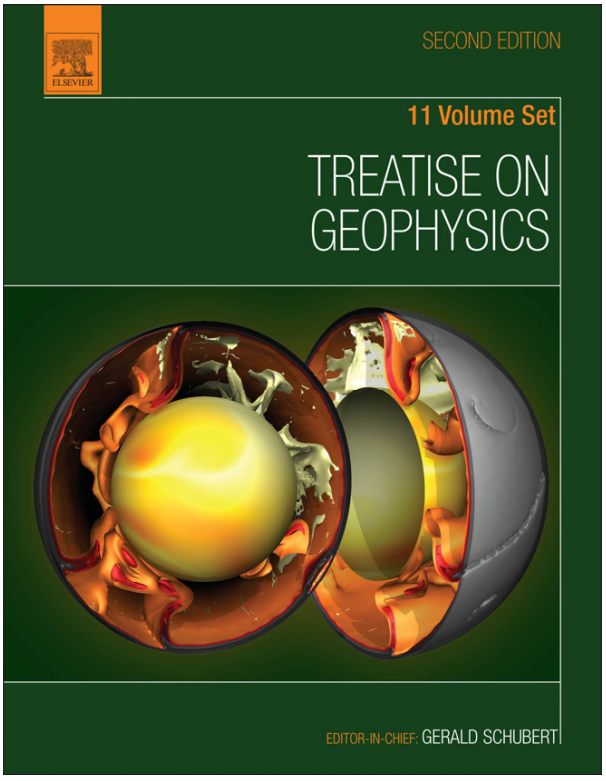

Schmitt D.R Geophysical Properties of the Near Surface Earth: Seismic Properties. In: Gerald Schubert (editor-in-chief) Treatise on Geophysics, 2nd edition, Vol 11. Oxford: Elsevier; 2015. p. 43-87.

11.03 Geophysical Properties of the Near Surface Earth: Seismic Properties

DR Schmitt, University of Alberta, Edmonton, AB, Canada

Glossary

Adiabat An adiabatic path in P–V–T space.

Adiabatic A thermodynamic process in which no heat is allowed to transfer into or out of the system. The local compression and rarefaction and corresponding increase and decrease of both pressure and temperature of a material as compressional wave passes are assumed to be an adiabatic process.

Anisotropy The condition in which the physical properties of a material will depend on direction.

Aspect ratio χ (dimensionless) In the context of crack-like porosity, this refers to the aperture width of the crack to its length.

Bulk modulus K (Pa) Also called the incompressibility. A measure of the resistance of a material to deformation for a given change in pressure.

Compliances S_{ij} (Pa^{-1}) The elastic mechanical parameters that generally relate stresses to strains.

Compressibility (Pa^{-1}) Inverse of the bulk modulus.

*Treatise on Geophysics, 2nd edition, (*2015), vol. 11, pp. 43-87

Cricondenbar For fluid mixtures. The greatest pressure at which both liquid and vapor phases can coexist. Above the cricondenbar, the mixture must be either a liquid or a supercritical fluid phase.
Critical point For pure fluids, a point in P–V–T space at which the liquid–vapor phase line terminates. The fluid will be in the supercritical state for pressures and temperatures above the critical pressure P_c and temperature T_c. At the critical point the fluid will have the critical specific volume V_c or equivalently the critical density $\rho_c = M/V_c$, where M is the chemical molecular weight.
Cricondentherm For fluid mixtures. The greatest temperature at which both liquid phase and vapor phase can still coexist. Above this temperature, the fluid will be either vapor or supercritical fluid phase.
Density ρ (kg m^{-3}) Mass per unit volume.
Equation of state A theoretical or empirical function or set of functions that describes the material's specific volume as a function of pressure and temperature.
Hooke's law The mathematical relationship between stress and strain via the elastic stiffnesses or conversely the strains and the stresses via the elastic compliances.
Isentropic A thermodynamic process in which the entropy of the system remains constant. A reversible adiabatic process is also isentropic.
Isochor A thermodynamic path in P–V–T space in which the specific volume V_m or the density ρ remains constant.
Isotherm A thermodynamic path in P–V–T space in which the temperature T remains constant. These are often the conditions employed in conventional measurements of fluid properties particularly in the petroleum industry.
Lamé parameters λ and μ (Pa). The two elastic parameters relating stresses to strains in the Lamé mathematical formulation of Hooke's law.
Poisson's ratio ν (dimensionless) The negative of the ratio between the radial and the axial strains induced by an axial stress.
Polycrystal A material that is a mixture of mineral crystals and that, often, is assumed to be free of pores. The properties of the polycrystal are then taken to be representative of those for the solid portion of the rock.
Pseudocritical point For fluid mixtures, a point in P–V–T space where the bubble and dew lines meet. This point depends on the composition of the mixture and occurs at the pseudocritical pressure P_{PC} and temperature T_{PC}.
Saturated The condition where the pore space of the rock is filled with fluids.
Saturation The fraction of the pore space that is filled with a given fluid. If only one fluid fills the pore volume, it will have a saturation of 1. If the pore volume is equally filled with two different fluids, they each will have a saturation of 0.5.
Shear modulus μ (Pa) The elastic mechanical parameter relating shear stress to shear strain.
Stiffness C_{ij} (Pa) The elastic mechanical parameters that generally relate strains to stresses.
Strain ϵ_{ij} or γ_{ij} (dimensionless) Measures of the deformation of a material.
Stress σ_{ij} or τ_{ij} (Pa) The ratio of an applied force to the area over which it is applied. Normal stresses σ_{ij} are directed perpendicularly to the surface. Shear stresses τ_{ij} are directed along the plane of the surface.
Supercritical The condition for a fluid encountered in P–V–T space in which it is no longer considered a liquid or a vapor (gas) but a fluid with the characteristics of both. For single-component fluids, the supercritical phase exists above the critical point at the critical pressure P_c and temperature T_c.
Young's modulus E (Pa) Also often referred to as the modulus of elasticity. The elastic mechanical parameter relating the linear axial strain induced to the applied axial normal stress.

11.03.1 Introduction

Geophysicists measure the spatial and temporal variations in electromagnetic, magnetic, and gravitational potentials and seismic wave fields in order to make inferences regarding the internal structure of the Earth in terms of, respectively, its electrical resistivity (See Chapters 2.25, 11.04, 11.08, and 11.10), its magnetism (See Chapters 2.24, 5.08, 11.05, 11.11), its density (See Chapter 3.03, 11.05, 11.12), and its elasticity (See Chapters 1.26 and 2.12). In seismology the most basic observation is that of a seismic wave's travel time from its source to the point of measurement. Seismologists continue to develop increasingly sophisticated analyses to convert this basic observation into seismic velocities from which the Earth's structure may be deduced. This holds true for the simplest 1-D seismic refraction analysis to the most complicated modern 3-D whole Earth tomogram. The influence of this velocity is not so directly apparent in seismic reflection profiles, but proper imaging depends critically on solid knowledge of the *in situ* seismic velocity structure. Indeed, as computational power grows, the differences between inversion and advanced prestack migration in imaging will become less distinct.

Velocity, as it is used in the geophysical community for wave speed, would certainly first come to a geophysicist's mind as a seismic property. It is also the seismic property that is most often used to infer lithology. Liberally, compressional wave velocities that can exist in crustal materials can range from a few hundred meters per second in air-saturated unconsolidated sediments to upward of 8 km s^{-1} for high-grade metamorphosed rocks at the top of the mantle. Typically then, within a given geologic context, the velocities themselves or additional parameters derived from them such as the compressional/shear wave speed ratio V_P/V_S, Poisson's ratio ν, or the seismic parameter $\varphi = V_P^2 - 4V_S^2/3$ are useful indicators of lithology. Unfortunately, the seismic velocities of any given lithology are not unique. Seismic velocities are affected by numerous factors such as mineralogical composition, texture, porosity, fluids, confining stress, pressure, and temperature, all of which contribute by differing degrees to the value of the

observed wave speed. Seismic anisotropy, being the variation of the wave speeds with direction of propagation through the medium, may also need to be included (Chapter 2.20). With attenuation, even the frequency at which the observation is made should be considered.

With a particular focus on the porous and fluid-filled Earth materials near the Earth's surface, the purpose of this contribution is to review 'seismic properties.' To most workers, this will again mean the measurable 'seismic velocity.' Such velocities are what we, as remote observers, can measure. More fundamentally, however, the seismic velocities are a manifestation of the competition between a material's internal forces (represented in a continuum via the elastic moduli) and inertia (through density). Without derivation, the relationships between the compressional P and S waves and the material's moduli and bulk density ρ are

$$V_P = \sqrt{\frac{K + 4\mu/3}{\rho}} \quad [1]$$

$$V_S = \sqrt{\frac{\mu}{\rho}} \quad [2]$$

where K and μ are the bulk and shear moduli for an isotropic medium, respectively. As fluids cannot support a shear stress, their $\mu = 0$ and eqn [1] reduces to the simpler longitudinal elastic wave of speed V_L

$$V_L = \sqrt{\frac{K}{\rho}} \quad [3]$$

first derived by Newton and thermodynamically corrected by Laplace. Care must be exercised in the choice of K particularly for fluids; much of the task of this contribution will not be in the examination of the wave speeds so much as attempting to understand the material's elastic moduli.

Later, when discussing a fluid-filled porous rock, the K and μ to be used in eqns [1] and [2] will necessarily be those of the bulk mixture of solids and fluids and will appropriately be denoted K_{sat} and μ_{sat}, respectively.

A given wave speed depends on the ratio between the moduli and density. One cannot understand the meaning of an observed seismic velocity, nor calculate it, without sufficient knowledge of these underlying moduli and density. Not surprisingly, then, the complexity of the physics needed to describe a wave velocity increases with the number of the material's characteristics considered. In particular, the introduction to the problem of porosity and mobile fluids multiplies the number of free parameters that can influence the material's moduli and density. Properly describing a near-surface material is substantially more difficult than trying to predict variations in, for example, the Earth's mantle where excursions of only a few percent are considered large!

This review is also carried out from the perspective of rock physics, the factors affecting wave speeds and the models used to predict them are presented. This is all done from the viewpoint of an experimentalist concerned with attempting to test such theories. That said, it must be recognized that often, one cannot have all of the information necessary, nor are the models sufficiently sophisticated, to properly predict a given velocity. This will more often than not be the case in seismic investigations of the near surface for resource exploration or engineering and environmental characterization. As such, at the end, a number of empirical relationships are also described. The basics of elasticity, anisotropy, and poroelasticity are briefly covered in order to set the stage for understanding how wave speeds relate to moduli. In attempting to understand the seismic properties of a fluid-saturated crustal rock, one must first have some understanding of the physical properties of the rock's constituent solid minerals, its saturating fluids, and finally its 'frame.' Minerals and fluids are the basic components in rocks in the upper crust and their behavior first must be studied. This is followed by a review of the factors affecting the rock's frame properties. Finally, these different components affecting rock properties are then integrated using various theories to arrive at estimates of the seismic properties. However, one may not always have available sufficient information to allow for the calculation of the physical properties, and for this case, a number of empirical relations and references to published compilations of observed results are provided. Lack of space restricts delving in detail into the range of issues related to seismic properties, so I conclude with some thoughts about the topics that will be important in the coming decade. A short glossary of terms that are not normally encountered in the geophysical literature is also provided.

11.03.2 Basic Theory

Any understanding of the propagation of mechanical waves rests on basic elasticity theory. The number of texts on this topic is large and little is to be gained here by repeating the basic concepts of stress and strain, the development of Hooke's law, or the construction of the wave equations linking elasticity to wave velocities. I assume the reader will have some basic understanding of elasticity. Some recommended texts covering the basic governing equations at different levels of sophistication include Bower (2010), Fung (1965), and Tadmor et al. (2012). Stein and Wysession (2002) gave a particularly cogent exposition of both isotropic elasticity and the solution to the wave equation particularly as it relates to seismology. Auld (1990) provided an excellent advanced overview of elasticity with good emphasis on elastic anisotropy; the notation styles employed here follow largely from this text. For understanding of more complicated materials, the essentials of poroelasticity can be found in Wang (2000), Bourbié et al. (1987), and Gueguen and Bouteca (2004); of anelasticity in Lakes (2009) and Carcione (2007); and of hyperelasticity (nonlinear elasticity) in Holzapfel (2000). These texts will well cover the details, and only the necessary definitions of moduli within the Voigt representation of Hooke's law are provided.

11.03.2.1 Hooke's Constitutive Relationship and Moduli

In this contribution, we assume all strains are infinitesimal and describe to the first order the material's deformation via the strain tensor ε

$$\epsilon(x,y,z)=\begin{bmatrix}\epsilon_{xx} & \epsilon_{xy} & \epsilon_{xz}\\ \epsilon_{yx} & \epsilon_{yy} & \epsilon_{yz}\\ \epsilon_{zx} & \epsilon_{zy} & \epsilon_{zz}\end{bmatrix}$$

$$=\begin{bmatrix}\dfrac{\partial u_x}{\partial x} & \dfrac{1}{2}\left(\dfrac{\partial u_x}{\partial y}+\dfrac{\partial u_y}{\partial x}\right) & \dfrac{1}{2}\left(\dfrac{\partial u_x}{\partial z}+\dfrac{\partial u_z}{\partial x}\right)\\ \dfrac{1}{2}\left(\dfrac{\partial u_y}{\partial x}+\dfrac{\partial u_x}{\partial y}\right) & \dfrac{\partial u_y}{\partial y} & \dfrac{1}{2}\left(\dfrac{\partial u_y}{\partial z}+\dfrac{\partial u_z}{\partial y}\right)\\ \dfrac{1}{2}\left(\dfrac{\partial u_z}{\partial x}+\dfrac{\partial u_x}{\partial z}\right) & \dfrac{1}{2}\left(\dfrac{\partial u_z}{\partial y}+\dfrac{\partial u_y}{\partial z}\right) & \dfrac{\partial u_z}{\partial z}\end{bmatrix} \quad [4]$$

where the displacement of the particle originally at (x, y, z) is given by the vector $\mathbf{u}=u_x\mathbf{i}+u_y\mathbf{j}+u_z\mathbf{k}$. Forces within the materials are defined by the stress tensor σ:

$$\sigma(x,y,z)=\begin{bmatrix}\sigma_{xx} & \tau_{xy} & \tau_{xz}\\ \tau_{yx} & \sigma_{yy} & \tau_{yz}\\ \tau_{zx} & \tau_{zy} & \sigma_{zz}\end{bmatrix} \quad [5]$$

where normal and shear stresses are represented by σ_{ii} and τ_{ij}, respectively. Hooke's law is the linear constitutive relationship between strain equation [4] and stress equation [5]. The simplest case of an isotopic medium is most commonly assumed in studies of wave propagation. In this case, Hooke's law may be written in the abbreviated Voigt notation as using the mathematical simplifications afforded by the use of the Lamé parameters λ and μ:

$$\begin{bmatrix}\sigma_{xx}\\ \sigma_{yy}\\ \sigma_{zz}\\ \tau_{yz}\\ \tau_{zx}\\ \tau_{xy}\end{bmatrix}=\begin{bmatrix}\lambda+2\mu & \lambda & \lambda & 0 & 0 & 0\\ \lambda & \lambda+2\mu & \lambda & 0 & 0 & 0\\ \lambda & \lambda & \lambda+2\mu & 0 & 0 & 0\\ 0 & 0 & 0 & \mu & 0 & 0\\ 0 & 0 & 0 & 0 & \mu & 0\\ 0 & 0 & 0 & 0 & 0 & \mu\end{bmatrix}\begin{bmatrix}\epsilon_{xx}\\ \epsilon_{yy}\\ \epsilon_{zz}\\ 2\epsilon_{yz}\\ 2\epsilon_{zx}\\ 2\epsilon_{xy}\end{bmatrix} \quad [6]$$

The reader should take note of the pattern relating the tensors of eqns [4] and [5] to the stress and strain vectors of the Voigt abbreviated notation of eqn [6] in which the shear strains are multiplied by the awkward factor of 2. The Lamé formulation is mathematically elegant and simple. This simplicity comes with some cost, however, in that λ cannot be directly measured in a simple experiment. In contrast, the second Lamé parameter μ is the shear modulus, which is the simple ratio between an applied shear stress τ and the resulting shear strain $\gamma_{ij}=2\epsilon_{ij}$, a value that can readily be experimentally measured (**Figure 1(c)**).

Two other important moduli in isotropic media are Young's modulus E and the already introduced bulk modulus K. These can be found by conducting simple experiments with clear physical interpretations. E is the ratio between an applied uniaxial stress and its corresponding resulting coaxial linear strain (**Figure 1(b)**). K is the ratio between an applied uniform (hydrostatic) pressure P and the consequent volumetric strain $\theta=\epsilon_{xx}+\epsilon_{yy}+\epsilon_{zz}$. Poisson's ratio ν is not a modulus but it too is an important and popular measure of a material's deformation under stress. It is simply the negative of the ratio between the lateral ϵ_{xx} and axial ϵ_{yy} strains observed during the same test used to measure E (**Figure 1(b)**).

E, K, λ, μ, or ν can be calculated if any of the other two moduli or parameters are known; extensive conversion tables are readily found (e.g., Birch, 1961; Mavko et al., 2003). Some of these relations are, for convenience,

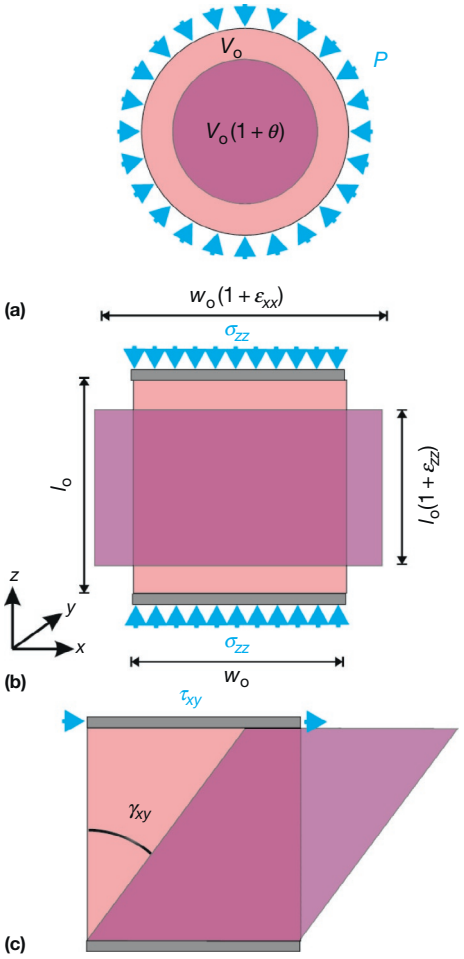

Figure 1 Illustration of the three basic deformations that allow the isotropic elastic moduli to be described. The original dimensions of the object are in light red with the deformed version in transparent purple. (a) Change in volume θV_o upon application of uniform pressure P defining the bulk modulus $K=-P/\theta$, there is no change in shape. (b) Change in the length $l_o\epsilon_{yy}$ and width $w_o\epsilon_{xx}$ upon application of a uniaxial stress σ_{yy} defining the Young's modulus $E=\sigma_{yy}/\epsilon_{yy}$ and Poisson's ratio $\nu=-\epsilon_{xx}/\epsilon_{yy}$. Both the shape and volume change and (c) the change in shape described by the angle $\gamma=2\epsilon_{xy}$ upon application of a simple shear stress τ_{xy} defining the shear modulus $\mu=\tau_{xy}/\epsilon_{xy}$. There is no change in volume.

$$\begin{aligned}E&=\frac{9K\mu}{3K+\mu}\\ K&=\lambda+2\mu/3\\ \mu&=\frac{3}{2}(K-\lambda)\\ \nu&=\frac{3K-E}{6K}\end{aligned} \quad [7]$$

In the case of a liquid, $\mu=0$ and λ can be assigned a physical interpretation as it collapses to the bulk modulus K.

Although we will not be directly addressing issues of seismic reflectivity here, one can also consider the acoustic impedances $Z_i=\rho_i V_i$, where i indicates either the P or the S wave, as a physical property in their own right.

Most of the theoretical models that will follow attempt to develop expressions for K and μ. With this in mind, Hooke's

law (eqn [6]) may alternatively be expressed less elegantly but more physically as

$$\begin{bmatrix}\sigma_{xx}\\ \sigma_{yy}\\ \sigma_{zz}\\ \tau_{yz}\\ \tau_{zx}\\ \tau_{xy}\end{bmatrix}=\begin{bmatrix}K+\frac{4}{3}\mu & K-\frac{2}{3}\mu & K-\frac{2}{3}\mu & 0 & 0 & 0\\ K-\frac{2}{3}\mu & K+\frac{4}{3}\mu & K-\frac{2}{3}\mu & 0 & 0 & 0\\ K-\frac{2}{3}\mu & K-\frac{2}{3}\mu & K+\frac{4}{3}\mu & 0 & 0 & 0\\ 0 & 0 & 0 & \mu & 0 & 0\\ 0 & 0 & 0 & 0 & \mu & 0\\ 0 & 0 & 0 & 0 & 0 & \mu\end{bmatrix}\begin{bmatrix}\epsilon_{xx}\\ \epsilon_{yy}\\ \epsilon_{zz}\\ 2\epsilon_{yz}\\ 2\epsilon_{zx}\\ 2\epsilon_{xy}\end{bmatrix} \quad [8]$$

A comparison of eqns [1] and [7] also allows the moduli to be written in terms of the wave speeds as

$$\begin{aligned}\mu&=\rho V_S^2,\\ K&=\rho\left(V_P^2-\frac{4}{3}V_S^2\right),\\ \nu&=\frac{1}{2}\left(\frac{V_P^2-2V_S^2}{V_P^2-V_S^2}\right)\end{aligned} \quad [9]$$

11.03.3 Mineral Building Blocks

11.03.3.1 Elastic Properties of Minerals

The majority of seismological studies assume that the elastic responses of Earth materials behave according to eqn [6]. In reality, however, isotropy is the exception; all minerals and most rocks are elastically anisotropic. We introduce this topic early as it is key to understanding how we arrive at the physical properties of the minerals that constitute the rocks. To include this anisotropy, eqn [8] may more generally be rewritten as

$$\begin{bmatrix}\sigma_{xx}\\ \sigma_{yy}\\ \sigma_{zz}\\ \tau_{yz}\\ \tau_{zx}\\ \tau_{xy}\end{bmatrix}=\sigma=\begin{bmatrix}C_{11} & C_{12} & C_{13} & C_{14} & C_{15} & C_{16}\\ C_{21} & C_{22} & C_{23} & C_{24} & C_{25} & C_{26}\\ C_{31} & C_{32} & C_{33} & C_{34} & C_{35} & C_{36}\\ C_{41} & C_{42} & C_{43} & C_{44} & C_{45} & C_{46}\\ C_{51} & C_{52} & C_{53} & C_{54} & C_{55} & C_{56}\\ C_{61} & C_{62} & C_{63} & C_{64} & C_{65} & C_{66}\end{bmatrix}=\begin{bmatrix}\epsilon_{xx}\\ \epsilon_{yy}\\ \epsilon_{zz}\\ 2\epsilon_{yz}\\ 2\epsilon_{zx}\\ 2\epsilon_{xy}\end{bmatrix}=[c]\epsilon \quad [10]$$

where each of the matrix components C_{ij} is called the elastic stiffnesses. More formally, eqn [10] condenses the expression of Hooke's law through the fourth-order tensor components $\sigma_{ij}=c_{ijkl}\epsilon_{kl}$ with the condensed subscripts following the rules:

$$\mathbf{xx}\rightarrow\mathbf{1},\ \mathbf{yy}\rightarrow\mathbf{2},\ \mathbf{zz}\rightarrow\mathbf{3},\ \mathbf{yz}\rightarrow\mathbf{4},\ \mathbf{xz}\rightarrow\mathbf{5},\ \text{and}\ \mathbf{xy}\rightarrow\mathbf{6} \quad [11]$$

and with the full stiffness matrix represented by $[c]$. ϵ and σ represent the corresponding stress and strain vectors, respectively, within this abbreviated notation. Further, $C_{ij}=C_{ji}$ making $[c]$ symmetrical such that there are at most 21 independent elastic stiffnesses. The total number depends on the degree of symmetry of the system varying from only 2 for the isotropic case just shown to the full 21 for the least symmetrical triclinic crystals as will be discussed shortly. Conversely, the strains can be written in terms of the applied stresses using the elastic compliances S_{ij} with their matrix similarly represented by $[s]$

$$\begin{bmatrix}\epsilon_{xx}\\ \epsilon_{yy}\\ \epsilon_{zz}\\ 2\epsilon_{yz}\\ 2\epsilon_{zx}\\ 2\epsilon_{xy}\end{bmatrix}=\epsilon=\begin{bmatrix}S_{11} & S_{12} & S_{13} & S_{14} & S_{15} & S_{16}\\ S_{21} & S_{22} & S_{23} & S_{24} & S_{25} & S_{26}\\ S_{31} & S_{32} & S_{33} & S_{34} & S_{35} & S_{36}\\ S_{41} & S_{42} & S_{43} & S_{44} & S_{45} & S_{46}\\ S_{51} & S_{52} & S_{53} & S_{54} & S_{55} & S_{56}\\ S_{61} & S_{62} & S_{63} & S_{64} & S_{65} & S_{66}\end{bmatrix}\begin{bmatrix}\sigma_{xx}\\ \sigma_{yy}\\ \sigma_{zz}\\ \tau_{yz}\\ \tau_{zx}\\ \tau_{xy}\end{bmatrix}=[s]\sigma \quad [12]$$

The author takes no responsibility for the fact that conventionally $[s]$ and $[c]$ are used to, respectively, denote the compliances and the stiffnesses. Regardless, the Voigt form is particularly useful because

$$[c]=[s]^{-1} \quad [13]$$

where the superscript '-1' indicates the matrix inverse operation (Auld, 1990). We note that an important property of the tensor (in its abbreviated form here) is its transformation upon change of the basis coordinate system. The mathematics describing this is beyond the needs of this contribution but Walker and Wookey (2012) provided convenient MATLAB® codes to carry out these otherwise tedious calculations.

Using this form, eqn [8] for the isotropic case is

$$\begin{bmatrix}\sigma_{xx}\\ \sigma_{yy}\\ \sigma_{zz}\\ \tau_{yz}\\ \tau_{zx}\\ \tau_{xy}\end{bmatrix}=\begin{bmatrix}C_{11} & C_{12} & C_{12} & 0 & 0 & 0\\ C_{12} & C_{11} & C_{12} & 0 & 0 & 0\\ C_{12} & C_{12} & C_{11} & 0 & 0 & 0\\ 0 & 0 & 0 & C_{44} & 0 & 0\\ 0 & 0 & 0 & 0 & C_{44} & 0\\ 0 & 0 & 0 & 0 & 0 & C_{44}\end{bmatrix}\begin{bmatrix}\epsilon_{xx}\\ \epsilon_{yy}\\ \epsilon_{zz}\\ 2\epsilon_{yz}\\ 2\epsilon_{zx}\\ 2\epsilon_{xy}\end{bmatrix} \quad [14]$$

with only C_{11} and C_{12} necessary and $C_{44}=(C_{11}-C_{12})/2$. The symmetry of $[c]$ across the main diagonal should be kept in mind.

Some of the hypothetical experiments that could be carried out in order to find some of the rarer off-axis elastic stiffnesses that couple normal stresses to shear strains and vice versa are illustrated in **Figure 2**. Hearmon (1946) gave the geometry for a number of such static measurements that could be used to fill $[c]$.

For anisotropic materials, the configuration of $[c]$ depends on the material's degree of symmetry. Such symmetry is classified within the six crystal systems listed in terms of diminishing symmetry: cubic (or isometric), hexagonal, tetragonal, orthorhombic, monoclinic, and triclinic. The literature is not necessarily consistent on how many crystal systems there are, and many authors divide the hexagonal system into separate hexagonal and trigonal systems for a total of 7. This classification is used here following Auld (1990) and Tinder (2007). Regardless of the preference, nine different sets of stiffnesses $[c]$ can be defined. This is larger than the seven classes because two unique sets exist in both the trigonal and the tetragonal systems depending on the slightly different symmetries. The lower the symmetry, the greater the number of independent elastic stiffnesses required. The organization of the nine different sets of $[c]$ is shown symbolically in **Figure 3**.

Bass (1995) had compiled an extensive collection of C_{ij} for many minerals up to 1995, and Angel et al. (2009) provided an overview of the techniques used to obtain these elastic constants. The full sets of the values in $[c]$ are repeated here for a

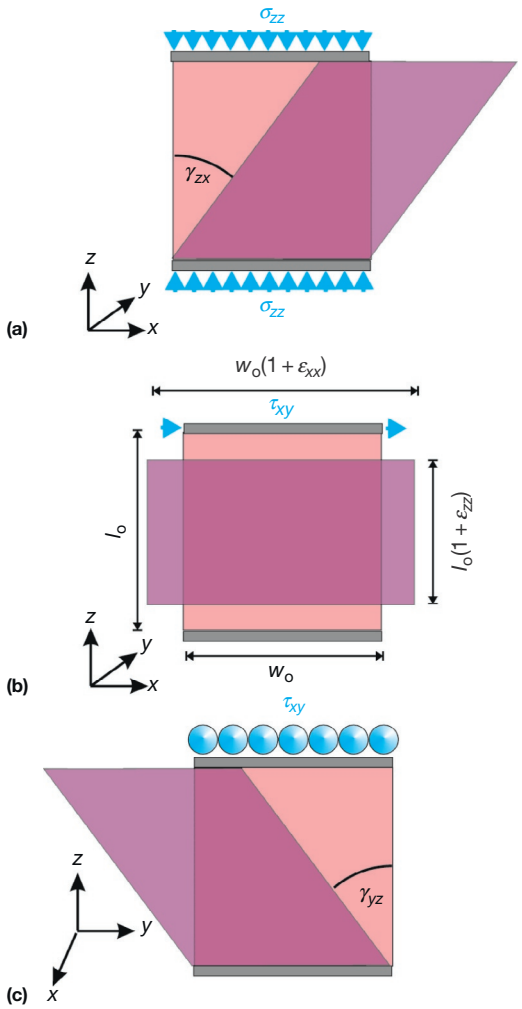

Figure 2 Illustration of the physical meaning of the elastic moduli that provide stress–strain responses outside of those defined in **Figure 1**. (a) Generation of a shear deformation of angle γ_{zx} by the application of a uniaxial stress σ_{zz} leading to the definition of $C_{53}=\sigma_{zz}/\gamma_{zx}$. (b) Generation of normal strains ϵ_{xx} and ϵ_{zz} by the application of a shear stress (shown as a pure shear) τ_{xy} leading to the definitions of $C_{16}=\tau_{xy}/\epsilon_{xx}$ and $C_{36}=\tau_{xy}/\epsilon_{zz}$, respectively. (c) Generation of a shear strain γ_{yz} by application of the shear stress τ_{xy} leading to the definitions of $C_{16}=\tau_{xy}/\gamma_{yz}$.

few of the more important minerals in **Table 1**. While most of the values are from Bass (1995), it should be no surprise that his compilation did not include any values for triclinic minerals, as determining all 21 independent elastic constants for a triclinic mineral awaited the more recent work of Brown et al. (2006).

11.03.3.2 Bounds on Isotropic Mixtures of Anisotropic Minerals

The discussion in the preceding text revealed that all minerals are elastically anisotropic to some degree. However, we often prefer that the rocks that we study, which are of course an assemblage of these minerals, be isotropic. That is, most workers prefer to indirectly employ the values in [c] distilled into bulk K and shear μ moduli for an isotropic polycrystal; it is this isotropic value that is often all that is reported in compilations. This value is usually called the Voigt–Reuss–Hill (VRH) average (Hill, 1952), being the simple arithmetic mean of the isostress Voigt (Voigt, 1928) and isostrain Reuss (1929b) bounds. The Voigt bulk K_V and shear μ_V moduli for any crystal class (Anderson, 1963; Hill, 1952) are

$$K_V=\frac{1}{9}[(c_{11}+c_{22}+c_{33})+2(c_{12}+c_{23}+c_{13})]$$
$$\mu_V=\frac{1}{15}[(c_{11}+c_{22}+c_{33})-(c_{12}+c_{23}+c_{13})+3(c_{44}+c_{55}+c_{66})] \quad [15]$$

while the corresponding Reuss bulk K_R and shear μ_R moduli are

$$K_R=\frac{1}{[(s_{11}+s_{22}+s_{33})+2(s_{12}+s_{13}+s_{23})]}$$
$$\mu_R=\frac{15}{[4(s_{11}+s_{22}+s_{33})-4(s_{12}+s_{13}+s_{23})+3(s_{44}+s_{55}+s_{66})]} \quad [16]$$

One problem can be that the mineral moduli are reported as stiffnesses in [c] but eqn [16] uses the compliances of [s]. To overcome this issue, Watt and coworkers (Watt, 1979, 1980, 1986; Watt and Peselnick, 1980) laboriously derived the expressions for K_R and μ_R in terms of the stiffnesses C_{ij}. Today, however, matrix inversions are easily accomplished and one may prefer to first calculate the compliances s_{ij} using eqn [13] and substitute them directly into eqn [16].

Berryman (2005) also provided alternative formulas developed using a self-consistent approach.

These Voigt and Reuss moduli usually provide the upper and lower bounds to the moduli, respectively, as shown by Hill (1952). The values for isotropic polycrystals that are most often reported in compilations (**Table 1**), however, are the simple VRH arithmetic mean averages of these two bounds for the bulk

$$K_{VRH}=[K_R+K_V]/2 \quad [17]$$

and the shear moduli

$$\mu_{VRH}=[\mu_R+\mu_V]/2 \quad [18]$$

The differences in the bounds are insignificant for the highly symmetrical isotropic and cubic cases. Indeed, **Table 1** purposefully displays more significant digits than legitimate just to show the minor differences between the values for pyrope garnet. However, for hexagonal ice (Ih), the differences between the bounding shear moduli differ by 40%.

More rigorous bounds may also be found. *Simmons* (Meister and Peselnick, 1966; Peselnick and Meister, 1965; Simmons and Wang, 1971; Watt, 1979, 1980, 1986) derived stronger bounds on the isotropic polycrystalline moduli using the variational principles of Hashin and Shtrikman (1962) for all of the crystal classes except for triclinic. Of course, these become increasingly complicated as symmetry decreases and more elastic constants are required; and we repeat here only Simmon's (see Simmons and Wang, 1971) expression for cubic minerals:

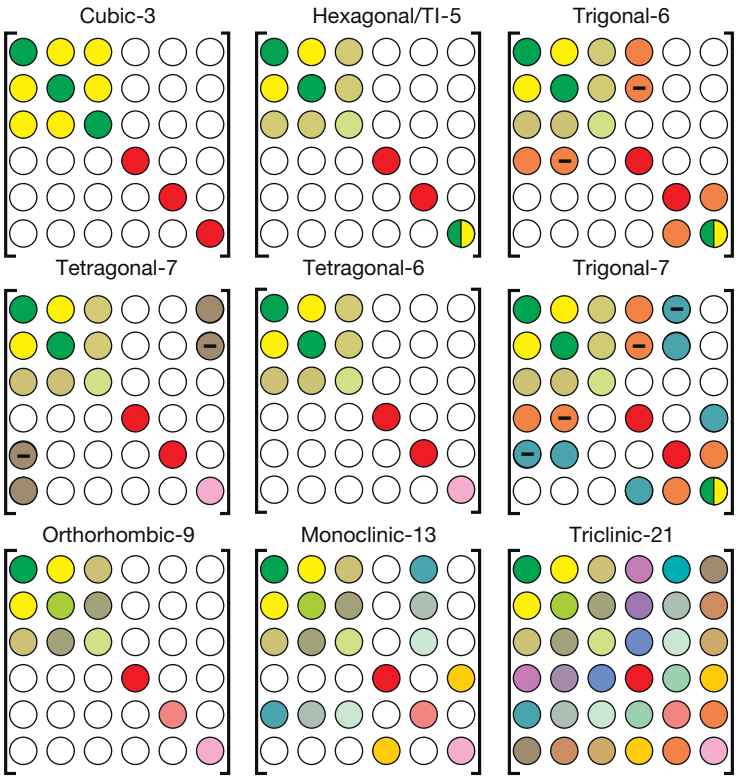

Figure 3 Graphic description of the nine different elastic stiffness matrices [c] in Voigt abbreviated notation following eqn [10] and employing Tinder's (2007) form. The symmetrical system and its corresponding number of independent C_{IJ}'s are given by the title immediately above each matrix. The values of the C_{ij} are color-coded. A white circle indicates zero. The same solid color for different components means that they share the same numerical value. A minus sign indicates that the component's value is the negative of the adjacent component of the same solid color. Note that C_{66} in the hexagonal and trigonal [c] matrices has two colors; this is to indicate that in these systems, $C_{66}=(C_{11}-C_{12})/2$.

$$
\begin{aligned}
&K_{HS^+}=K_{HS^-}=K_V=K_R=K\\
&\mu_{HS^+}=G_1+3\left[\frac{5}{G_2-G_1}+4\frac{3K+2G_1}{5G_1(3K+4G_1)}\right]^{-1}\\
&\quad\geq\mu\geq G_2+2\left[\frac{5}{G_1-G_2}+6\frac{3K+2G_2}{5G_2(3K+4G_2)}\right]^{-1}=\mu_{HS^-}\\
&\quad G_1=\frac{1}{2}(c_{11}-c_{12})\\
&\quad G_2=c_{44}
\end{aligned}
\qquad [19]
$$

Calculations of these different averages generally, but not always, show that the VRH averages lie within the HS bounds. This suggests that the VRH averages provide reasonable estimates of the isotropic polycrystal properties. The validity of the VRH averages in providing representative values still remains of current interest (Berryman, 2005, 2012; Pham, 2011).

Table 1 lists K_{VRH} and μ_{VRH} for many of the minerals commonly found within crustal rocks; these values are often used for calculating rock properties. This list is not intended to be comprehensive and many more complete compilations are available (Babuška and Cara, 1991; Bass, 1995; Gebrande, 1982; Hearmon, 1946, 1956; Huntington, 1958; Simmons and Wang, 1971; Sumino and Anderson, 1984). Many of the moduli in these compilations are reproduced from the extensive acoustic measurements made by Alexandrov and coworkers in the 1960s (Alexandrov and Ryzhova, 1961a,b, 1962, 1964; Ryzhova et al., 1966) on large (and imperfect) single crystals (see Brown et al., 2006). The impressive contributions of Alexandrov and coworkers have been invaluable to the geophysical community, but an update of their measurements on the minerals forming rocks in the upper crust using more modern techniques is long overdue.

11.03.3.3 Isothermal Versus Adiabatic Moduli

So far, the bulk modulus has been defined as the simple quotient of an applied hydrostatic stress to the resulting volumetric strain P/θ as shown in Figure 1. This is true, but one must also be careful about the conditions under which the experiment is carried out. A bulk modulus measurement can be carried out either of two ways depending on how heat energy is allowed to move during the experiment:

i. Adiabatically (also isentropically) when the material is compressed and no heat is allowed to flow in or out of the system
ii. Isothermally where heat can flow in or out in order to maintain the temperature of the system constant

Table 1 Values of the elastic stiffnesses for select materials displaying varying degrees of symmetry

'ij'	Isotropic Fused SIO2	Cubic Pyrope	hexagonal ice (Ih) (257 K)	Trigonal - 6 α-quartz	Trigonal - 7 Dolomite	Tetragonal - 6 Rutile	Tetragonal - 7 Wulfenite	Orhtorhombic Enstatite	Monoclinic Muscovite	Triclinic Low Albite
	Stiffnesses in GPa									
11	78.08	296.2	13.5	86.6	205	269	109	225	183	69.9
22	78.08	296.2	13.5	86.6	205	269	109	178	178	183.5
33	78.08	296.2	14.9	106.1	113	480	92	214	59.1	179.5
44	31.38	91.6	3.09	57.8	39.8	124	26.7	77.6	16	24.9
55	31.38	91.6	3.09	57.8	39.8	124	26.7	75.9	17.6	26.8
66	31.38	91.6	3.5	40	67	192	33.7	81.6	72.4	33.5
12	15.32	111.1	6.5	6.7	71	177	68	72.4	48.3	34
13	15.32	111.1	5.9	12.6	57.4	146	53	54.1	23.8	30.8
23	15.32	111.1	5.9	12.6	57.4	146	53	52.7	21.7	5.5
14	0	0	0	–17.8	–19.5	0	0	0	0	5.1
15	0	0	0	0	13.7	0	0	0	–2	–2.4
16	0	0	0	0	0	0	–13.6	0	0	–0.9
24	0	0	0	17.8	19.5	0	0	0	0	–3.9
25	0	0	0	0	–13.7	0	0	0	3.9	–7.7
26	0	0	0	0	0	0	13.6	0	0	–5.8
34	0	0	0	0	0	0	0	0	0	–8.7
35	0	0	0	0	0	0	0	0	1.2	7.1
36	0	0	0	0	13.7	0	0	0	0	–9.8
45	0	0	0	0	0	0	0	0	0	–2.4
46	0	0	0	0	0	0	0	0	0.5	–7.2
56	0	0	0	–17.8	–19.5	0	0	0	0	0.5
K_V	**36.24**	**172.8**	**8.722**	**38.1**	**99.4**	**217**	**73.11**	**108**	**67.5**	**63.8**
K_R			**8.717**	**37.6**	**89.1**	**209**	**71.58**	**107**	**48.7**	**55.2**
K_H			**8.72**	**37.85**	**94.25**	**213**	**72.35**	**108**	**58.1**	**59.50**
μ_V	**31.38**	**91.98**	**3.5093**	**47.6**	**51.8**	**124.6**	**19.75**	**76.2**	**43**	**41.2**
μ_R		**91.98**	**5.689**	**41**	**40**	**98.7**	**25.33**	**75.2**	**27.6**	**29.8**
μ_H		**92.0**	**4.60**	**44.3**	**45.9**	**111.7**	**22.5**	**75.7**	**35.3**	**35.5**
M_V	**78.08**	**295.4**	**13.4**	**101.6**	**168.5**	**383.1**	**99.44**	**210**	**125**	**118.7**
M_R		**295.4**	**13.3**	**92.2**	**142.4**	**340**	**105.4**	**208**	**85.4**	**94.93**
M_H		**295.4**	**13.4**	**96.9**	**155.5**	**361.6**	**102.4**	**209**	**105**	**106.8**

Cell color fills correlate to the symbolic representation of the Voigt elastic stiffness matrices in **Figure 3**. Values are taken from Bass (1995) except for isotropic fused SiO_2 (Ohno et al., 2000) and triclinic low albite (Brown et al., 2006). Values in bold are calculated from the other elastic stiffnesses.

A propagating compressional wave consists of alternating zones of high pressure and low pressure that are slightly hotter and colder, respectively, than the initial ambient temperature. An isothermal state could only be achieved if during a half-period, the heat could fully conduct from the high- to the low-pressure regions. This is in fact difficult to achieve (Condon, 1933; Fletcher, 1974, 1976) with the somewhat paradoxical result that isothermal conditions can only be reached at extremely high frequencies where, in a gas, the wavelengths are comparable to the mean free path of the molecules (Condon, 1933).

Table 2 is typical of the types of data presented in the literature for such properties but its simplicity does hide a number of complications that the reader, usually simply looking for a value to use, should still keep in mind. The first is that the values reported are usually the VRH averages as just noted.

The values reported are also usually the adiabatic bulk moduli as would be measured using acoustic techniques.

In most of the solid crystalline materials, this will insignificantly differ from the isothermal bulk modulus K_T obtained from static measurements carried out at constant temperature. Voigt (1928) (p. 788; see also Hearmon (1946)) provided the relationship between the isothermal $\overset{T}{}_{ik}$ and the adiabatic s_{ij} compliances:

$$s_{ik}^{T} = s_{ik} + \frac{\alpha_i \alpha_k T}{\rho C_P} \quad [20]$$

where ρ is the density, T is the absolute temperature in $^\circ K$, C_P is the heat capacity at constant pressure, and α_i is the appropriate component of the thermal expansion tensor (see Landau and Lifshitz, 1970, Section 10). This difference can often be ignored for most minerals, although for KCl, the two S_{12} values differ by 18%. The reader may be able to obtain appropriate values for α_i and C_P and formulas for their correction to pressure and temperature in the compilations of Holland and Powell (1998). It is important to note, however, that these differences cannot generally so easily be ignored for fluids. This issue will be discussed in more detail later.

11.03.3.4 Effects of Pressure and Temperature on Mineral Moduli

The values in Table 2 are for the most part provided under standard or room conditions. In many cases, in the upper crust, the use of such values as 'constants' is generally valid as the variations with pressure and temperature will be small. For example, the variations in the properties are usually ignored in petroleum and near-surface seismology. Those studying shallow and high-temperature geothermal systems may, however, need to take such variations into account.

Even though we can often ignore their effects, the moduli for various minerals are not constants and do depend on both the temperature and the confining pressure. With increasing confining pressure, minerals become stiffer and more rigid, and the first-order derivatives of the bulk $\delta K/\delta P$ and $\delta \mu/\delta P$ are positive and the range for most minerals is between 4–6 Pa Pa^{-1} and 0.5–2 Pa Pa^{-1}, respectively. Conversely, the moduli decrease with temperature with $\delta K/\delta T \sim -5$ MPa $^\circ$K^{-1} to -30 MPa $^\circ$K^{-1}. As such, within the crust, temperature will usually influence the moduli more than pressure. The changes in the moduli and density of an isotropic polycrystalline quartz compact with pressure and temperature are shown for purposes of illustration in Figure 4. These suggest that the effects of pressure and temperature tend to cancel each other out, although in areas with steep thermal gradients, the changes in temperature can significantly alter the bulk modulus and the density of the quartz. The range of temperatures is intentionally shown to reflect the larger variations in the physical properties of the quartz in the vicinity of the α-quartz to β-quartz phase transition.

11.03.3.5 Mineral Densities

Equations [1] and [2] also include the material's bulk density ρ. Consider a rock composed of m separate mineral phases each with density ρ_i and ϕ_i of the fractional volume of the material (with $\Sigma\phi_i = 1$). The density for this rock takes the form

$$\rho = \sum_{i=1}^{m} \phi_i \rho_i \quad [21]$$

Our knowledge of mineral density is often taken for granted, but in reality, it may not always be so easy to determine and a number of different methods are applied. While usually the differences are small, one may still need to take care to know how the number is derived. The methods used to determine density include the following:

i. Archimedean fluid displacement in which the mineral sample's volume is found from the amount of reference fluid volume that it displaces. The density so determined is referred to as the specific gravity and it is simply equal to the ratio of the sample's measured mass to the volume of the fluid displaced.
ii. Boyle's law pyncnometry where the sample volume is determined by in a measurement of the deviation of the gas pressure in a container of a known volume (Lowell et al., 2004). The noble gas helium is usually used.
iii. x-Ray and neutron scattering crystallography that provide information on the dimensions and hence volume $V_{x\text{-ray}}$ of

Table 2 Density, isotropic bulk moduli, and isotropic polycrystalline wave speeds

Material	*Density (kg m^{-3})*	*Adiabatic bulk modulus* K *(GPa)*	*Shear modulus* μ *(GPa)*	*Poisson's ratio* ν	V_P *(m s^{-1})*	V_S *(m s^{-1})*
Tectosilicates						
α-Quartz	2648	37.8	44.3	0.079	6048	4090
β-Quartz[a]	2522	42.97	41.41	0.135	6239	4052
Albite	2610[b]	56.9	28.6	0.285	6034	3310
Anorthite	2765[b]	84.2	39.9	0.295	7049	3799
Orthoclase	2571[b]	62	29.3	0.296	6270	3376
Microcline	2567	55.4	28.1	0.283	6015	3309
Neosilicates						
Forsterite	3221	129.5	81.1	0.241	8589	5018
Fayalite	4380	134	50.7	0.332	6784	3402
$Fo_{91}Fa_9$	3325	129.5	77.6	0.250	8370	4831
Grossular	3602	168.4	108.9	0.234	9331	5498
Pyrope	3567	172.8	92	0.274	9101	5079
Inosilicates						

(*Continued*)

Table 2 (Continued)

Material	*Density (kg m^{-3})*	*Adiabatic bulk modulus* K *(GPa)*	*Shear modulus* μ *(GPa)*	*Poisson's ratio* ν	V_P *(m s^{-1})*	V_S *(m s^{-1})*
Hornblende	3150	93.3	49.3	0.275	7105	3956
Augite	3320	95	59	0.243	7233	4216
Ferrosilite	4002	101	52	0.280	6524	3605
Enstatite	3272	107.8	75.7	0.215	7987	4810
Phyllosilicates						
Muscovite (Illite?[c])	2844	58.2	35.3	0.248	6084	3523
Biotite	3050	50.5[d]	27.4[d]	0.270	5342	2997
Kaolinite	2669[b]	71.1[e]	31.2[e]	0.309	6498	3419
Na montmorillonite, dry	2700[f]	82[g]	32[g]	0.327	6795	3443
Na montmorillonite, wet	1700[f]	36[g]	16.5[g]	0.301	5841	3115
Talc[h]	2793	41.6	22.6	0.270	5068	2845
Lizardite[i]	2516	61	33.9	0.265	6400	3600
Antigorite[i]	2668	69	34.0	0.288	6520	3570
Evaporites						
Calcite	2712	73.3	32	0.309	6539	3435
Aragonite	2930	46.9	38.5	0.178	5790	3625
Dolomite	3795	94.9	45.7	0.293	6408	3470
Anhydrite	2963	54.9	29.3	0.273	5631	3145
Gypsum	2317	42	15.4	0.337	5195	2578
Halite	2163	24.9	14.7	0.253	4536	2607
Sylvite	1987	18.1	9.4	0.279	3926	2175
Barite	4473	55	22.8	0.318	4369	2258
Oxides						
Corundum	3982	253.5	163.2	0.235	10 877	6402
Magnetite	5206	161	91.4	0.261	7371	4190
Periclase	3584	160	130.3	0.180	9650	6030
Ice-I (270 K)	917.5	8.73	3.4	0.328	3802	1925
Sulfides						
Pyrite	5016	142.7	125.7	0.160	7865	5006
Galena	7597	58.6	31.9	0.270	3649	2049
Sphalerite	4088	77.1	31.5	0.320	5398	2776
Others						
Diamond	3512	443	535.7	0.069	18 153	12 350
Graphite	2260	161.0	109.3	0.223	11 650	6954
Fluids						
Air (STP) dry[k]	1.31	0.00014311	–	–	330.2	–
Water (STP)[l]	999.84	1.97	–	–	1402.4	–
Seawater (STP), 35% salinity[m]	1032.8	2.17	–	–	1449.1	–
Light oil (1 atm, 26 °C)[n]	750	1.15	–	–	1237	–
Heavy oil (1 atm, 26 °C)[n]	1037	2.71	–	–	1616	–
Tholeiitic basalt 1505 °K[o]	2650	17.9	–	–	2599	–
Andesite melt 1553 °K[o]	2440	16.1	–	–	2569	–
Rhyolite melt 1553 °K[o]	2310	13.5	–	–	2417	–

Unless otherwise indicated, the densities, adiabatic bulk moduli, and shear moduli are all from Bass (1995). The seismic velocities are calculated using eqns [1] and [2].

[a]From Table 4 of Ohno et al. (2006) at 575.5 °C.

[b]Densities from Smyth and McCormick (1995).

[c]See discussion in Cholach and Schmitt (2006).

[d]Value is the Voigt–Reuss–Hill average calculated assuming hexagonal symmetry (Watt and Peselni, 1980) using the values reported in Bass (1995).

[e]Value is the Voigt–Reuss–Hill average calculated assuming hexagonal symmetry (Watt and Peselni, 1980) using the values reported in Karmous (2011). See also Militzer et al. (2011) and Sato et al. (2005).

[f]Densities of a dry and saturated montmorillonite as updated by Chitale and Sigal (2000).

[g]Value is the Voigt–Reuss–Hill average calculated assuming hexagonal symmetry (Watt and Peselni, 1980) using the elastic stiffness calculated in Ebrahimi et al. (2012).

[h]Density and estimates of moduli in Bailey and Holloway (2000).

[i]Estimates from Auzende et al. (2006). See also Schmitt et al. (2007).

[j]From measurements described in Christensen (2004). See also recent modeling by Mookherjee and Stixrude (2009).

[k]From Lemmon et al. (2000).

[l]Online calculation Lemmon et al. (2012a) derived from the model of Wagner and Pruss (2002).

[m]From Wong and Zhu (1995) and Safarov et al. (2012).

[n]From ultrasonic measurements of Wang et al. (1990).

[o]Zero frequency (relaxed) estimates based on ultrasonic measurement of Rivers and Carmichael (1987) as reported in Bass (1995).

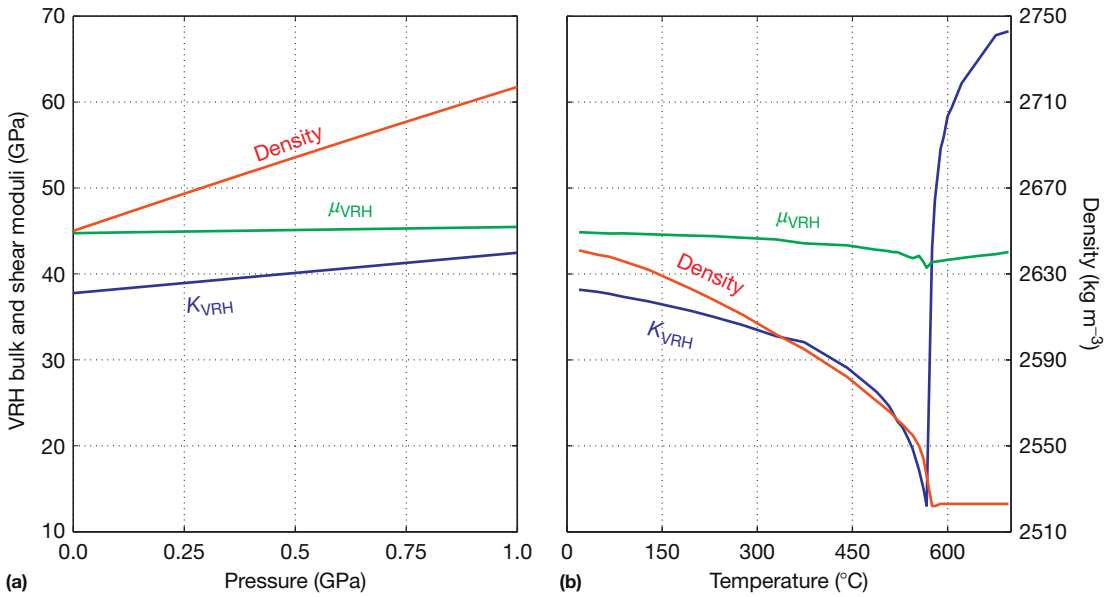

Figure 4 Changes in the averaged bulk K_{VRH} and shear μ_{VRH} moduli and density of an isotropic polycrystalline quartz aggregate (a) calculated as a function of pressure at constant temperature 298 °K (Calderon et al., 2007), The density as a function of pressure is calculated with values of $K_o = 37.7$ GPa, $dk/dP = 4.69$ Pa Pa^{-1}, and $\rho = 2650$ kg m^{-3} using the Birch–Murnaghan equation of state (Birch, 1947) (b) measured as a function of temperature at constant room pressure (Ohno et al., 2006). Note in (b) the influence of the solid state phase transition of α-quartz to β-quartz at 573.0 °C.

the mineral's crystal unit cell (Smyth and McCormick, 2013; Wohlenberg, 1982). The x-ray density $\rho_{x\text{-ray}}$ is then calculated with knowledge of the chemical molar molecular weight M in g mol^{-1} and its number of formula units per unit cell z:

$$\rho_{x\text{-ray}} = \frac{zM}{N_A V_{x\text{-ray}}} \quad [22]$$

where N_A is Avogadro's number (6.02214×10^{23}). These methods are particularly advantageous for the many minerals that do not exist in large crystal form and are then not amenable to the Archimedean or Boyle's law methods. Further, they can be used to determine density (and hence static bulk elastic properties) under conditions of pressure and temperature (Hemley et al., 2005).

iv. The electron bulk density ρ_e is calculated from estimates of the number of electrons per unit volume, n_e, from Compton scattering attenuation of x-rays (Schmitt et al., 2003):

$$\rho_e = \frac{n_p/Z}{N_A} M \quad [23]$$

where $n_e = n_p$ is the number of protons per unit volume and Z is the atomic number (i.e., number of electrons or protons in the electrically neutral molecule). This is no more than measuring the number of moles of the compound in a given volume.

The mass of a given atom is close to the sum of the masses of its constituent neutrons and protons. Neutrons and protons have nearly the same mass. Further, examination of the periodic table shows that there are equal numbers of neutron N and protons Z in the most common isotopes of elements that constitute the rock-forming minerals. It follows from this then that the ratio $M/Z \sim 2$ g mol^{-1} and eqn [23] may often be simplified to

$$\rho_e = (2\,\text{g mol}^{-1}) \frac{n_p}{N_A} \quad [24]$$

Equation [24] is often applied in geophysical well logging as it allows for an accurate estimate of the bulk density to be obtained even in the absence of detailed knowledge of the mineralogy.

Some of these measures of density are provided Table 2.

11.03.4 Fluid Properties

Pore fluids can strongly influence the overall seismic properties of rocks. Pore fluids contribute to the overall moduli and the bulk density of the rocks that they are contained in. Consequently, they must affect the seismic wave speeds through eqns [1] and [2]. In many respects, fluids are more interesting than solids because their density ρ_f, bulk modulus K_f, and phase state depend on pressure P and temperature T. These are the dependencies that allow, in part, for successful active seismic 'time-lapse' active seismic monitoring of fluid motions during hydrocarbon production (Bianco et al., 2010; Lumley, 2001; Schmitt, 1999) or greenhouse gas sequestration (White, 2013).

In order to forward model or to interpret observed seismic velocities through fluid-saturated rocks, one must then have a good knowledge of ρ_f and K_f with pressure P and temperature T. This P–V–T relationship, or equation of state (EOS), can take many forms depending upon the degree of sophistication required and whether it can account for phase transformations. Of course, this is a vast topic and only a cursory introduction can

be given here with particular focus on some key fluids that researchers would encounter including water, carbon dioxide, and methane. While as geophysicists we would prefer to be handed easily obtained values for the desired properties, this may not always be possible and some work may be required to obtain appropriate representative values. The reader should not necessarily look for quick answers here, but this contribution attempts to at least lead the way to the relevant literature where answers might be found. An important contribution of Batzle and Wang (1992), for example, has distilled some of these complex relations into more readily applicable formulas. Their equations have been incorporated into numerous fluid property calculators for use in seismic fluid substitution calculations; because they are so widely used, these too will be provided where appropriate. This section attempts to give some appreciation of how complicated and interesting fluid properties are, particularly relative to the more consistent minerals.

11.03.4.1 Phase Relations for Fluids

Before proceeding further, it is important to review the pressure and temperature dependencies of the fluid phase. Figure 5 shows the phase boundaries for water, carbon dioxide, and methane. Most workers are familiar with solids, liquids, and gases and the melting, sublimation, and boiling curves for the transitions between these phases. These are first-order phase transformations in that the internal energy and physical properties (Figure 6) are discontinuous. Via the latent heat of the transformation, additional energy is also released (exothermic) or absorbed (endothermic) during the phase change.

Many fluids of interest can also be in their supercritical fluid phase within the Earth. In the range of pore fluid pressures and temperatures encountered, free CO_2 and CH_4 are more likely than not to be in the supercritical regime. Supercritical H_2O exists at depth within volcanic systems, and it remains a target for geothermal power generation because of its lower viscosity but still considerable enthalpy (Fridleifsson and Elders, 2005). As illustrated in Figure 6, the transition from either gas or liquid to supercritical is continuous, and this transition is referred to as second (or higher)-order. Essentially, any surface tension between the liquid and vapor disappears under supercritical conditions, and this fluid is best characterized at the microscopic scale by rapidly fluctuating regions of density. Coherent light propagating through this fluid is scattered by the density fluctuations through a phenomenon referred to as critical opalescence. Otherwise, detecting when the fluid actually becomes supercritical can be difficult because of the lack of any discontinuity in the properties. Indeed, examination of the phase diagrams shows that it is possible to go from a gas to a liquid continuously by following a P–T trajectory around the critical point. The critical point values of temperature T_c, pressure P_c, and density ρ_c are provided for a few representative fluids in Table 3.

Note that 0.1 MPa is just <1 atmosphere of pressure and $°C = °K - 273.15°$.

11.03.4.2 Equations of State for Fluids

Again, in order to determine seismic wave speeds, eqns [1] and [2] demand knowledge of the moduli and density. Although it will become fully apparent later in Section 11.03.6, an overall saturated rock's bulk modulus K_{sat} and density ρ_{sat} will require knowledge of the fluid bulk modulus K_f and density ρ_f (or equivalently the specific volume $V_f = 1/\rho_f$). As Figure 6 shows,

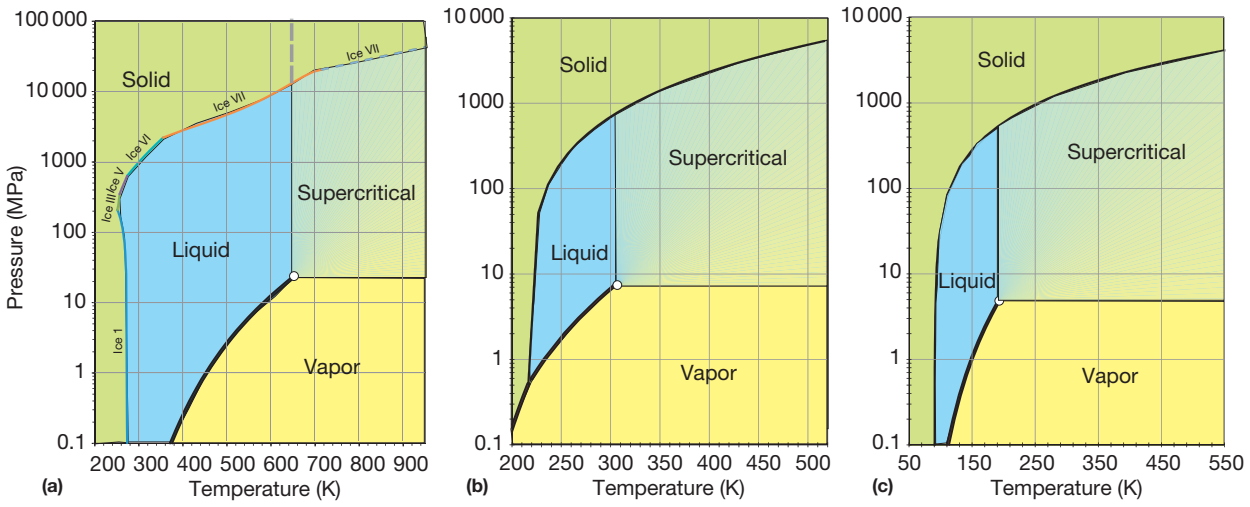

Figure 5 P–T phase diagrams for important relevant fluids. (a) Water phase diagram: The critical point shown as a white dot lies at $P_C = 22.064$ MPa and $T_C = 373.946$ °C (647.096 °K). The liquid–vapor phase boundary line is from the standard thermodynamic models (Wagner and Pruss, 2002) for water and calculated using the NIST web-based database (Lemmon et al., 2012b) and the solid–liquid/supercritical phase boundary calculated using the expressions developed by the IAPWS (2011); this boundary is only inferred past 775 K. (b) Carbon dioxide phase diagram: The critical point shown as a white dot lies at $P_C = 7.3773$ MPa and $T_C = 30.9782$ °C (304.1282 °K). The liquid–vapor phase boundary line is from the standard thermodynamic models for CO_2 (Span and Wagner, 1996) and calculated using the NIST web-based database (Lemmon et al., 2012b) and the melting and sublimation lines calculated using eqns [3.10] and [3.12] of Span and Wagner (1996). (c) Methane phase diagram: The critical point shown as a white dot lies at $P_C = 4.5992$ MPa and $T_C = -78.586$ °C (194.564 °K). The liquid–vapor phase boundary line is from eqn [3.2] and the melting curve from eqn [3.7] of Setzmann and Wagner (1991).

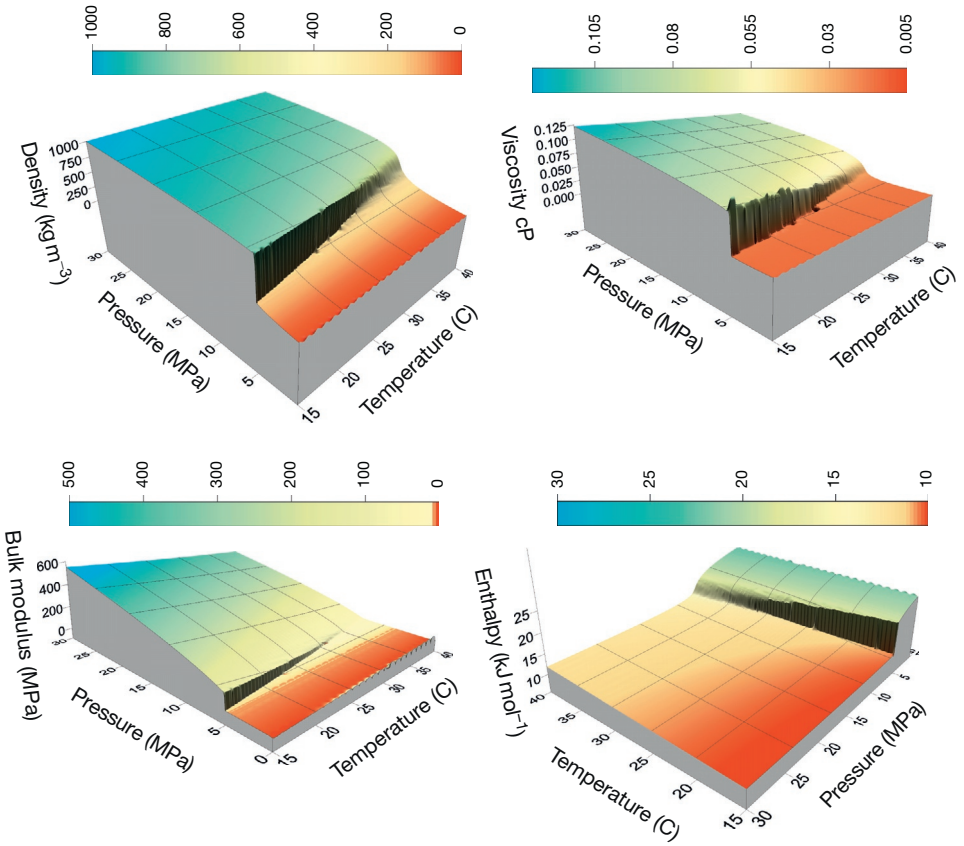

Figure 6 Dependence of the density, viscosity, bulk modulus, and enthalpy for CO_2 on pressure and temperature in the region around the critical point ($P_C = 7.3773$ MPa and $T_C = 30.9782\,^{\circ}$C (304.1282 °K)). Underlying data obtained from NIST online model (Lemmon et al., 2012b) using the model of Span and Wagner (1996).

Table 3 Thermodynamic properties of representative fluids

Molecule	*Critical temperature* T_c *(°C)*[a]	*Critical pressure* P_c *(MPa)*[a]	*Critical density (mol* m^{-3}*)*[a]	*Critical volume* ($m^3\,mol^{-1} \times 10^{-5}$)	*The van der Waals* a[b] *(Pa* ($m^3\,mol^{-1})^2$)	*The van der Waals* b[c] ($m^3\,mol^{-1} \times 10^5$)	*Acentric factor*	*Boiling point (°C)*
Water	373.946	22.064	17873.72	5.595	0.20719	1.8649	0.3443	99.974
Carbon dioxide	30.9782	7.3773	10624.9	9.412	0.19605	3.1372	0.2239	−78.4
Methane	−82.586	4.5992	10139	9.863	0.13421	3.2876	0.0114	−161.48
Propane	96.675	4.24766	5000	20.000	0.50971	6.6666	0.1524	−42.09
Decane	344.6	2.103	1640	60.976	2.34570	20.325	0.488	174.12
Benzene	288.90	4.894	3956.1	25.277	0.93810	8.4258	0.2092	80.08
Nitrogen	−146.958	3.3958	11183.9	8.941	0.08144	2.9804	0.0372	−195.79
Helium	−267.9547	0.22746	17399	5.747	0.00225	1.9158	−0.382	−268.92
Hydrogen	−240.005	1.2964	155508	0.643	0.00016	0.2143	−0.219	−252.78

[a]Data obtained from webbook.nist.gov/chemistry/fluid/.
[b]$a = 3P_cV_m^3$.
[c]$b = V_m/3$.

both are pressure- and temperature-dependent. The ρ_f maps a surface in the three-dimensional pressure–volume–temperature (P–V–T) space. This surface is mathematically described by the fluid's EOS. For our purposes, this means that ρ_f can be found if we know the *in situ* P and T. The bulk modulus K_f, however, requires the calculation of the volume-dependent derivative along the lines of either constant temperature (isotherms) or entropy (adiabats). Although in practice the simple EOS described may not always be adequate to describe real fluid behavior, it is useful to present them to provide some basic background on how density and bulk moduli may be determined. Some discussion of how one may find appropriate values is necessary, and to do this, a review of common EOS is required.

11.03.4.2.1 Ideal gas law

The simplest EOS is that for a perfect gas that considers the gas molecules to be point masses of no volume such that

$$PV_m = RT \quad [25]$$

where $R = 8.3144621(75575)\,\mathrm{J\,mol^{-1}{}^{\circ}K^{-1}}$ is the gas constant, V_m is the molar volume in $\mathrm{m^3\,mol^{-1}}$, and T is the temperature in degrees kelvin. Note that $\rho_f = 1/V_f = M/V_m$. The P–V_m relationship for a perfect gas law equation [25] is plotted for two temperatures in Figure 7, and at all temperatures, P simply decreases monotonically. Consequently, the perfect gas law is of limited value in rock physics as it only describes gas behavior at low densities and high temperatures. It cannot predict the existence of more condensed liquid or supercritical phases nor their properties.

11.03.4.2.2 Adiabatic and isothermal fluid moduli

A brief examination of eqn [25] illuminates some issues with regard to the fluid compressibility, and this brings us again to the issue of the adiabatic and isothermal bulk moduli first discussed for solids in Section 11.03.3.3. The general definition of the isothermal bulk modulus K_T for any material is

$$K_T = -V\left(\frac{\partial P}{\partial V}\right)_T = \rho\left(\frac{\partial P}{\partial \rho}\right)_T \quad [26]$$

The application of eqn [26] to the perfect gas EOS of eqn [25] yields $K_T = P$. However, as already stressed earlier, most seismic wave propagation phenomena occur adiabatically and are controlled by the adiabatic bulk modulus K_S. For an ideal gas, this is

$$K_S = -V\left(\frac{\partial P}{\partial V}\right)_S = \rho\left(\frac{\partial P}{\partial \rho}\right)_S = \frac{C_P}{C_V}K_T = \gamma K_T = \gamma P = \gamma\frac{RT}{V_M} \quad [27]$$

where the ratio of the heat capacities at constant pressure C_P and volume C_V is often called the adiabatic index γ. The value of γ depends on the degrees of freedom for the gases with $\gamma \approx 1.67$ for a monotonic gas (only three translational motions allowed) and $\gamma = 1.4$ for a diatomic gas (with two additional rotational degrees of freedom). Under adiabatic conditions, then $K_S = \gamma K_T = \gamma P$; and consequently, K_S and K_T can be considerably different for gases and many hydrocarbon fluids (Picard and Bishnoi, 1987). This translates to large differences in the wave speeds between adiabatic and isothermal conditions. Substituting $K_S = \gamma P$ into eqn [3] for the wave speed in a 'perfect' gas

$$V_L = \sqrt{\frac{\gamma P}{\rho_f}} \quad [28]$$

but more generally for nonideal fluids, one arrives at the Newton–Laplace eqn [3] rewritten here as

$$V_L = \sqrt{\frac{K_S}{\rho_f}} \quad [29]$$

For example, in dry air with $\gamma = 1.3998$ (Wong and Embleton, 1984), the adiabatic sound speed calculated using eqn [28] at 0 °C and 101.325 kPa (i.e., one standard atmosphere) is 331.29 m s^{-1} (±0.02%) in excellent agreement with

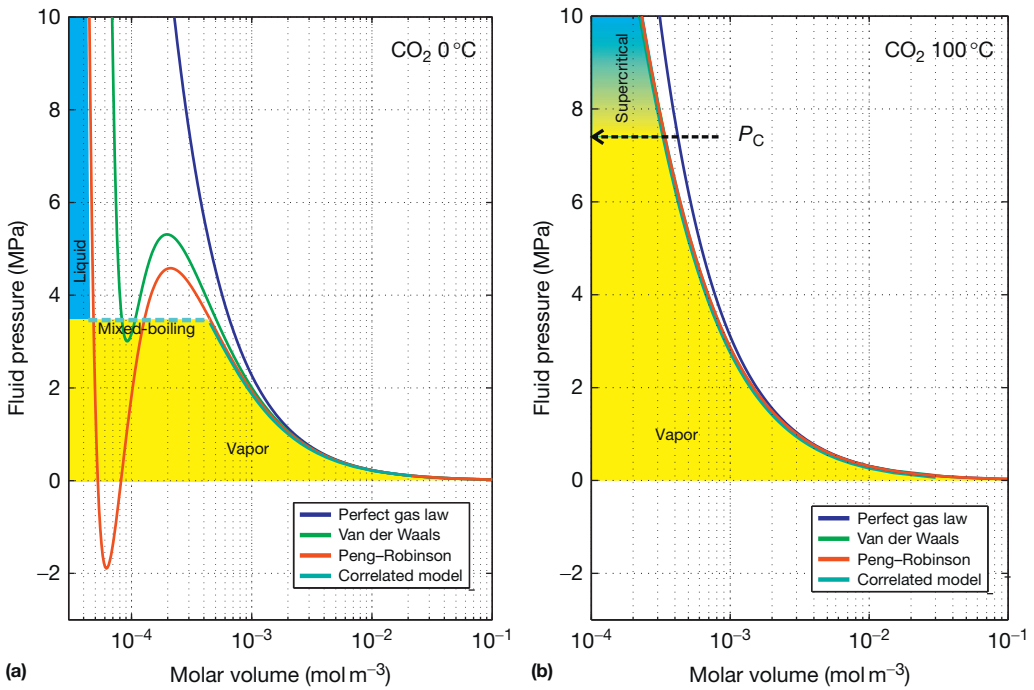

Figure 7 Comparison of different EOS for CO_2 for isotherms at (a) 0 °C and (b) 100 °C plotted in fluid pressure versus molar volume space. These include the perfect gas law eqn [25] (blue line), the van der Waals formula (eqn [32]), the Peng–Robinson equation [35] (with acentric factor = 0.22394), and the more sophisticated correlative models of Span and Wagner (1996) that directly specify phase. Filled color zones to the left of the curves indicate the various phases according to the correlative models of Span and Wagner (1996). Underlying data obtained from NIST online model (Lemmon et al., 2012b) using the model of Span and Wagner (1996).

experimental observations. In contrast, the isothermal sound speed first predicted by Newton would be only ~280 m s^{-1}.

As will be apparent later, an appropriate value for the fluid bulk modulus K_f is necessary to calculate the saturated rock properties. In the following discussions, we will assume that the fluid bulk modulus K_f that needs to be found is the adiabatic, or isentropic, bulk modulus K_S. It is worth mentioning that V_L as defined by eqn [29] is at low frequencies with the system at equilibrium a thermodynamic property in its own right; in the fluid physics and engineering communities, V_L is called the thermodynamic sound speed (Castier, 2011; Picard and Bishnoi, 1987).

Similarly to eqn [20], adiabatic and isothermal bulk moduli are related through

$$\frac{1}{K_S}=\frac{1}{K_T}-\frac{\alpha^2 T}{\rho C_P} \qquad [30]$$

where α is the coefficient of thermal expansion, T is the temperature in K, ρ is the density, and C_P is the isobaric (i.e., constant pressure) heat capacity (Clark, 1992; Kieffer, 1977).

11.03.4.2.3 The van der Waals model

The deficiencies of the perfect gas law of equation [25] were recognized early. In order to attempt to resolve these problems, van der Waals (1873) adapted eqn [25] by assigning the molecules a finite molar volume b and allowing them minor self-attractive 'van der Waals' forces to develop his EOS

$$\left(P+a/V_m^2\right)(V_m-b)=RT \qquad [31]$$

that may alternatively be displayed in its polynomial cubic form

$$V_m^3-\left(b+\frac{RT_c}{P_c}\right)V_m^2+\frac{a}{P_c}V_m-\frac{ab}{P_c}=0 \qquad [32]$$

Factor a describes the weak self-attraction of the gas molecules to one another, and a is proportional to the liquid's vaporization energy. Factor b is roughly equivalent to the molar volume of the liquid. These constants may be found from the fluid's T_c and P_c:

$$a=\frac{(RT_c)^2}{64P_c}\qquad b=\frac{RT_c}{8P_c} \qquad [33]$$

The reader will note in Figure 7 that the isotherm of the van der Waals curve at 0 °C (i.e., below the critical temperature T_c where two phases can exist at a given pressure) displays cubic behavior with three possible real roots. The smallest and largest solutions provide the molar volumes of the liquid and the vapor, respectively, while the intermediate root has no real physical meaning. At sufficiently high temperatures or at low pressures, only one real root exists. While not obvious to the more casual reader, this shape allows for the prediction of liquid, gas, and supercritical regimes. The real fluid does not follow the trajectory in the region of the function's trough and peak, which is actually a mixed-phase region where the liquid and vapor coexist until either condensation or boiling is complete. Castellan (1971) contains a particularly clear discussion of the information that may be obtained from the van der Waals curves that are beyond the scope of the discussion here. Carcione et al. (2006) had applied the van der Waals formula to obtain appropriate fluid moduli and density for use in modeling of the seismic behavior of CO_2 saturated rocks.

11.03.4.2.4 The Peng–Robinson EOS

The development of the van der Waals equation [31] was a major improvement over the perfect gas law equation [25], but as examination of Figure 7(a) shows, it is not at all accurate in the fluid state; and a plethora of additional formulas have been developed to overcome this to varying degrees of complication. The Peng and Robinson (1976) modification to the van der Waals formula

$$\left(P+\frac{\alpha_{PR}a_{PR}}{V_m^2+2b_{PR}V_m-b_{PR}^2}\right)(V_m-b_{PR})=RT \qquad [34]$$

remains one of the most popular in that it retains much of the simplicity of the van der Waals EOS but provides better estimates of the P–V–T relations. In eqn [34], there are three factors that are obtained from tabulated values that include the Peng–Robinson a_{PR} and b_{PR}

$$a_{PR}=0.45724\frac{(RT_c)^2}{P_c}\qquad b_{PR}=0.07780\frac{RT_c}{8P_c} \qquad [35]$$

and the acentric factor ω that accounts for nonsphericity of the molecule (Bett et al., 2003). The effects of the acentricity and temperature are included in α_{PR}:

$$\alpha_{PR}=\left[1+\left(0.37464+1.5422\omega-0.26992\omega^2\right)\left(1-\sqrt{T/T_c}\right)\right]^2 \qquad [36]$$

The cubic form of the Peng–Robinson equation [34] is most often for simplicity given in terms of the compressibility factor $Z=PV_m/RT$ with

$$Z^3-(1-B)Z^2+\left(A-3B^2-2B\right)Z-\left(AB-B^2-B^3\right)=0 \qquad [37]$$

where

$$A=\frac{a_{PR}P}{(RT)^2}\qquad B=\frac{b_{PR}P}{RT} \qquad [38]$$

and, as for the van der Waals equation, in the two-phase region below T_c, the largest and smallest roots correspond to the vapor and liquid molar volumes, respectively.

The Peng–Robinson equation [34] predicts well the P–V–T relationship for in the vapor and supercritical regimes. The liquid properties are not as precise but depending on the application may be sufficient. In Figure 7, for example, the Peng–Robinson EOS value for V_m at the boiling point exceeds that observed by about 7%. It too shows cubic behavior below T_c and the same arguments used for the van der Waals equation [32] hold. The Peng–Robinson equation [34] was a seminal development, and a very large literature of adaptations and additional corrections to it has emerged. It is particularly heavily used in the petroleum industry to describe P–V–T relations of both *in situ* and produced hydrocarbons.

11.03.4.2.5 Correlative EOS models

The best models, at least for monomolecular fluids, are those constructed by fitting of actual observed experimental measurements. As such, these correlative models rely on the existence of solid experimental observations of P–V–T relations and phase boundaries and of course can only be as good as the quality of the data and are limited by the ranges of conditions over which measurements have been made (Setzmann and Wagner, 1989). Models exist for important geophysical fluids including water (Wagner and Pruss, 2002), CO_2 (Span and Wagner, 1996; see also Han et al. (2010, 2011)), and methane (Kunz and Wagner, 2012; Setzmann and Wagner, 1991). The formulas used in these models are extensive and are not repeated here as they are lengthy and dependent on the phase state. The correlative model for CO_2 is shown as the 'reference' against which the other simpler models are compared in **Figure 7**. Online calculation of isotherms (P–V–T paths of constant temperature), isobars (P–V–T paths of constant pressure), and isochors (P–V–T paths of constant volume or density) is available from Lemmon et al. (2012b) for a number of important fluids. Independent software for water properties may also be found for water (NIST, 2010b) and for other fluids and mixtures of interest to geophysics (NIST, 2010a).

Pure water has been extensively studied and numerous less complicated expressions exist with validity over more limited ranges of P and T and a large literature exists. A few of the contributions in this area for liquid water in include those of Del Grosso and Mader (1972) and Kell (1975).

Batzle and Wang (1992) provided a number of simplified equations for the acoustic properties of water based on earlier experimental work of many authors (Helgeson and Kirkham, 1974; Rowe and Chou, 1970; Wilson, 1959). For example, based on Rowe and Chou's (1970) compilation, they derived a formula for the density of pure water ρ_w (in g cm^{-3}) as a function of pressure P (in MPa) and temperature T (in °C)

$$\rho_w = 1 + 10^{-6}(-80T - 3.3T^2 + 0.00175T^3 + 489P - 2TP + 0.016T^2P - 1.3\times10^{-5}T^3P - 0.333P^2 - 0.002TP^2) \quad [39]$$

and provided Wilson's (1959) empirical regression for the speed of sound V_w (longitudinal wave in m s^{-1}) in pure water

$$V_w = \begin{bmatrix}1 & P & P^2 & P^3\end{bmatrix}\begin{bmatrix}w_{00} & w_{10} & w_{20} & w_{30} & w_{40}\\ w_{01} & w_{11} & w_{21} & w_{31} & w_{41}\\ w_{02} & w_{12} & w_{22} & w_{32} & w_{42}\\ w_{03} & w_{13} & w_{23} & w_{33} & w_{43}\end{bmatrix}\begin{bmatrix}1\\ T\\ T^2\\ T^3\\ T^4\end{bmatrix} \quad [40]$$

with the coefficients w_{ij}

$$\begin{bmatrix}w_{00} & w_{10} & w_{20} & w_{30} & w_{40}\\ w_{01} & w_{11} & w_{21} & w_{31} & w_{41}\\ w_{02} & w_{12} & w_{22} & w_{32} & w_{42}\\ w_{03} & w_{13} & w_{23} & w_{33} & w_{43}\end{bmatrix} = \begin{bmatrix}1402.85 & 4.871 & -0.04783 & 1.487\times10^{-4} & -2.197\times10^{-7}\\ 1.524 & -0.0111 & 2.747\times10^{-4} & -6.503\times10^{-7} & 7.987\times10^{-10}\\ 3.437\times10^{-3} & 1.739\times10^{-4} & -2.135\times10^{-6} & -1.455\times10^{-8} & 5.230\times10^{-11}\\ -1.197\times10^{-5} & -1.628\times10^{-6} & 1.237\times10^{-8} & 1.327\times10^{-10} & -4.614\times10^{-13}\end{bmatrix} \quad [41]$$

Wilson's equation [40] may be adequate for fluid substitution use under field conditions (Chen and Millero, 1976), whereas in the laboratory, the more recent correlation models (Lemmon et al., 2012a; Wagner and Pruss, 2002) or more recent formulas (Belogol'skii et al., 1999; Lin and Trusler, 2012; Vance and Brown, 2010) may be preferable if greater accuracy is desired. That said, the adiabatic bulk modulus predicted using eqns [39] and [40] from Batzle and Wang (1992) agrees well with other models (**Figure 8**).

11.03.4.2.6 Determining K_f from equations of state

Ideally, the best way to obtain the adiabatic fluid bulk modulus K_f is from direct determinations of the sound speed and density in the fluid subject to the appropriate P–T conditions (Clark, 1992; Picard and Bishnoi, 1987). Equations [26] and [27] provide the definitions of the isothermal K_T and adiabatic K_S bulk moduli as the partial derivative of P with V_m. In principle then, one may simply obtain K_T or K_S by appropriately differentiating, respectively, either an isotherm (such as shown in **Figure 7**) or a corresponding adiabat. This is done relatively easily for the isotherms for which we can write explicit equations as in the preceding text, and, ignoring imperfections in the EOS itself, K_T can then be easily obtained. Unfortunately, for purposes of seismic wave propagation, K_S is the one required as discussed in **Section 11.03.3.3**. From the EOS, K_S can be determined in different ways:

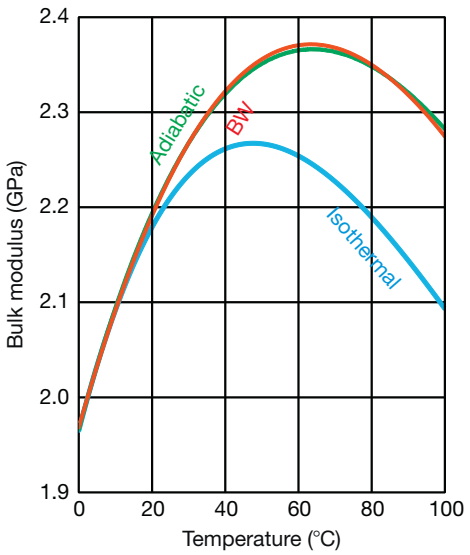

Figure 8 Comparison of the bulk moduli of liquid water at 1 atmosphere from 0 to 100 °C for (i) isothermal K_T (blue line) calculated using expressions in Kell (1975), the adiabatic K_S (green line) as calculated from the correlative model sound speeds and densities from Lemmon et al. (2012b), and a second adiabatic K_S (red line) calculated from the Batzle and Wang (1992) formulas for density (eqn [40]) and sound speed (eqn [41]). Note that the peak in the bulk moduli arises from the unique behavior of water.

i. Assuming that the differences are small such that $K_S \approx K_T$. This may be true in some cases, but even for liquid water at 1 atmosphere, the two deviate above 20 °C (**Figure 8**). This assumption becomes even more problematic for hydrocarbon fluids. In practical interpretation of seismic data, the errors in determining seismic velocities may be greater than the differences produced by using K_T, but workers should still take care when assuming K_T is sufficient.
ii. Obtaining K_T by derivation of the isotherm and then applying eqn [30] assuming appropriate knowledge of C_P and α. One problem with this approach is that the knowledge of these parameters may be incomplete or erroneous.
iii. Numerically converting the P–V isotherms to P–V isentropes and taking the derivative of these directly (Picard and Bishnoi, 1987). Again, this approach can be fraught with additional error. Clark (1992) noted that this may be the only way to obtain a value for K_S particularly for complex multiphase fluids but it should be recognized that the EOSs are usually imperfect (as demonstrated in **Figure 7**). She recommended that, if possible, workers should find K_S by measuring the sound speeds in the fluids directly with eqn [29]. Plantier et al. (2008) also echoed this caveat on the direct application of thermodynamic relations to predict wave speeds or bulk moduli in heavy oils.

An alternative strategy to calculate the isentropic compressibility and hence the fluid's thermodynamic sound speed has recently been developed by Nichita et al. (2010). They obtained the relevant parameters from partial derivatives of the total enthalpy with respect to temperature at constant pressure and composition.

11.03.4.3 Mixtures and Solutions

The discussion in the preceding text focuses primarily on simple fluids with a single chemical component, but in the Earth, this will rarely be the case. Pore waters are never pure and usually contain numerous solvated ions and absorbed gases (van Weert and van der Gun, 2012). Hydrocarbon-saturated rocks actually contain a complex mixture of different organic species mixed both miscibly and immiscibly, with water and free gas often residing separately from the oil in the same pore. Perhaps most importantly, the pore space can hold the fluid in pockets of liquids and gas, a mixture with unexpected mechanical properties (the so-called 'patchy' saturation). Consequently, we must look at the topic of fluid mixtures from a number of different perspectives as solutions, mixtures of immiscible fluids, and mixed phases.

11.03.4.3.1 Frozen mixtures

'Frozen' fluid mixtures can consist of either (i) a mix of immiscible and nonchemically interacting fluids or (ii) a mix of vapor and liquid phases of the same fluid, the proportions of which do not vary during passage of the seismic wave. In his classic text, Wood (1955) developed the formula for the wave speed in a bubbly fluid with liquid and gas phases in proportions of ϕ_l and ϕ_g, respectively, and of bulk moduli K_l and K_g, respectively (Wilson, 2005),

$$V_f = \sqrt{\frac{1}{\left(\phi_l \rho_l + \phi_g \rho_g\right)\left(\phi_l / K_l + \phi_g / K_g\right)}} \qquad [42]$$

where he assumed no chemical interaction between the phases and that the Laplace surface tension pressure in the gas bubbles was negligible (i.e., the bubbles were sufficiently large approximately >0.1 mm in water). By analogy to eqn [29], the bulk modulus is

$$K_f = \left(\phi_l / K_l + \phi_g / K_g\right)^{-1} \qquad [43]$$

In the rock physics literature, eqn [43] has been extended to mixtures of n fluids and further generalized to include suspended solids within the liquid. It is often assumed to be an exact representation:

$$K_f = \left(\sum_{i=1}^{n} \phi_i / K_i\right)^{-1} \qquad [44]$$

For purposes of illustration and following Wood's example, consider a mixture of air and water. The density of the mixture increases linearly from that for air to that for water but its bulk modulus remains much closer to that for air and only rises to that for water in at near 100% water content (**Figure 9(a)**). Conversely, a few bubbles within the water have a large influence on diminishing the mixture's bulk modulus. This leads to the unexpected result that the wave speed in the mixture is substantially less than that in either air or water (**Figure 9(b)**), a consequence of the competition between stiffness and density in eqn [3].

As noted, the results of **Figure 9** obtained using Wood's equation [42] are presumed to be valid at low frequencies, but the formula is applied nearly universally in the geophysical literature. Nichita et al. (2010) had recently questioned even this assumption. In reality, the physics of the problem is quite complex with numerous additional considerations needing to be accounted for including changes to the bulk modulus of the gas due to Laplace internal pressure in the bubbles (e.g., Kieffer, 1977; Landau and Lifshitz, 1959) and of dispersion due to a wide variety of thermal and mechanical factors (Carey and Evans, 2011), the literature of which is too large to review here.

One of the more popular models that considers wave speed dispersion is that of Commander and Prosperetti (1989). This model includes the bubble size and corresponding resonance frequency, thermal diffusivity, and the Laplace bubble pressure. Because of these factors, this model is able to determine both mixture wave speed and attenuation with frequency. This model, too, has another unexpected result that, while Wood's equation [42] appears to predict the velocities well for this case below a few hundred Hz, above the resonance frequency for the bubbles, the stiffness of the mixture increases dramatically with surprisingly unexpected wave speeds above 15 000 m s^{-1} (**Figure 10**). Cheyne et al. (1995) provided a heuristic description of this phenomenon. The minimum near 3 kHz is at the bubble resonance frequency; and the subresonant ('Wood's regime') and superresonant regimes will shift left and right as the mean bubble dimensions increase and decrease, respectively. The point of showing these phenomena is not so

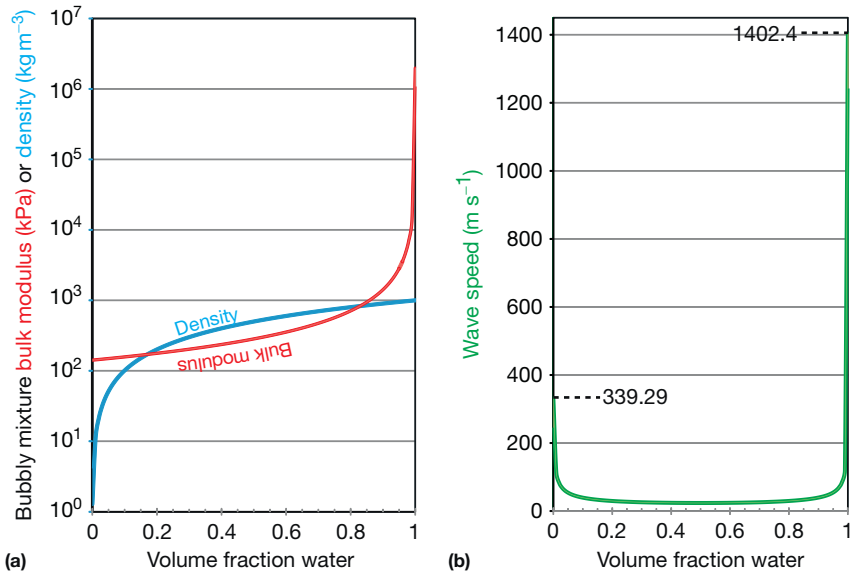

Figure 9 Properties of a bubbly mixture of air and water as a function of the volume fraction of water at 101.325 kPa and 0 °C. (a) Mixture density (eqn [21]) and bulk modulus (eqn [44]) on logarithmic scale. (b) Corresponding longitudinal wave speed in the bubbly mixture with the limits for air (339.29 m s^{-1}) and water (1402.4 m s^{-1}) shown. Calculations assume $K_{air} = 141.8$ kPa, $K_w = 1.966$ GPa, $\rho_{air} = 1.232$ kg m^{-3}, and $\rho_w = 999.84$ kg m^{-3}.

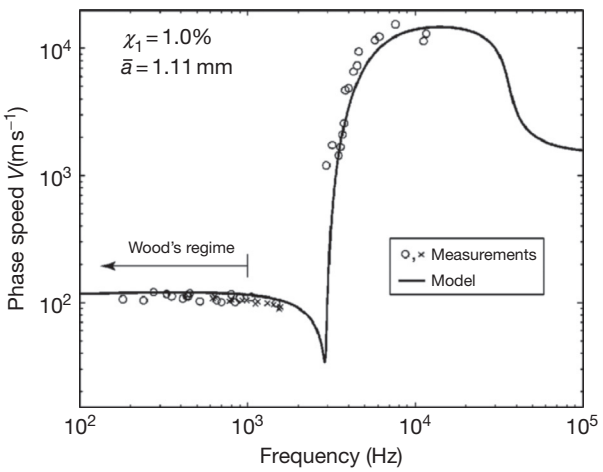

Figure 10 Observed (Cheyne et al., 1995; Wilson, 2005) and calculated (Commander and Prosperetti, 1989) wave speed dispersion in a mixture for a mean bubble radius of 1.11 m and a gas fraction air = 0.01. Reproduced from Wilson PS (2005) Low-frequency dispersion in bubbly liquids. *Acoustics Research Letters Online (ARLO)* 6: 188–194.

much that we may be interested in the wave speed of the mixture itself but that the fluid mixture's bulk moduli can be frequency-dependent. Consequently, some care may need to be exercised in the use of the otherwise ubiquitously applied general Wood's equation [44]. It is also important to note that dispersion exists even in the low-frequency Wood's regime but this is masked by the logarithmic scaling in Figure 10.

11.03.4.3.2 Miscible fluid mixtures

Miscible fluid mixtures are also very common within the Earth. Natural oils, for example, are really a complex blend of a multitude of different hydrocarbon compounds, and the 'heavier' (denser) and more viscous the oil, the greater the number of compounds that can occur in it. Brines are by far the most common liquids in both sedimentary basins and the crystalline crust, and their properties differ from those for pure H_2O. Molecules that would by themselves be gases, particularly CO_2 or CH_4, go into solution in both H_2O and oils. In this section, we will briefly review a number of these different types of miscible mixtures.

11.03.4.3.2.1 Brines

Solutions of water and, mostly, NaCl are the predominant fluids within the Earth's crust in both sedimentary basins and crystalline hard rocks. Brines have engendered a large literature primarily because of the need for information by a number of disciplines on their physical properties. Work on this topic continues to the present day with a standardized formula provided (IAPWS, 2008) and an alternative scheme developed by Del Grosso (1974) being the most popular descriptions of brine behavior. While the salt composition of seawater may remain globally consistent, brines in the Earth can contain numerous different electrolytes with wide concentrations affecting both the liquid density and bulk modulus. The density of the solution invariably increases with salinity, often given as some fractional measure such as ppt (referring to g of salt per kg of pure water) as illustrated for a 30 ppt brine compared with pure water in Figure 11. The trough in the bulk modulus near 50 °C is again apparent.

Numerous simple polynomial expressions describe the sound speeds and densities of seawater as a function of depth, salinity, and temperature (Coppens, 1981; Mackenzie, 1981; Safarov et al., 2009). Following from eqns [39] and [40], Batzle and Wang (1992) constructed fits of existing data for brine density ρ_B

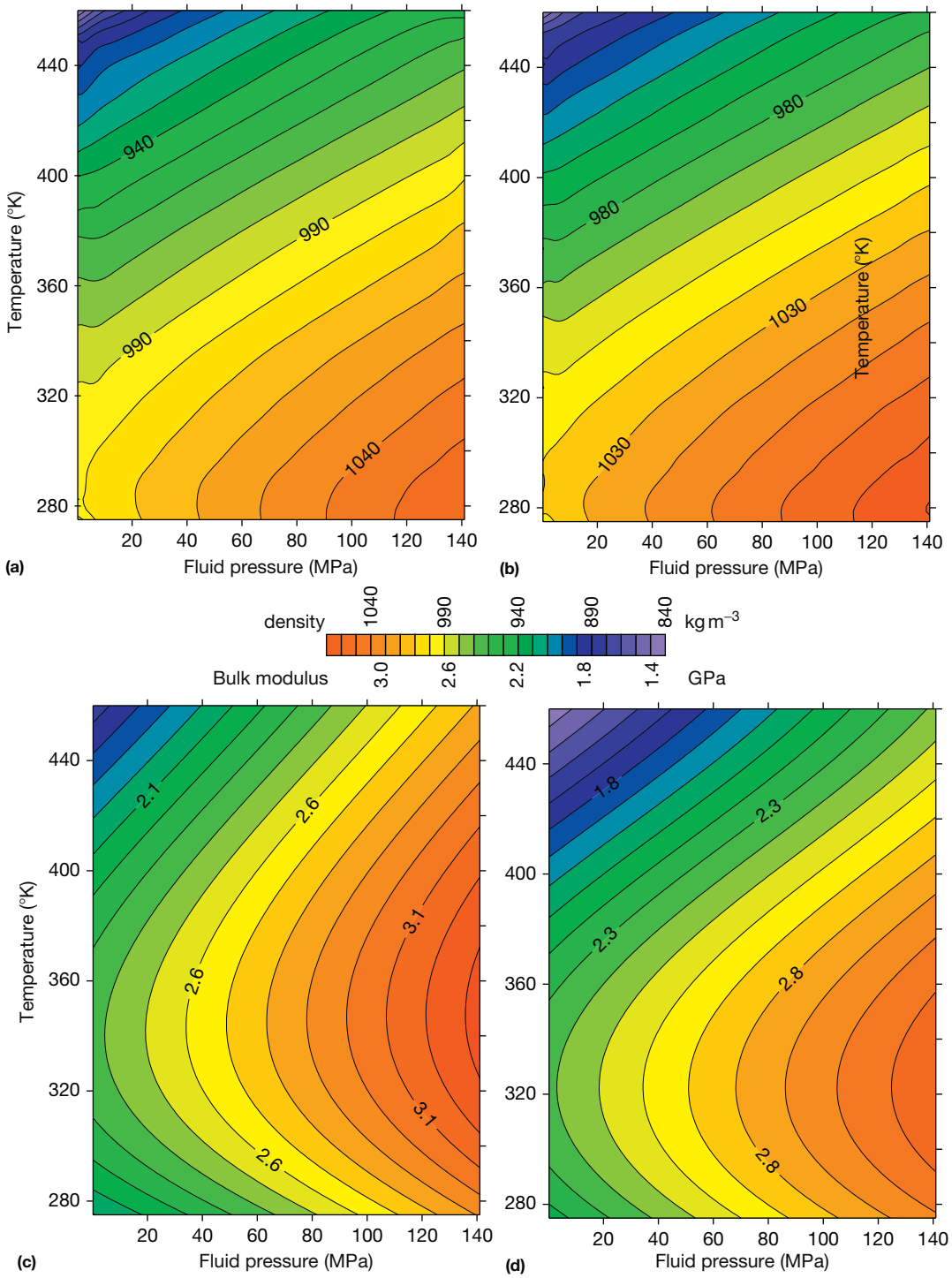

Figure 11 Comparison of the density of (a) pure water (Wagner and Pruss, 2002) and of (b) brine with a salinity of 30 ppt (g salt per kg water) (Safarov et al., 2013) contoured over the (P, T) region of 275–460°K and 0.2–140 MPa. Comparison of the (c) adiabatic bulk modulus of pure water with the (d) isothermal bulk modulus of the same 30 ppt brine (Safarov et al., 2013) over the same pressure and temperature conditions. Note that based on knowledge of the specific heat capacity of seawater (Sharqawy et al., 2010), the differences in the adiabatic and isothermal bulk moduli for seawater are significant for brines also.

$$\rho_B = \rho_w + S1\left(0.668 + 0.44S + 10^{-6} \times [300P - 2400PS + T(80 + 3T - 3300S - 13P + 47PS)]\right) \quad [45]$$

and sound speed V_B

$$V_B = V_w + S\left(1170 - 9.6T + 0.055T^2 - 8.5 \times 10^{-5}T^3 + 2.6P - 0.0029TP - 0.0476P^2\right) + S^{1.5}\left(780 - 10P + 0.16P^2\right) - 820S^2 \quad [46]$$

where S is the salinity in terms of the weight fraction in ppm/10^6. They noted that these were for NaCl concentrations and could be in significant error for other electrolytes particularly with divalent anions.

The lack of information on the properties of more concentrated brines is an important gap in our knowledge. The extensive work of Safarov et al. (2013) only reaches 30 ppt, but *in situ* natural brines can reach full salt saturations with salinities approaching 300 ppt. Data at higher concentrations are more difficult to find, but some appropriate density information might be obtained to 5.5 molal (320 ppt) in Rogers and Pitzer (1982), Gucker et al. (1975), and LaLiberte and Cooper (2004). Formation waters in the Earth too also can have quite different compositions than seawater, with a wide variety of ions including the cations Na^+, Ca^{2+}, Mg^{2+}, Fe^{2+}, K^+, Ba^{2+}, Li^+, and Sr^{2+} and anions Cl^-, SO_4^{2-}, HCO_3, CO_3^{2-}, NO_3^-, Br^-, I^-, and S^{2-}. Kumar (2003) measured wave speeds in KCl solutions but there is little in the literature on the effect of these ions on the acoustic properties of the solution. These few citations are in no way intended to be exhaustive, and there are many contributions that discuss the properties of brines. However, most of the work is performed under conditions, particularly of pressure, that are below what is needed *in situ*, and workers may need to take care in regard to the range of applicability of a given formulation.

11.03.4.3.2.2 Multicomponent fluid mixtures

Multicomponent mixtures in this section refer to miscible combinations of different gases and liquids, that is, a single-phase solution that is formed from two or more fluids. Carbonated water is one example. Natural hydrocarbon oils are another; they are quite complex and will literally contain thousands of different molecules. Indeed, we expect that such mixtures are likely the rule, not the exception, within the Earth. Such mixtures have many of the same characteristics as the pure fluids described in the preceding text, but with significant complications.

In addition to pressure P, volume V, and temperature T, the proportions x_i of the different fluids in the mixture and their respective solubilities must also now be considered. As such, the literature on the study of the behavior of such mixtures is immense and the field remains an active area of research.

Consider a mixture of two fluids A and B. The phase diagram of this multicomponent system in Figure 12 is broadly similar to that for the single components shown in Figure 5 except for the zone in P–T space separating the pure fluid and the vapor phases from one another. For the pure compounds of Figure 5, this boundary is only a line. For a miscible mixture in Figure 12, the boundary instead becomes an area in P–T space in which both liquid and vapor coexist. This

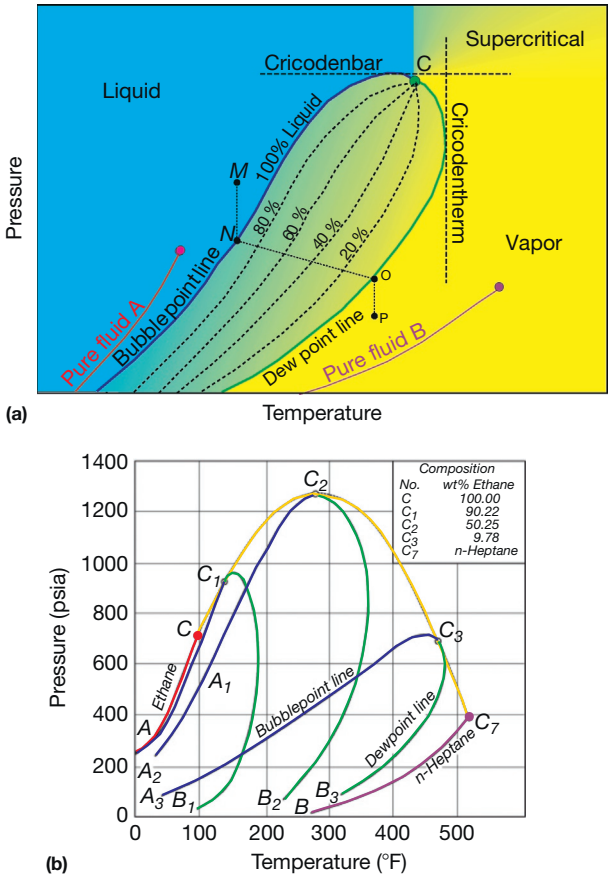

Figure 12 (a) Illustration of the phase boundaries for a 50–50 multicomponent mixture of pure fluids *A* and *B* with liquid, vapor, and supercritical regions adapted from Ezekwe (2010). The boiling lines and critical points for the two pure fluids are shown in red and green for fluids *A* and *B*, respectively. Point C is the pseudocritical point for the mixture. Percentages represent the saturation proportions of liquid to gas in the mixed-phase region between the bubble and dew point lines. (b) Mixed-phase envelopes for various proportions of ethane and *n*-heptane. The single-component boiling lines for ethane and *n*-heptane are shown in red and purple, respectively, in analogy to (a). The phase curves for three differing mixture compositions 1, 2, and 3 are shown with the bubble and dew point lines in blue and green and with their corresponding pseudocritical point. The yellow line is an envelope of the critical points and highlights the compositional dependence of the mixture's critical points. Adapted from Ezekwe N (2010) *Petroleum Reservoir Engineering Practice*. New York: Prentice Hall; Figure 4.5.

mixed-phase zone lies between the single-component boiling lines of the two pure fluids *A* and *B*.

For purposes of illustration, it is useful to follow the changes of a 50–50 mixture of two fluids along a hypothetical path *M*–*N*–*O*–*P* in *P*–*T* space in Figure 12. At *M*, the mixture is a homogeneous liquid. It remains a homogeneous liquid with decreasing pressure until point *N* is reached. Here, the path meets the bubble point line whereupon the first trace of vapor phase appears. From the appearance of this first gas bubble at *N*, the phase transformation progresses with varying saturations (i.e., proportions of liquid to gas) as one travels from *N* to *O*. At *O*, called the dew point, the last vestige of liquid phase remains. Past the dew point *O* and downward in pressure to *P*, the fluid is a homogenous vapor.

The pseudocritical point C in Figure 12 (Kay, 1936) lies where the bubble and dew point lines meet at pressure P_{PC} and temperature T_{PC}. Note that C lies above the critical points for pure A and B. The envelope of the mixed-phase boundary (i.e., the line that includes both the bubble and dew point lines) further complicates the phase behavior. Unlike the single-component fluid, C is not the limiting point at which multiple phases can exist. Consequently, the cricondenbar and the cricondentherm are the pressure and temperature limits, respectively, at which both liquid and vapor coexist. At pressure above the cricondenbar, the mixture can only be in liquid or supercritical states. At temperatures above the cricondentherm, it must be vapor or supercritical.

The location of C and the shape of the mixed-phase envelope change with the miscible fluid composition as illustrated for a real mixture in Figure 12(b). The behavior must approach that of the pure end-member as the proportions of the fluids move towards 100%. The P–T phase diagrams for various proportions of the hydrocarbon mixture of ethane (C_2H_6) and n-heptane (C_7H_{16}) show the evolution of the envelope as the proportions of the two fluids vary. The position of the pseudocritical point relative to the cricondenbar, too, varies. The yellow line in Figure 12(b) maps the locus of the pseudocritical points. It is worth noting that for the ethane/n-heptane mixture, this line is continuous between the critical points for pure ethane and n-heptane. Vankonynenburg and Scott (1980) classified this as a class I binary phase diagram (Gray et al., 2011).

The class I phase diagram of Figure 12 exemplifies the behavior of mixtures of organic liquids and particularly natural hydrocarbon oils. As noted, this is a vast topic in the hydrocarbon energy industry as such knowledge is required at nearly every point from initial production to refining. An understanding of such curves is necessary for purposes of seismic monitoring over oil reservoirs. For example, the fluid pressure in an oil field declines as fluids are produced. If this pressure decline followed a hypothetical path downward leading from point M, the pressure must eventually reach the bubble point where vapor comes out of solution. The fluid is now mixed-phase, and its overall bulk modulus drastically decreases similar to the behavior for air bubble water as shown in Figure 9. As will be seen later, this change in the fluid properties affects the overall saturated bulk modulus with a consequent decrease in both the rock's wave speed and elastic impedance. This changes the overall reflectivity of the structure with a detectable change (Fereidoon et al., 2010). Similarly, heating of liquid heavy oils to lower their viscosity and enhance their producibility would also result in the bubble point of the hydrocarbon mixture being reached with the consequential change in the seismic responses.

There are a number of resources that practitioners can exploit to obtain appropriate moduli and density. The GERG-2008 (Kunz and Wagner, 2012) model calculates the properties for hydrocarbon mixtures and it includes 21 different common components of natural gas. The software that carries out these calculations is available (Wagner, 2013). Although this is a sophisticated model, its authors still argue that new experimental data are necessary.

Batzle and Wang (1992) also provided useful approximate formulas for hydrocarbon mixtures. In their developments, a gas mixture is characterized simply only by its specific gravity G, the ratio between the gas mixture density ρ_g and that of air ρ_{air}

$$G = \frac{\rho_g}{\rho_{air}} \quad [47]$$

measured at 1 atmosphere of pressure and 15.6 °C. Following Thomas et al. (1970) and using a Benedict–Webb–Rubin EOS model (Benedict et al., 1942, 1951), they defined pseudo-reduced temperature T_{PR} and pressure P_{PR}, both of which can be related to G according to

$$P_{PR} = P/P_{PC} = P/(4.892 - 0.4048G) \quad [48]$$

$$T_{PR} = T^K/T^K_{PC} = T^K/(94.72 + 170.75G) \quad [49]$$

where the superscript K in eqn [49] indicates that the temperatures must be the absolute temperatures in degrees kelvin (T^K (°K) = T (°C) + 273.15). With these variables, the gas mixture's density ρ_g at P and T is approximately given by

$$\rho_g \cong \frac{28.8GP}{zRT^K} \quad [50]$$

where z is

$$z = \left[0.03 + 0.00527(3.5 - T_{PR})^3\right]P_{PR} + 0.642T_{PR} - 0.007T^4_{PR} - 0.52 + 0.109(3.85 - T_{PR})^2 \exp\left\{-\left[0.45 + 8(0.56 - 1/T_{PR})^2\right]P^{1.2}_{PR}/T_{PR}\right\} \quad [51]$$

The adiabatic bulk modulus K_S for this mixture may also be estimated as

$$K_S \cong \frac{P}{\left(1 - \frac{P_{PR}}{Z}\frac{\partial z}{\partial P_{PR}}\right)_T} \times \left\{0.85 + \frac{5.6}{P_{PR} + 2} + \frac{27.1}{(P_{PR} + 3.5)^2} - 8.7\exp[-0.65(P_{PR} + 1)]\right\} \quad [52]$$

with the derivative $\partial z/\partial P_{PR}$ taken at constant temperature calculated from eqn [51].

Batzle and Wang (1992) also gave expressions for estimating the density and bulk modulus of oils. As already noted, natural petroleum oils are composed of numerous different organic compounds, and, as was done with natural gas in eqn [47], these natural oils can be characterized by their density ρ_o, again measured at 15.6 °C and atmospheric pressure. They developed expressions for the pressure and the temperature dependence of the density of such oils (in g cm^{-3})

$$\rho = \frac{\rho_o + (0.00277P - 1.71 \times 10^{-7}P^3)(\rho_o - 1.15)^2 + 3.49 \times 10^{-4}P}{0.972 + 3.81 \times 10^{-4}(T + 17.78)^{1.175}} \quad [53]$$

that lead to the adiabatic bulk modulus

$$K_S \cong \rho\left\{2096\left(\frac{\rho_o}{2.6 - \rho_o}\right)^{1/2} - 3.7T + 4.64P + 0.0115 \times \left[4.12\left(\frac{1.08}{\rho_o} - 1\right)^{1/2} - 1\right]TP\right\}^2 \quad [54]$$

Live oils are oils containing gas in solution. As Figure 12 suggests, this gas will come out of solution upon depressurization at the bubble point N; and consequently, the composition and physical properties of a produced oil may be significantly different from its *in situ* precursor (Clark,

1992). Batzle and Wang (1992) also considered the case of live oils and provided additional relationships to eqns [53] and [54] for such cases. They suggested, however, that additional work is necessary.

As noted by Clark (1992), the best way to obtain appropriate information is to directly measure sound speeds in the oils themselves. This approach can provide a great deal of thermodynamic information but it remains quite rare. Wang and coworkers carried out numerous measurements of the wave speeds in oils at ultrasonic frequencies and observed their variation with pressure and temperature (Wang and Nur, 1991; Wang et al., 1990). Daridon et al. (1998) conducted a series of ultrasonic measurements on a suite of hydrocarbons. Han and Batzle (2000) described a series of measurements on natural oils and provided a straightforward way to model the behavior. Oakley et al. (2003a,b) provided an extensive review of the literature of ultrasonic measurements in organic fluids in general and expressions for the speed of sound in 68 different pure organic fluids as a function of pressure.

Many workers have shown that the sound speeds in hydrocarbons are significantly affected by pressure and temperature. The experimental results of Daridon et al. (1998) on a light oil condensate, a medium weight hyperbaric oil, and a heavy natural hydrocarbon oil are shown in **Figure 13**. Generally, the denser the oil, the greater the wave speed. Wave speed also increases with pressure and decreases with temperature. However, it is important to note that these experiments were conducted at ultrasonic frequencies, and it is still not clear whether the values of K_f derived from them would reflect the adiabatic value at lower seismic frequencies; more work is required on this topic as very heavy oils have been shown to display a substantial dispersion both *in situ* (Schmitt, 1999) and in the laboratory (Behura et al., 2007).

Mixtures of CO_2 and H_2O are also of great importance for understanding chemical processes within the Earth. The growth of the geologic sequestration of greenhouse gases has further accelerated the need for knowledge of this system's behavior and its influence on the seismic properties of rocks

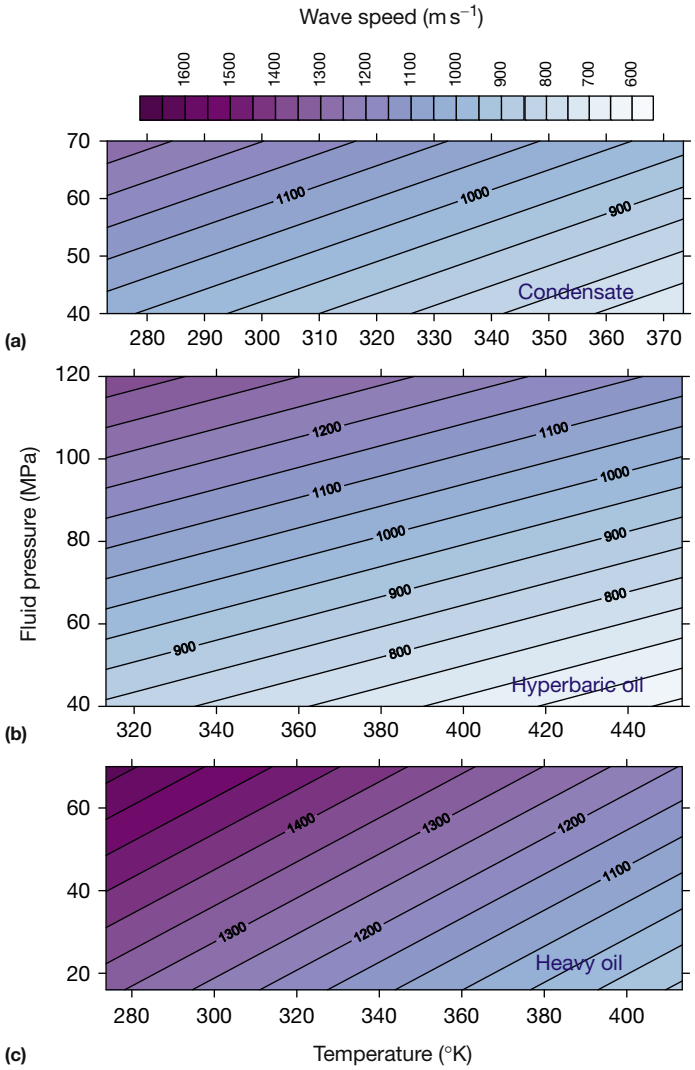

Figure 13 Sound wave speeds in (a) a light oil condensate, (b) a medium weight hyperbaric oil, and (c) a heavy undersaturated oil as measured by Daridon et al. (1998) with pressure and temperature.

in situ. Again, a large literature on the CO_2–H_2O system exists and Hou et al. (2013) gave an up-to-date listing of the many *PVTx* studies. The global phase diagram is described by a number of authors (Evelein et al., 1976; Spycher et al., 2003; Takenouchi and Kennedy, 1964; Wendland et al., 1999).

The limits on the solubility of CO_2 in H_2O complicate the phase diagrams (Duan and Sun, 2003) relative to those of the hydrocarbon mixtures as shown in **Figure 12** because, in addition to the vapor–liquid (VL) equilibrium curves, one must also consider the vapor–liquid–liquid (VLL) equilibrium where vapor coexists with H_2O-rich and CO_2-rich liquids. Some of this behavior is illustrated in **Figure 14**. Two compositionally dependent critical lines are evident although the one near the boiling line for pure CO_2 is small. The second critical line extends to higher pressures from the critical point of H_2O, but it does not continue to the critical point of CO_2 as was seen for the hydrocarbon mixtures in **Figure 12**. Instead, this curve bends backward to increasing temperatures with pressure, and it would be expected to eventually intersect the solid phase line at much higher pressures that are above the limits of current experiments (Evelein et al., 1976). This type of phase diagram is denoted class III (Gallagher et al., 1993; Gray et al., 2011; Vankonynenburg and Scott, 1980).

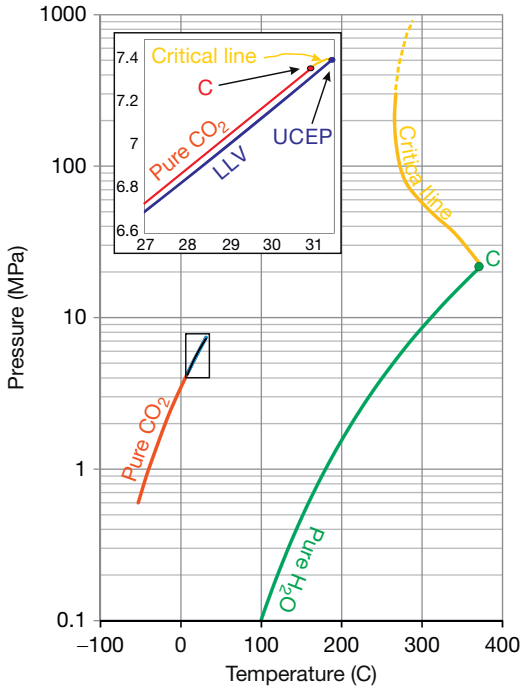

Figure 14 Some characteristics of the class III phase diagram of the CO_2–H_2O mixture system (Gray et al., 2011; Vankonynenburg and Scott, 1980) as projected onto the *P*–*T* plane. Inset is an expanded view of the area in *P*–*T* space near CO_2's critical point. Red and green lines are the boiling lines for single-component CO_2 and H_2O, respectively, and are the same as shown in **Figure 5(a)** and **5(b)**. These end at the respective critical points, also denoted as red or green C. Two composition-dependent critical lines exist. A short one connects CO_2's critical point to the upper critical end point (UCEP) at 7.411 MPa and 31.48 °C (Diamond and Akinfiev, 2003) for the liquid–liquid–vapor (LLV) three-phase line. This line is the locus of points where a H_2O-rich liquid, a CO_2-rich liquid, and a CO_2-rich vapor coexist with vapor existing to the right of this line. A second critical line extends to higher pressures from the critical point of water. Data for the LLV were determined by Wendland et al. (1999) while the second critical line is estimated from Takenouchi and Kennedy (1964). See also Gallagher et al. (1993).

Figure 14 highlights only the phase behavior of CO_2–H_2O mixtures. However, in order to calculate seismic properties, the density and bulk modulus of the mixture are required. Obtaining this information is challenging for such a complex system. Although a global model of the EOS for CO_2–H_2O mixtures has not yet been realized, workers have been able to provide EOS information over certain regions of *PVTx* space. For example, Duan and colleagues have developed models for the CO_2–H_2O gas phase from 0 to 28 MPa and from 323 to 645 °K (Duan et al., 2008) and vapor–liquid phase above 523 °K (Mao et al., 2009). Gallagher et al. (1993) provided estimates of behavior from 400 to 1000°K and to 100 MPa. However, a good deal of work still is required to fully understand this system (Hu et al., 2007). The use of such data in fluid substitution modeling of seismic responses may be further complicated by the fact that in practice, there will also be numerous additional impurities in the injected gas streams (Ziabakhsh-Ganji and Kooi, 2012).

11.03.5 The Rock Frame

11.03.5.1 Essential Characteristics

In order to properly understand the seismic properties of a real and usually fluid-saturated rock at depth in the Earth, one must also know the elasticity of the rock's skeleton or frame. The frame is an assemblage of a number of solid minerals. This construction, free of fluids or dry, will have its own elastic properties K_d and μ_d and density ρ_d. The subscript 'd' usually denotes the 'dry' or unsaturated state for the frame. This can also mean in certain contexts 'drained,' which is the state of a saturated sample after sufficient time such that the pore fluid pressure has equilibrated after a deformation. In the literature, the 'dry' and 'drained' conditions are usually taken to give the same static bulk modulus. The situation is different for wave propagation as fluids may not have time to move relative to the frame. In the earlier literature, the reader needs to take care when the term 'skeleton' is discussed as this has variously been used to describe either the mineral or the frame. The frame is characterized by its constituent minerals that will have their own solid moduli K_m and μ_m and density ρ_m, its porosity ϕ, and its permeability κ.

The fluid directly affects the overall density of the rock, ρ, through eqn [21] that is often simplified to

$$\rho = \phi\rho_f + (1-\phi)\rho_m \qquad [55]$$

where ϕ is the porosity (the ratio of the void space volume to the envelope or total volume of the material) and ρ_f and ρ_m are the fluid and the solid densities, respectively. When more than one fluid resides in the pore space, eqn [55] is further modified, particularly in the applied literature, to saturations S_j for each of the n immiscible free fluid components such that

$$\rho = \phi\left(\sum_{j=1}^{n} S_j\rho_j^f\right) + (1-\phi)\rho_m \qquad [56]$$

with

$$1 = \sum_{j=1}^{n} S_j \qquad [57]$$

and where ρ_f^f is the respective fluid component density. Usually, the saturations are assigned more directly to the different fluid phases such as S_w, S_o, and S_g for water, oil, and gas, respectively.

With these definitions out of the way, we proceed in this section to discuss the elastic properties of the rock frame. These frame properties are key to understanding the elasticity, and hence the wave propagation, through rocks. Again, there is a large literature on this topic as the study of wave propagation in porous fluid-saturated media is important in many disciplines.

11.03.5.2 The Pore-Free Solid Portion

In this section, we are interested in the effective elastic properties of the solid frame by itself. Rocks are most commonly a mixture of a number of minerals, and often, knowledge of the effective bulk K_m and shear μ_m moduli for the solid mineral portion is a first prerequisite to the more sophisticated calculations incorporating porosity and fluids. To obtain these, workers often assume that on average, the rock's minerals are randomly oriented such that the effective material is elastically isotropic. The simplest approaches to calculating the effective mineral moduli of the pore-free composite were derived by Voigt (1887) and by Reuss (1929a) who, respectively, assumed constant strain or stress within each of the components. Consequently, the Voigt and Reuss formulations are mixing rules for the stiffnesses or the compliances, respectively, such that for N isotropic components,

$$K_V = \sum_{i=1}^{N} \phi_i K_i \geq K_m \geq \left[\sum_{i=1}^{N} \phi_i / K_i\right]^{-1} = K_R \qquad [58]$$

and

$$\mu_V = \sum_{i=1}^{N} \phi_i \mu_i \geq \mu_m \geq \left[\sum_{i=1}^{N} \phi_i / \mu_i\right]^{-1} = \mu_R \qquad [59]$$

In eqns [58] and [59], the values of K_i and μ_i could be taken from **Table 2** or more extensive compilations (Bass, 1995).

Hill (1952) demonstrated that the Voigt and Reuss values bound the composite's effective bulk K_m and shear μ_m moduli. Various authors (see Watt et al. (1976)) have argued over which of the bounds or averages provide the best values. In practice, Hill's simple arithmetic mean of the bounds $K_{VRH} = [K_R + K_V]/2$ and $\mu_{VRH} = [\mu_R + \mu_V]/2$ is most usually calculated to give K_m and μ_m as done similarly in **Section 11.03.3.2** for isotropic composites of polycrystals made of a single mineral phase. The difference here is that the bounds are assumed to be mixtures of isotropic materials.

Hashin and Shtrikman's (1962) approach may also be applied to estimating the composite's elastic moduli according to

$$K_{HS}^{+} = K_1 + \frac{\phi_2}{(K_2 - K_1)^{-1} + \phi_1\left(K_1 + \frac{4}{3}\mu_1\right)^{-1}} \geq K_m$$

$$\geq K_2 + \frac{\phi_1}{(K_1 - K_2)^{-1} + \phi_2\left(K_2 + \frac{4}{3}\mu_2\right)^{-1}} = K_{HS}^{-} \qquad [60]$$

and

$$\mu_{HS}^{+} = \mu_1 + \frac{\phi_2}{(\mu_2 - \mu_1)^{-1} + \frac{2\phi_1(K_1 + 2\mu_1)}{5\mu_1\left(K_1 + \frac{4}{3}\mu_1\right)}} \geq \mu_m$$

$$\geq \mu_2 + \frac{\phi_1}{(\mu_1 - \mu_2)^{-1} + \frac{2\phi_2(K_2 + 2\mu_2)}{5\mu_2\left(K_2 + \frac{4}{3}\mu_2\right)}} = \mu_{HS}^{-} \qquad [61]$$

Equations [60] and [61] are valid for only two mineral components, but Hashin and Shtrikman (1963) also provided the methodology to carry out the calculations for N components (Berryman, 1995; Watt et al., 1976).

Calculations using eqns [58] through [61] are carried out for a hypothetical mixture of quartz and calcite for purposes of illustration in **Figure 15**. Such a quartz–calcite mixture is not expected to exist naturally, but these two minerals were chosen only because of the large differences in their elastic moduli and because of the unusual differences between K_m and μ_m. Equation [59] gives similar values of the shear moduli with the largest deviation between μ_V and μ_R being $< 3\%$ at $\phi_{quartz} = 0.5$. In contrast, the Voigt and Reuss bulk moduli from eqn [58] differ by nearly 11% at the same quartz proportion. In contrast, the Hashin–Shtrikman bounds for both moduli of eqns [60] and [61] differ by only a fraction of a percent. This translates into tighter differences for the wave speeds that vary by at most by 3.5% and 1.4% for V_P and V_S, respectively. Consequently, eqns [58] through [61] are widely used to estimate K_m and μ_m for the rock, and there appears to be good experimental evidence of their applicability to pore-free metal composites (Hashin and Shtrikman, 1963; Umekawa and Sherby, 1966) and to an assortment of rocks (Brace, 1965; Ji et al., 2002) subject to high pressures.

One caveat is that in many rocks, the minerals have a preferential crystallographic alignment due to sedimentary deposition or metamorphic deformation. In such cases, the minerals are no longer crystallographically randomly oriented; and their intrinsic anisotropy affects the overall anisotropy of the composite. These preferential mineral alignments are variously called lattice-preferred orientations (LPO) or crystallographic-preferred orientations (CPO) in the literature. This requires that the various mixing theories be modified to account for the crystal symmetries and the statistics of their orientations with respect to that of the material.

There is insufficient room to go into details of the procedures used and only a brief listing of the relevant literature is given. Different averaging techniques were described by a variety of workers (Babuska, 1972; Bunge, 1974; Crosson and Lin, 1971; Kumazawa, 1969; Thomsen, 1972). Mainprice (1990) provided computer programs that utilized these ideas and applied it to a textured plagioclase rock.

Noting that the results from the Voigt and Ruess averages are not invertible to each other (i.e., eqn [13] does not hold), Matthies and Humbert (1993) developed the geometric mean average that was then used by Mainprice and Humbert (1994) on polycrystals of feldspar and biotite and by Cholach and Schmitt (2006) to explore the effects of the strength of phyllosilicate orientations on the seismic anisotropy of shales and schists. The ability to quantitatively obtain mineralogical orientation distribution functions has grown greatly in the last

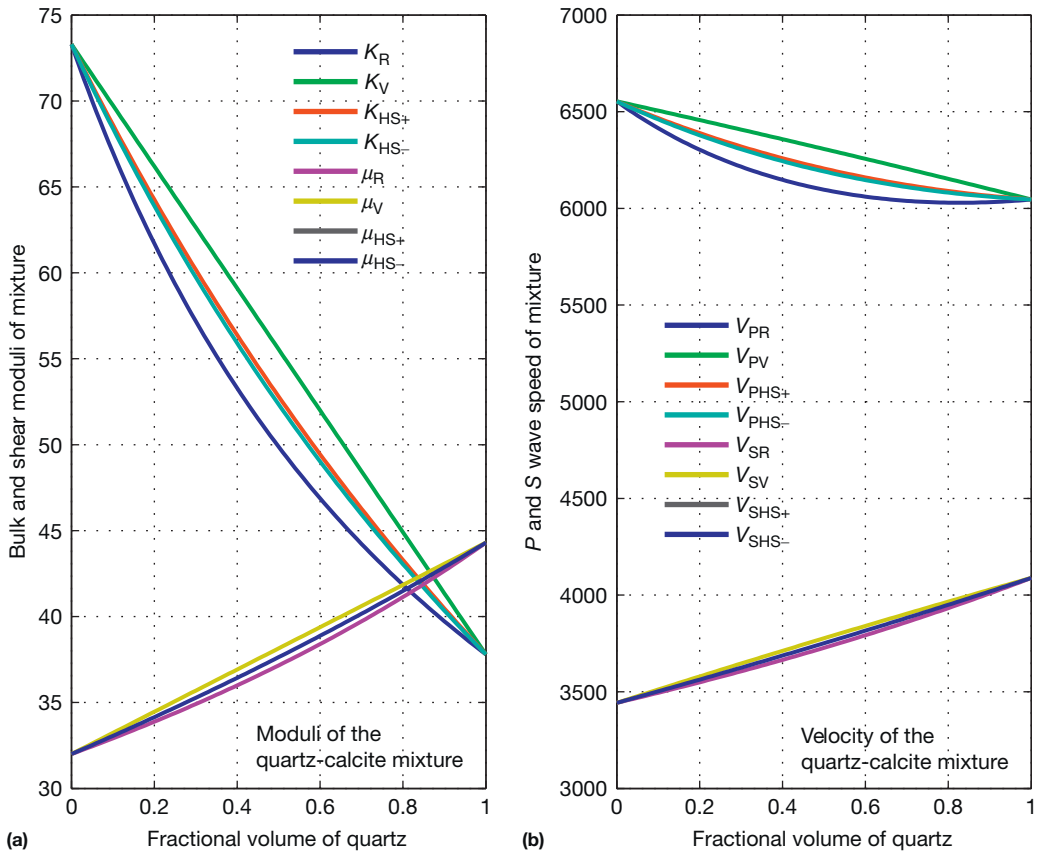

Figure 15 Illustration of the predictions of the (a) Voigt, Reuss, and Hashin–Shtrikman bounds and the resulting (b) V_P and V_S for a hypothetical mixture of calcite and quartz as a function of the volume fraction of quartz.

decade with developments in x-ray and neutron scattering and electron backscatter diffraction techniques. This is motivating a growth in the use of the averaging techniques that have now been applied to numerous different rock types (e.g., Almqvist et al., 2010; Kanitpanyacharoen et al., 2011; Wenk et al., 2007, 2012), although often the model results disagree with corresponding observations because the averaging models cannot account for porosity. Development of modeling procedures still continues (Man and Huang, 2011; Morris, 2006).

11.03.5.3 Influence of Porosity

The rock's porosity ϕ has a large influence on the elastic properties of a material. Walsh et al.'s (1965) classic experiments still remain of interest in this context. They constructed a series of glass 'foams' of differing porosities by heating packs of glass beads. They then measured the linear compressibility of these samples with strain gauges during hydrostatic compression; unfortunately, this only provides a measure of the K_d as indicated by the filled squares in **Figure 16(a)**. Regardless, these data illustrate the rapid decline in K_d with ϕ.

It is worthwhile to compare these observations to the Voigt, Ruess, and Hashin–Shtrikman bounds described above, the expressions developed for a solid composed of a 'mineral' filled with spherical pores by MacKenzie (Li and Zhang, 2011; Mackenzie, 1950; Yoshimura et al., 2007) and those of Kuster and Toksöz (1974a,b).

Mackenzie's expressions take the form

$$K_{MK} = \frac{K_m}{\left[1 + \frac{3\phi(1-\nu_m)}{2(1-2\nu_m)(1-\phi)}\right]} \quad [62]$$

and

$$\mu_{MK} = \frac{\mu_m(1-\phi)}{\left[1 + \frac{\phi(12+6K_m/\mu_m)}{(8+9K_m/\mu_m)}\right]} \quad [63]$$

Poisson's ratio for the solid portion ν_m may be calculated from the pore-free mineral moduli K_m and μ_m using a standard elastic relation (Birch, 1961)

$$\nu_m = \frac{1}{2}\frac{3K_m - 2\mu_m}{3K_m + \mu_m} \quad [64]$$

The corresponding formulas for spherical inclusions with moduli K_i and μ_i and volume fraction, ϕ, according to Kuster and Toksöz (1974a) are

$$(K_{KT} - K_m)\frac{(K_m + 4\mu_m/3)}{(K_{KT} + 4\mu_m/3)} = \phi_i(K_i - K_m)\frac{(K_m + 4\mu_m/3)}{(K_i + 4\mu_m/3)} \quad [65]$$

and

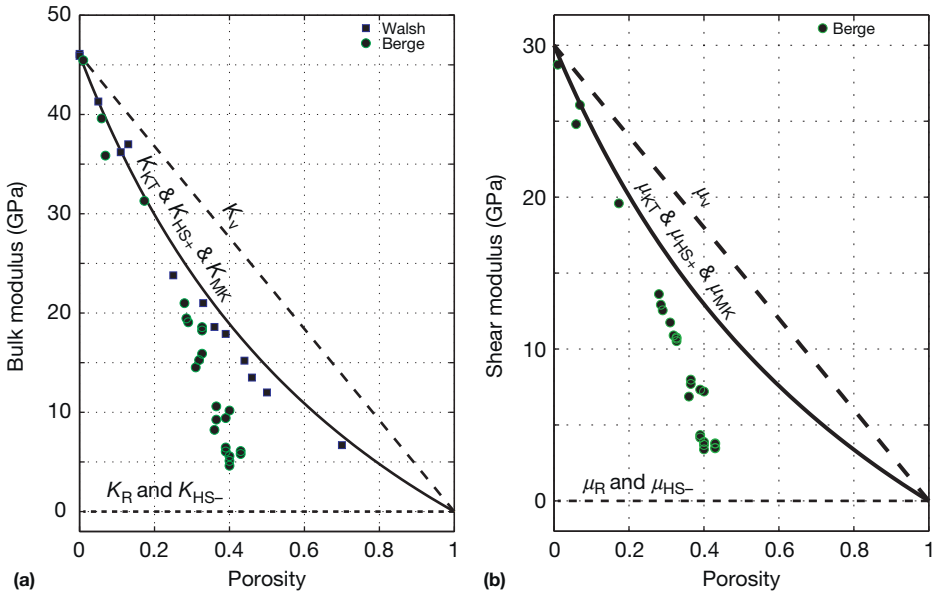

Figure 16 Comparison of experimentally observed (a) bulk modulus and (b) shear modulus versus air-filled porosity in sintered porous glass composites from Walsh (1965) and Berge et al. (1995). Subscripts on the moduli are R, Ruess bound; V, Voigt bound; HS− and HS+, Hashin–Shtrikman bounds; KT, Kuster–Toksöz; and MK, Mackenzie.

$$\left(\mu^{KT}-\mu_m\right)\frac{(\mu_m+\zeta_m)}{(\mu^{KT}+\zeta_m)}=\phi_i(\mu_i-\mu_m)\frac{(\mu_m+\zeta_m)}{(\mu_i+\zeta_m)} \qquad [66]$$

where

$$\zeta_m=\frac{\mu_m(9K_m+8\mu_m)}{6(K_m+2\mu_m)} \qquad [67]$$

The moduli for the inclusions are taken to be zero for the calculations shown in **Figure 16**. For this particular case (and also for cases in which the spherical voids are filled with a fluid for which $\mu_i=0$), the Reuss and the lower Hashin–Shtrikman bounds coincide. Further, the Kuster–Toksöz and the upper Hashin–Shtrikman bound values also are the same, and these are also close to those calculated using Mackenzie's equations.

One important observation from **Figure 16** is that unlike the calculations for a nonporous mixture of solids (**Figure 15**), the Voigt–Reuss bounds are less useful in predicting the moduli for porous materials. One reason for this is the large divergence between the vanishing moduli in the empty pore. The Hashin–Shtrikman bounds, too, have a wide variance although the upper bounds appear to match Walsh et al.'s (1965) bulk modulus observations reasonably well.

There is some scatter in Walsh et al.'s (1965) experimental results in **Figure 16(a)**, but they do trend close to but slightly lower than the $K_{KT}-K_{HS+}-K_{MK}$ prediction line. The reason for this most likely lies in the fact that both the Kuster–Toksöz and Mackenzie formulations assume 'dilute' amounts of spherical voids that are sufficiently removed from one another such that the interactions between their concentrated stress and strains may be ignored. Interaction of the elastic fields from individual spheres cannot be avoided once the spheres become sufficiently proximate.

Numerous authors have attempted to overcome these limitations by addressing such interactions by two main groups of approaches: that of an effective matrix or that of an effective field (Carvalho and Labuz, 1996; Mavko et al., 2003). The effective matrix approaches are often further subdivided either into 'self-consistent' methods (Budiansky and O'Connell, 1976; Hill, 1965; Wu, 1966) that consider the solids and pores as a whole or by 'differential effective medium' methods in which pores are incrementally added to a matrix in order to update its modulus, and this revised modulus is then that of the new matrix for the next iteration (e.g., Berryman et al., 2002; David and Zimmerman, 2011; Kachanov, 1980; Li and Zhang, 2011; Norris, 1985; Zimmerman, 1984). The effective field methods developed by Mori and Tanaka (1973) place a pore in the nonporous solid to which a stress field is then applied. The advantage of this approach is that more complex stress fields can be applied within the material accounting directly for the existence of the holes. These techniques have been widely applied in the composite materials literature but have not seen as much application in rock physics (Sayers and Kachanov, 1995), although Kachanov et al. (1994) suggested that the Mori–Tanaka approach may be superior. Berryman and Berge (1996) noted the exclusivity of the use of the Mori–Tanaka approach in the engineering literature and contrasted it with the Kuster–Toksöz model employed in geophysics indicating that both are likely only valid for $\phi<0.3$. Yan et al. (2011) gave a recent example of the use of the Mori–Tanaka approach in estimating the frame moduli of sandstones.

The literature on modeling of rock properties using the various developments presented earlier in the text is large and only a small view of it is possible here. Mavko et al. (2003) provided some starting points for further investigations.

The porosity-dependent variations in moduli transfer through to the wave speeds according to eqns [1] and [2]. An illustration of this effect in a suite of carbonates, primarily clean limestones, shows the significant changes in both V_P and V_S with increasing porosity. Both wave speeds decrease

by upward of 50% over the range of ϕ measured. This is despite the fact that the bulk density, ρ, which is in the denominator of eqns [1] and [2], also decreases as ϕ increases according to eqn [55]. Cleary, porosity is an important factor in determining a material's seismic wave speeds.

11.03.5.4 Influence of Crack-Like Porosity

As just noted, aside from the constituent mineralogy, the most important factor affecting the elastic properties of the frame is ϕ. The calculations shown in **Figure 16** are based on spherical pores, but most pores will not be shaped so simply; and the geometry of the pores needs also to be considered. It is useful to return to **Figures 16** and **17** to see some of such effects. Berge et al. (1995) measured V_P and V_S on sandstone analogs of lightly sintered glass beads and, from these values, calculated the dynamic moduli shown in **Figure 16**. Their observed values substantially deviate from those obtained in Walsh et al.'s (1965) measurements and from those predicted by Mackenzie's (1950) derivation of eqn [62]. Bakhorji's (2009) measurements on carbonates, too, show considerable scatter of up to 1700 m s^{-1} for limestones near a given ϕ. Other factors that simplify porosity and mineralogy must be influencing these observations.

Much of this can be explained by considering the influence of the pore shape. At the risk of oversimplifying the problem, pore shapes can broadly be placed into two categories: equant or crack-like. Much like a Roman arch, large aspect ratio equant pores are stiff; they do not significantly deform under the application of a stress. In contrast, small aspect ratio crack-like pores are easily compressed and can close under even modest stresses.

An important consequence of this is that the rock elastic moduli are generally pressure-dependent, a fact that has been known since the very first elastic measurements on rock to high pressures by Adams and Williamson (1923) (**Figure 18(a)**). They were surprised that such effects were seen in rocks with porosities $<1\%$. They theoretically tested a number of possible

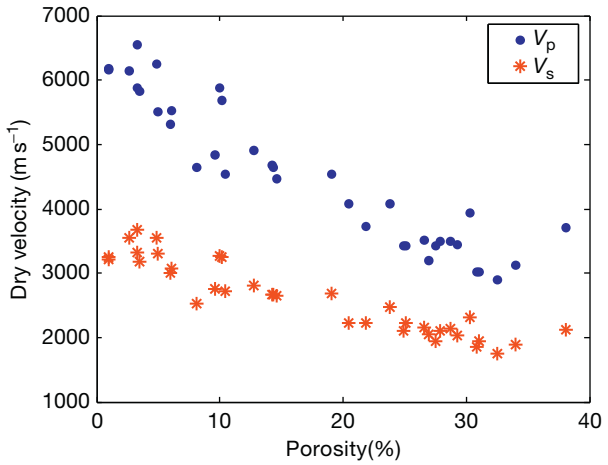

Figure 17 Illustration of the effects of porosity on V_P (blue filled circles) and V_S (red stars) for a suite of carbonates from the Arab D formation of Saudi Arabia. Experimental errors are approximately the size of the symbols. Unpublished ultrasonic measurements from Bakhorji (2009).

hypotheses and finally inferred that this nonlinear behavior must be due to the existence of crack-like pores of small aspect ratio.

Heuristically, this behavior stems from the large compressibility of a crack-like pore perpendicular to its plane. A normal stress applied across the crack face pushes the surfaces towards one another. As this stress increases, the effective crack shortens and eventually closes at pressure P_c. For a crack with an elliptical cross-section of aspect ratio χ (ratio of the minor to major axes), this is (Walsh, 1965)

$$P_c = \frac{\pi E_m \chi}{4\left(1-\nu_m^2\right)} \qquad [68]$$

where E_m and ν_m are the solid mineral Young's modulus and Poisson's ratio, respectively. Cracks with small aspect ratios χ are easily closed. For example, a hypothetical elliptical crack with $\chi \sim 10^{-3}$ residing in quartz matrix closes by application of <2 atmospheres of pressure ($\sim$0.2 MPa). In contrast, a spherical 'crack' with $\chi = 1$ would according to eqn [68] not close until 172 GPa. Of course, the material would crush long before such a pressure could be reached, but these calculations serve to illustrate how easily crack-like porosity can be closed relative to more equant porosity.

Consider subjecting a material containing cracks with a distribution of different χ's to an increasing confining pressure. At low pressures, those cracks with small χ first close. As the pressure continues to increase, cracks with progressively larger χ will close. Once closed, a crack no longer influences the overall elasticity and essentially disappears with the result that the rock becomes less compressible. This is illustrated in **Figure 18(b)**, which is a cartoon of the expected strains on a cracked rock sample. As pressure increases, the observed strain (heavy dark line) is initially nonlinear. As the cracks progressively close, the material stiffens and the strain–stress curve becomes less steep. This continues until all of the crack porosity is closed at which point the strain–stress curve becomes linear and parallel to that expected for the pore-free solid (thick dashed line). The observed strain is a combination of the strains due to closure of the cracks (thick dashed line) and that of the solid. This can be seen in the real strains observed on a dolomite rock sample (**Figure 18(c)**). These arguments are perhaps a bit oversimplified (Stroisz and Fjaer, 2013), but regardless at lower confining stresses, rocks are generally nonlinearly elastic materials, that is, their moduli and subsequently their seismic wave speeds depend on confining pressure. One may be able to ignore this in the deep crust and the Earth's mantle, but it appears to be an important factor in seismic investigations nearer the Earth's surface (Crampin and Peacock, 2008; Schijns et al., 2012). Recognizing this fact is key, for example, in properly interpreting time-lapse seismic observations from reservoirs subject to varying states of effective stress.

As noted, such nonlinear pressure dependencies have been noted since Adams and Williamson (1923). This pressure dependence of the elastic moduli translates into a pressure dependence of the waves speeds. Such effects have been observed in nearly all rock types and an incomplete listing of contributions where such nonlinear effects have been observed includes those for igneous and metamorphic hard rocks (e.g., Birch, 1960, 1961; Blake et al., 2013; Cheng and Toksöz, 1979; Cholach et al., 2005; Christensen

and Stanley, 2003; Goddard, 1990; Kern, 1982; Lyakhovsky et al., 1997; Todd and Simmons, 1972), sandstones (e.g., Christensen and Wang, 1985; Gomez et al., 2010; Jones and Nur, 1983; Khazanehdari and McCann, 2005; Khazanehdari and Sothcott, 2003; Lo et al., 1986; Prasad and Manghnani, 1997; Sayers, 2002; Sayers et al., 1990; Smith et al., 2010; Wyllie et al., 1958; Xu et al., 2006), carbonates (e.g., Alam et al., 2012; Azeemuddin et al., 2001; Fabricius et al., 2008; Melendez Martinez and Schmitt, 2013), and mudstones (Freund, 1992; Kwon et al., 2001; Sayers, 1999). For example, the wave speeds in a highly cracked sandstone (**Figure 19(b)**) from the Cadotte formation in Alberta vary greatly even over the relatively modest range of confining pressures to 60 MPa (He, 2006). It is interesting to contrast this rock's behavior with that for a comparison brass sample that over this pressure range has a wave speed that increases slightly due to the pressure-dependent increase in the intrinsic crystal moduli as described in the section on minerals in the preceding text.

Many workers have focused on different ways to describe this nonlinearity including the use of curve fitting (Carcione and Tinivella, 2001; Eberhart-Phillips et al., 1989; Freund, 1992; Khaksar et al., 1999; Kirstetter et al., 2006; Prasad and Manghnani, 1997; Prikryl et al., 2005; Zimmerman, 1985), Birch–Murnaghan equations of state (Birch, 1961), differential

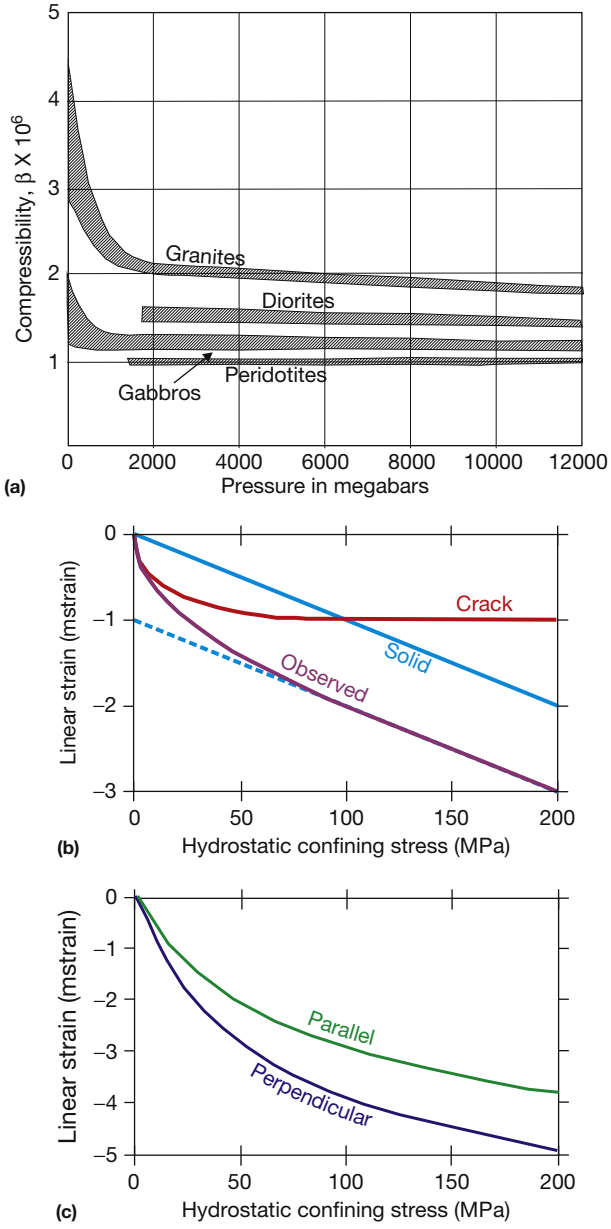

Figure 18 Effect of cracks on the elastic properties of rocks. (a) Early observations of compressibility of a series of rocks, as shown in the redrafting of Figure 7 of Adams and Williamson (1923). The gray areas represent the spread of the moduli they expected due to mineralogical differences within a given geologically defined rock type. Note that their definition of a megabar = 1.0197 kg cm^{-2} = 0.9869 atm ~ 0.1 MPa and should not be confused with the modern Mbar = 100 GPa. (b) Illustration of the partitioning of the total observed strain into components due to the cracks and the minerals as a function of pressure (redrafted from Schmitt and Li, 1995). (c) Observed strains parallel and perpendicular to the sedimentary layering in a cracked dolomite as a function of hydrostatic confining pressure. (data from Schmitt and Li, 1995).

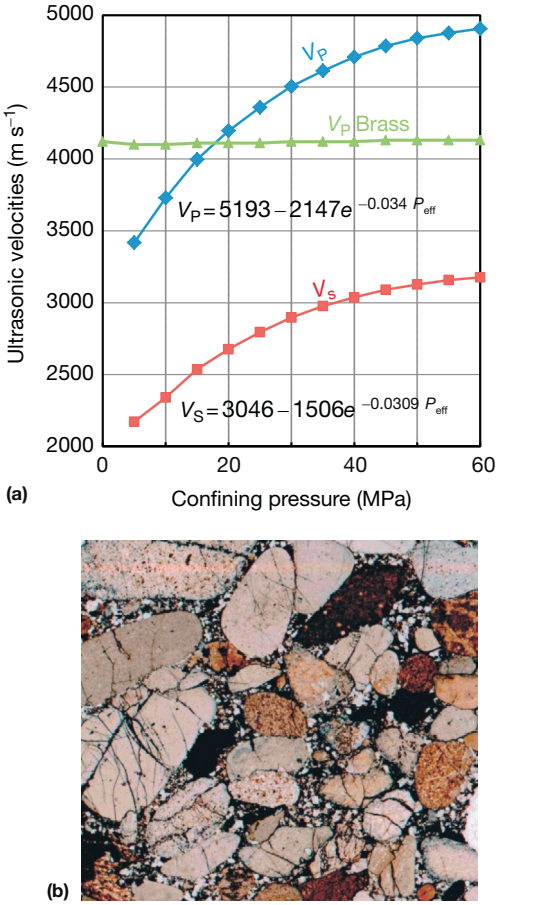

Figure 19 Example of the effects of pressure on wave speeds in a cracked rock. (a) Ultrasonically determined V_P (blue diamonds) and V_S (red squares) as a function of hydrostatic confining pressure. V_P for nonporous brass (green triangles) is shown for comparison. The fits to eqn [70] are shown. (b) Photomicrograph (2 × 2 cm) under transmitted light of the Cadotte sandstone showing its highly cracked nature. Despite differences in the color of the pebbles, they are nearly pure microcrystalline quartz. Unpublished data (for sample SB009 from 2457.7 m depth) and image from He (2006).

approaches (Ciz and Shapiro, 2009), crack damage (Lyakhovsky et al., 1997), and third-order elastic moduli (Payan et al., 2009; Sayers and Kachanov, 1995; Sinha and Kostek, 1996). In describing the pressure dependence of a velocity in such rocks, often workers will use an empirical expression of the form

$$V_i = A + CP_{\text{eff}} - Be^{-DP_{\text{eff}}} \quad [69]$$

where V_i can be either V_P or V_S, P_{eff} is the effective pressure (to be described shortly) applied to the material, and A, B, C, and D are simply parametric fitting parameters. C is often left as zero as it can result in unreasonable values at elevated pressures (Khaksar et al., 1999). This is convenient when the only information available might be laboratory measurements on the core samples. While eqn [69] is essentially devoid of any physics, it does well describe the shapes of the curves shown in **Figure 19** differing from the observed values by <15 m s^{-1} (He, 2006).

A number of approaches have been employed to more fundamentally explain the effects of cracks on elastic moduli and velocities. The already mentioned self-consistent approach (Budiansky and O'Connell, 1976; O'Connell and Budiansky, 1974) remains popular because of its relative ease of application. Consider the case of flat circular cracks of radius a and with an elliptical cross-section of minor axis c and with $a \gg c$. The crack density parameter is $\epsilon \equiv N\langle a^3 \rangle$ where N is the number of cracks per unit volume. It can only be related to the crack porosity ϕ_c if one assigns values to a and c so that $v_c = 4\pi a^2 c/3$ if all the cracks have the same dimensions whereupon $\phi_c = Nv_c$. Once ϵ is set, the effective Poisson's ratio of the cracked solid v_d must first be found from

$$\epsilon = \frac{45}{16}\frac{(v_m - v_d)(2 - v_d)}{(1 - v_d^2)(10v_m - 3v_m v_d - v_d)} \quad [70]$$

whereupon the moduli

$$K_d = K_m\left[1 - \frac{16}{9}\left(\frac{1 - v_d^2}{1 - 2v_d}\right)\epsilon\right] \quad [71]$$

and

$$\mu_d = \mu_m\left[1 - \frac{32}{45}\frac{(1 - v_d)(5 - v_d)}{(2 - v_d)}\epsilon\right] \quad [72]$$

are easily calculated. For purposes of illustration, this self-consistent approach is applied by placing cracks with major axis diameter of $a = 1$ mm for three different and small aspect ratios $\alpha = c/a$ in **Figure 20**. We choose to plot the moduli and wave speeds as function of the crack porosity ϕ_c because the physical meaning of the crack density parameter ϵ is less intuitive. Examination of **Figure 20** shows that smaller aspect ratio cracks have a disproportionate influence on the overall elastic moduli and velocities. Further, even a vanishingly small crack porosity of $<1\%$ has a substantially larger effect than the equivalent more equant porosity. This is particularly apparent when the theoretical results for spherical pores of **Figure 16** are compared to the equivalent crack porosities in **Figure 20**.

While we have used here the O'Connell and Budiansky (1974) self-consistent forms to illustrate the large influence of crack-like porosity on rock properties, it must be noted that there are also many competing models. Again, geophysicists

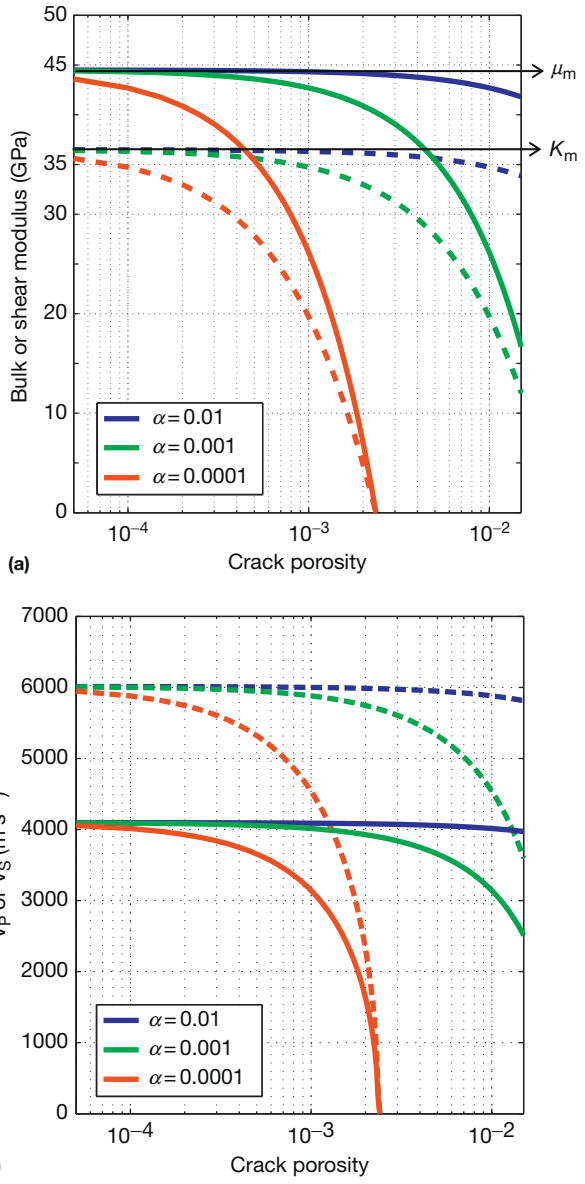

Figure 20 Illustration of the influence of crack porosity for elliptical pores with $a = 1$ mm and with aspect ratios $c/a = 0.01$ (blue lines), 0.001 (green lines), and 0.0001 (red lines) in a quartz solid on (a) the elastic moduli K_d (solid lines) and μ_d (dashed lines) and (b) the wave speeds V_P (dashed lines) and V_S (solid lines) according to self-consistent models.

will often employ the Kuster and Toksöz (1974a) model adjusted to employ small α ellipsoids. Horii and Nemat-Nasser (1983) extended the self-consistent approach by including crack–crack interactions, crack closure, and frictional sliding along the planes of closed cracks to show that the loading history may be important. Berryman et al. (2002) developed a differential effective medium model to account for dry and fluid-filled cracks. Hudson (1981) used a mean field approach to account for the dynamic effects of both aligned and randomly oriented cracks, and an advantage of his formulation is that he can account for seismic attenuation. Mavko and Nur (1978) carried out an analysis that employed dislocation theory to solve for the deformations associated with a more realistic

crack geometry with tapered edges. More recently, Gao and Gibson (2012) developed a statistical asperity model to describe the influence of microcracks and provide a more extensive review of the recent literature than is possible here.

Numerous authors have attempted to use the shapes of either the strain curves (as in Figure 18) or wave speeds (as in Figure 19) to invert for various characteristics of the cracks and the distributions of their dimensions (e.g., Angus et al., 2009; Cheng and Toksöz, 1979; David and Zimmerman, 2012; Schubnel et al., 2006) under a variety of simplifying assumptions.

11.03.5.5 Pressure Dependence in Granular Materials

Cracked Earth materials are not the only ones with pressure-dependent frame properties. Granular materials, such as unconsolidated sands at low confining pressures, too, are also highly sensitive to applied confining pressures. This has been demonstrated by many workers in the laboratory (Bachrach and Avseth, 2008; Domenico, 1977; Goddard, 1990; Makse et al., 1999; Zimmer, 2003; Zimmer et al., 2007) or inferred from field measurements (Bachrach et al., 2000). In order to predict the moduli and wave speeds in such materials, theoretical developments (Digby, 1981; Walton, 1987) rely primarily on the 'Hertz–Mindlin' deformations (Johnson, 1987) at the contact between two mineral grains. Consider a grain pack with porosity ϕ within which each grain will on average touch R neighbors. Further, assume that both normal and shear tractions exist at each grain contact according to Walton's (1987) 'infinitely rough' grain model. The moduli of this grain pack as rewritten by Makse et al. (1999) are

$$K_d = \frac{C_n(\phi R)^{2/3}}{12\pi}\sqrt[3]{\frac{6\pi P}{C_n}} \quad [73]$$

and

$$\mu_d = \frac{(C_n + 3C_t/2)(\phi R)^{2/3}}{20\pi}\sqrt[3]{\frac{6\pi P}{C_n}} \quad [74]$$

where

$$C_n = \frac{4\mu_m}{1-\nu_m} \quad [75]$$

and

$$C_t = \frac{8\mu_m}{2-\nu_m} \quad [76]$$

are factors that relate the forces at the contact points to the induced overlap between the grains. Walton also derived expressions for the case of 'smooth' spheres where any tangential forces at the grain contacts disappear. Makse et al. (1999) gained insight from discrete particle modeling (Cundall and Strack, 1979) to infer that the coordination number R is also pressure-dependent because of grain motions with a value empirically derived from their numerical modeling of

$$\langle R\rangle = 6 + \left(\frac{P}{0.06}\right)^{1/3} \quad [77]$$

where in this expression, the confining pressure P must be in units of MPa. The cubic root dependence of the moduli with confining pressure in eqns [73] and [74] is perhaps the most interesting aspect of these equations. This is essentially due to the fact that the grain contacts become stiffer with pressure as their contact area expands. The moduli increase more rapidly in Makse et al.'s (1999) model because the number of grain contacts is also increasing with pressure. This cubic root for the moduli translates to a 1/6 root dependence for the wave speeds.

Although the theory illustrated in Figure 21 captures some of the elements of the pressure dependence of the moduli, real measurements on granular materials give different moduli and

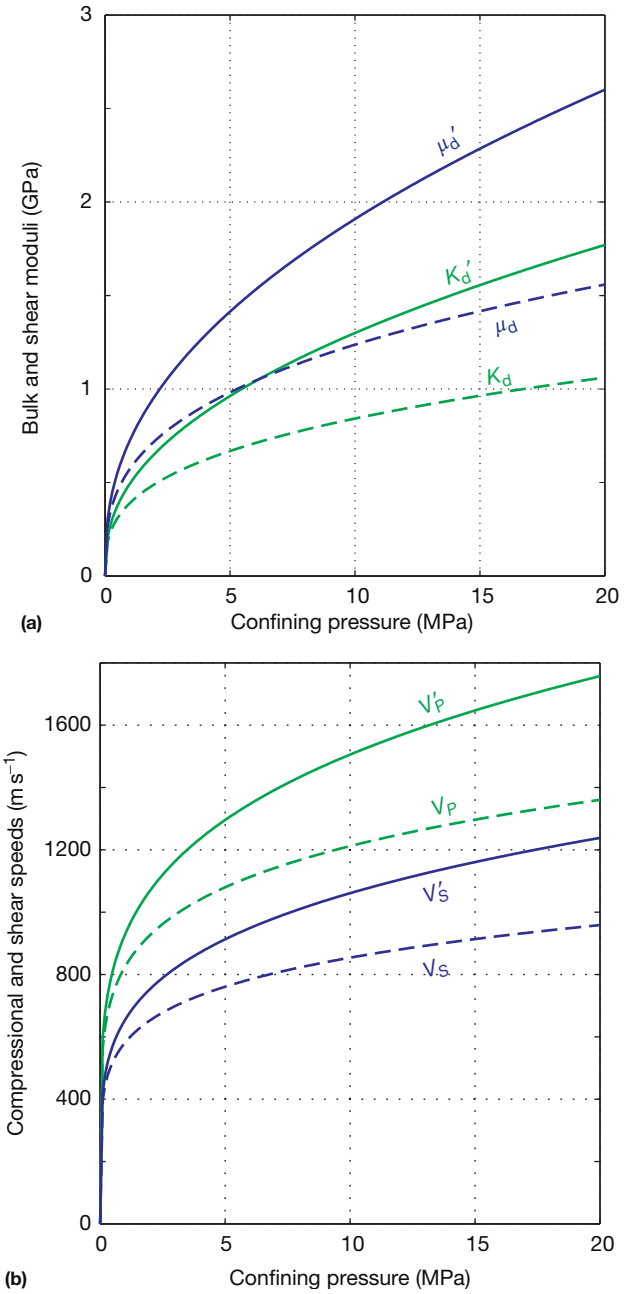

Figure 21 Illustration of the confining pressure dependence of (a) the dry frame moduli K_d (eqn [74], dashed green line) and μ_d (eqn [75], dashed blue line) according to Walton (1987) and (b) the corresponding compressional V_P (dashed green line) and shear V_S (dashed blue line) wave speeds of an unconsolidated pack of quartz spheres ($K_m = 36.5$ GPa, $\mu_m = 44.5$ GPa, $\rho_m = 2650$ kg m^{-3}) with a porosity $\phi = 0.36$ and coordination number $R = 6$. The corresponding values that include the pressure dependence of R (eqn [78]) are shown as solid lines and denoted by $'$.

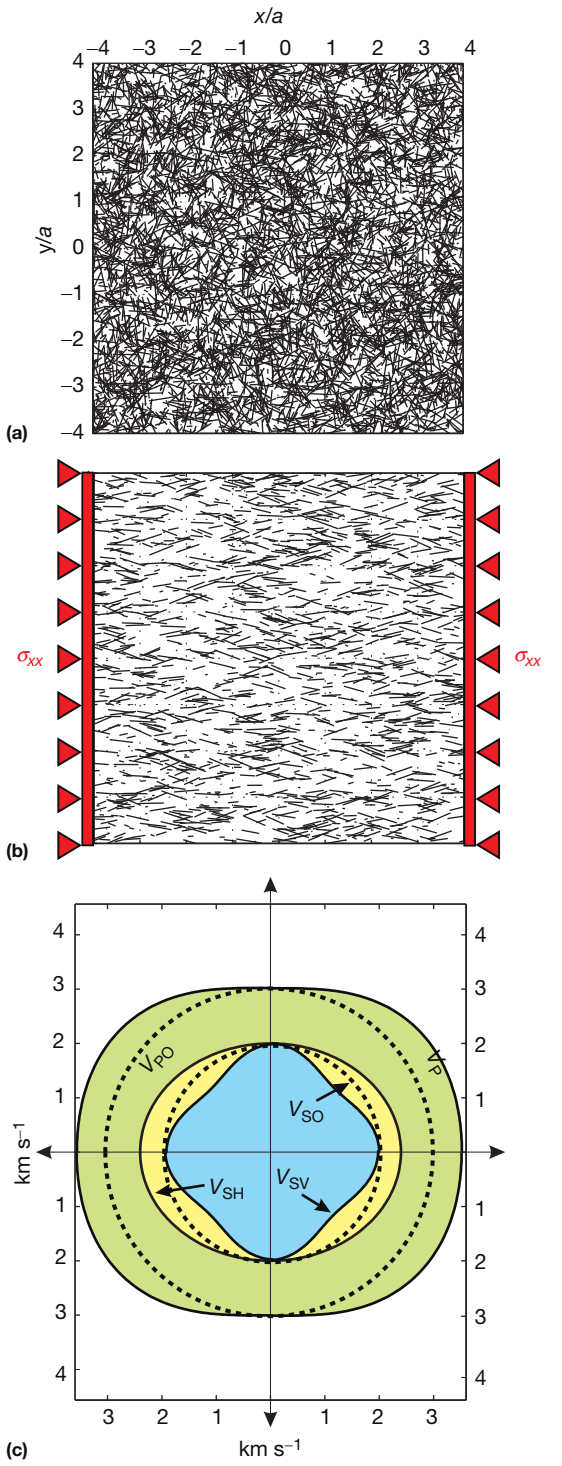

Figure 22 Two-dimensional description of crack-induced elastic anisotropy. (a) Initial cracked medium with random orientation of cracks. (b) Distribution of remaining open cracks after application of horizontal compression stress σ_{xx} (modified from Schmitt DR, Currie CA, and Zhang L (2012) Crustal stress determination from boreholes and rock cores: Fundamental principles. *Tectonophysics* 580: 1–26). (c) Hypothetical wave velocity surfaces before (circles outlined with dashed lines) and after (solid lines) application of σ_{xx}. V_{PO} and V_{SO} are the original isotropic compressional and shear wave speeds material of (a). V_P, V_{SV}, and V_{SH} are the induced anisotropic wave surfaces for the compressional, the vertically polarized shear (i.e., in the plane of the figure), and the horizontally polarized shear (i.e., perpendicular to the plane of the figure) wave modes, respectively. In (c), the wave speed is represented by the distance from the origin.

velocities (Hardin and Blandford, 1989). On the basis of an extensive series of ultrasonic wave speed measurements on a wide variety of different packs of synthetic and natural grains, (Zimmer, 2003; Zimmer et al., 2007) found exponents that were significantly $<1/6$. Recently, Andersen and Johansen (2010) found that Walton's (1987) model overpredicts the observed sonic log wave speeds in unconsolidated sands by more than a factor of 1.5, and they suggested empirically derived curves (e.g., Fam and Santamarina, 1997) may be best.

11.03.5.6 Implications of Pressure Dependence

The pressure sensitivity of moduli and wave speeds has two important implications. The first is that the application of nonhydrostatic or deviatoric stress states affects the rock's elastic anisotropy. The second is that the properties are also highly sensitive to a pore pressure. Both of these factors can strongly affect the seismic observations.

11.03.5.6.1 Stress-induced anisotropy (acoustoelastic effect)

All of the discussions to this point have assumed that the materials are subject to a uniform hydrostatic confining pressure P. In the Earth, however, a deviatoric state of stress is the general case. Such states of stress produce wave speed anisotropy in both granular (Sayers, 2002, 2007; Walton, 1987) and cracked (Horii and Nemat-Nasser, 1983; Sayers and Kachanov, 1995) rocks. In the former, the anisotropy results from the stiffening of the contacts in the direction parallel to the greater compression. In the latter, the anisotropy is primarily a consequence of the preferred closure of those cracks whose plane is aligned normal to the greatest principle compression. Nur and Simmons (1969) may have been the first to observe these phenomena although the stress concentrations in their circular sample subject to a uniaxial force were not uniform. Since then the effect has been documented by many workers under more controlled stress state conditions (e.g., Babuska and Pros, 1984; Becker et al., 2007; Bonner, 1974; Gurevich et al., 2011; Johnson and Rasolofosaon, 1996; Stanek et al., 2013) in cracked rock, (Nur, 1971) in granular rock (e.g., Dillen et al., 1999; Khidas and Jia, 2010; Prioul et al., 2004; Rai and Hanson, 1988; Roesler, 1979) and numerically (Gallop, 2013; Hu et al., 2010). At the field scale, Schijns et al. (2012) were able to explain the observed seismic anisotropy in a 1300 m thick section of the Outokumpu biotite gneiss on the basis of oriented microcracks and mineral CPO (Elbra et al., 2011; Kern et al., 2009; Lassila et al., 2010; Wenk et al., 2012).

The basis of this effect again derives from the progressive closure of the crack-like porosity with compression. Consider an unstressed rock mass containing numerous narrow cracks, the orientations of which are randomly but uniformly distributed (**Figure 22(a)**). Application of an appropriately large uniaxial stress σ_{xx} to the mass closes those cracks whose planes are perpendicular or nearly so to the direction of σ_{xx} (Berg, 1965; Walsh, 1965) while leaving the cracks whose planes are

aligned to the stress open as shown in Figure 22(b). This transforms the initially isotropic rock into a transversely isotropic one (Fuck and Tsvankin, 2009) with directionally dependent relative wave speeds as shown in Figure 22(c).

Stress-induced anisotropy is important in many geophysical problems from complicated stress conditions near a wellbore (Schmitt et al., 1989; Winkler, 1996), in mines (Holmes et al., 2000a; Holmes et al., 2000b), over petroleum reservoirs (Wuestefeld et al., 2011), and in stress changes related to seismicity. (Crampin, 1994; Crampin and Peacock, 2008) in particular had championed the interpretation of shear wave splitting to infer stress states for reservoir monitoring and earthquake forecasting.

11.03.5.6.2 Influence of pore pressure

Although we are not yet considering the effects on the dynamic seismic properties of fluids in the pore space of the rocks, the fluid pore pressure P_p has an important effect on the static elastic properties of the frame that must be taken account of in most cases. Numerous laboratory experiments have shown that the frame properties of rocks depend not on the confining pressure P per se but on the effective pressure P_e:

$$P_e = P - \xi P_p \qquad [78]$$

where ξ the pore pressure coefficient. More generally, for a set of total or confining stresses σ_{ij}, the effective stresses σ_{eij} eqn [78] can be written as

$$\sigma_{eij} = \sigma_{ij} - \delta_{ij}\xi P_p \qquad [79]$$

where δ_{ij} is the Kronecker delta; the pore fluid does not influence the shear stresses.

What this means is that the frame moduli K_d and μ_d and consequently the wave speeds V_P and V_S are generally functions of P_e. A corollary to this is that the dry moduli do not change (to the first approximation) if P_e remains constant. The measurements of He (2006) on the Cadotte sandstone illustrate these effects well (Figure 23). In his tests, he first measured V_P and V_S through a water-saturated sample of the Cadotte sandstone at confining pressures to 60 MPa while maintaining the pore pressure $P_p = 0$. This yields the highly nonlinear curve of velocities versus confining pressure as was already encountered for a similar dry sample in Figure 19. Once this was accomplished, He repeated the measurements in suites where the differential pressure was held constant first at 15 MPa and then at 30 MPa. In both of these, the wave speeds remain constant, meaning that $\xi = 1$ over this pressure range to within experimental error.

The concept of effective pressure can be confusing in part because a worker must take care to consider which definition of effective pressure one truly requires for the phenomena at hand. More directly, this usually means one must have the appropriate value of ξ for the physical process being studied (Berryman, 1992; Berryman, 1993). The effective pressure/stress concept was first developed by Terzaghi with $\xi = 1$. However, the *apparent* ξ will deviate from unity depending on the rock structure and potential of chemical interaction (e.g., swelling clays) (Bernabe, 1987; Zoback and Byerlee, 1975), on the rates at which pore pressures can recharge during rapid deformation and dilatancy leading to failure (Brace and Martin, 1968; Schmitt and Zoback, 1992), and on the linear strains and volumetric deformation of the material itself (Biot and Willis, 1957; Nur and Byerlee, 1971). With regard to the last item, the Biot–Willis effective stress coefficient *for poroelastic strain* is

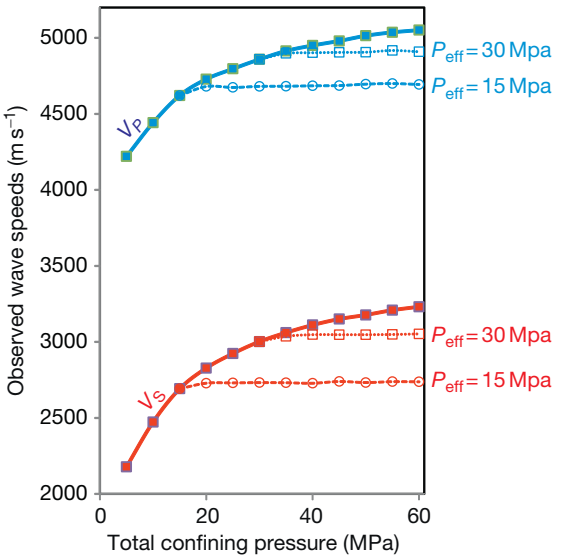

Figure 23 Observed ultrasonic velocities in a water-saturated sample of the Cadotte sandstone (see Figure 19) versus the total confining pressure. The solid lines are the velocities for V_P (blue) and V_S (red) for the sample with a small and constant pore pressure. Dashed and dotted lines and open circles and squares indicate the observations when the differential pressure $P - P_P$ is held constant at either 15 or 30 MPa, respectively. Data for sample SB007 of He (2006).

$$\xi = 1 - \frac{K_d}{K_m} \qquad [80]$$

Unfortunately, the use of eqn [80] in determining the appropriate effective pressure or stress in determining V_P or V_S has propagated through the rock physics literature. This usage is incorrect, as emphasized by Mavko and Vanorio (2010), and can lead to significant error particularly in compressible materials. For purposes of finding moduli or wave speeds, it is more proper to assume $\xi \approx 1$ in the absence of additional information on the material behavior.

The influence of effective pressure on seismic responses is of particular interest in time-lapse seismology. Pore pressures P_p in reservoirs will vary as fluids are injected or produced and this results in a change in the effective stress and, hence, V_P and V_S and the consequent seismic reflectivity. Proper interpretation of time-lapse observations cannot easily ignore the changes in the effective pressure or stress (Herwanger and Horne, 2005; Sayers, 2004).

11.03.6 Seismic Waves in Fluid-Saturated Rocks

Most commonly, a worker requires a prediction of the seismic wave speeds under the *in situ* conditions in the Earth where the rock is subject to various stresses, pore pressures, and fluid saturations. After providing information on the behavior of

the rock's various components of the mineral solid, the fluid, and the rock's frame in the preceding sections, we are now ready to review the approaches to understanding the seismic properties of fluid-saturated rocks. This is often referred to as a fluid substitution analysis. To summarize, the building blocks needed to determine the fluid-saturated bulk K_{sat} and shear μ_{sat} moduli that are necessary to calculate V_P and V_S with eqns [1] and [2] are as follows:

- The elastic moduli K_m and μ_m and density ρ_m of the solid mineral constituents.
- The saturating fluid's adiabatic bulk modulus K_f and its density ρ_f. If velocity dispersion is included, then one must also include the viscosity ζ.
- The rock frame's elastic dry or drained elastic moduli K_d and μ_d and its porosity ϕ. If frequency is considered, then one must also include additional factors such as the tortuosity τ, the permeability κ, and some measure of the dimensions of the pore.

Of course, one must remember that most of these depend on stress, pressure, and temperature as discussed in the previous sections and the values need to be appropriately chosen for the case at hand. After the intensive earlier discussions of the various mineral, fluid, and frame properties, the fluid-saturated expressions to come may seem anticlimactic. Often, finding the appropriate values of the inputs may take the most effort.

In this section, we review a number of the more important expressions that allow for the calculation of the saturated rock elastic moduli. This begins with Gassmann's widely employed formula and progresses through brief surveys of the local and global flow models that account for frequency effects.

11.03.6.1 Gassmann's Equation

Gassmann (1951) constructed expressions for the moduli of a fluid-saturated porous material. These expressions are relatively simple, and because of this, they are used almost exclusively in practice. His development is essentially that for an undrained poroelastic solid (Berryman, 1999; Rice and Cleary, 1976; Smith et al., 2003; Wang, 2000) and as such is strictly valid for static deformations. In developing his equations, he assumed the minerals and fluids interacted only mechanically, that the material was fully saturated and isotropic, that it was monomineralic, and, importantly, that the shear modulus is not influenced by the pore fluid. This last assumption leads to the expression for the saturated shear modulus μ_{sat}

$$\mu_{sat} = \mu_d \qquad [81]$$

and the saturated bulk modulus K_{sat}

$$K_{sat} = K_d + \frac{\xi^2}{\frac{\phi}{K_f} + \frac{\xi - \phi}{K_m}} \qquad [82]$$

where ξ is the poroelastic pore pressure coefficient of eqn [80]. Gassmann looked at the problem more as a superposition of interrelated volumetric strains of the frame, the minerals, and the fluid. The same result can be found independently as the undrained modulus from poroelasticity. Gassmann's formulas are written in many different ways, but one advantage of eqn [82] is that it highlights that the fluid effects are essentially a correction to K_d (Han and Batzle, 2004).

For the sake of convenience it is also worth rewriting an inverted form of Gassmann's equation [82]:

$$K_d = \frac{\left(\frac{\phi K_m}{K_f} + 1 - \phi\right) K_{sat} - K_m}{\frac{\phi K_m}{K_f} - 1 - \phi + \frac{K_{sat}}{K_m}} \qquad [83]$$

which is particularly useful in estimating K_d from sonic log information (Carcione et al., 2006).

Physically, the application of Gassmann's equations [81] and [82] assumes that during the passage of a wave over a small (relative to the wavelength) but representative volume V^R of the saturated rock, the frequency is sufficiently low that the pore pressure remains uniform throughout V^R. With no variations in pressure, there can be no fluid exchange between V^R and its neighboring representative volumes.

There are a number of salient points arising from Gassmann's equations including the following:

i. $K_{sat} \geq K_d$. That is, a fluid-saturated rock is always less compressible than the dry frame by itself.
ii. $1 \geq \xi \geq 0$. The upper bound occurs as K_d vanishes for increasingly compressible materials such as unconsolidated sands. It is interesting to note by examination that as $\xi \to 1$, K_{sat} approaches the Voigt bound equation [58] for the mixture of fluid and solid. The lower bound is approached as $K_d \to K_m$ where the rock is very stiff. Consequently, the influence of fluids diminishes as the frame stiffens.
iii. $K_m \gg K_f$. As **Tables 1** and **2** show, typical mineral moduli are mostly >30 GPa. In contrast, most typical liquid moduli are $\sim$1–3 GPa and gas moduli are $\sim$0.1–100 MPa (**Table 3**). As such, for real materials, K_{sat} is substantially more sensitive to K_f than to K_m. A corollary to this is that a compressible fluid (i.e., gas) has less effect than does a stiffer fluid (liquid).
iv. V_S will decrease upon saturation. The decrease, although it may only be small, occurs because, by definition, the shear modulus does not change but the bulk density ρ as given in eqns [55] and [56] must increase.
v. V_P will usually, but not necessarily, increase upon saturation. This increase is primarily due to the larger value of K_{sat}. However, one must always keep in mind that ρ_{sat} also rises, and should ρ_f be sufficiently large, it is quite possible that V_P will decrease upon saturation. This happens, for example, with pure CO_2 (e.g., see Njiekak et al., 2013).

It is worthwhile investigating the implications of Gassmann's equations. **Figure 24(a)** shows a suite of dry elastic moduli that might represent the values for a number of limestones with a range of porosities $0 \leq \phi \leq 0.4$. Both K_d and μ_d decrease substantially with porosity as expected. K_{sat} is calculated using eqn [82]; it is always greater than K_d but the two continue to diverge from one another with porosity and K_{sat} is nearly twice K_d once a porosity $\phi = 0.35$ is reached. The dry and saturated shear moduli are exactly the same according to Gassmann's assumptions in eqn [81].

The seismic wave speeds may subsequently be calculated using eqns [1] and [2] (**Figure 24(b)**). V_S decreases a small

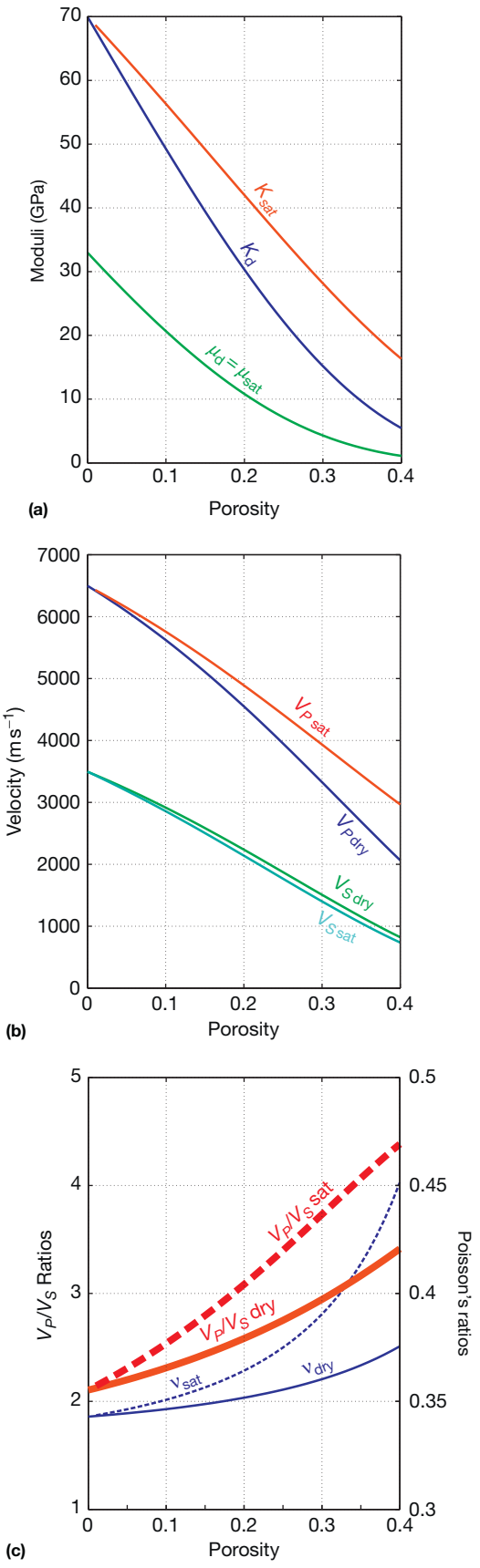

Figure 24 Illustration of the application of Gassmann's equations to a series of hypothetical rocks of increasing porosity. (a) Comparison of the dry frame modulus bulk K_d (blue) to the saturated bulk modulus K_{sat}. Note that by definition, the dry μ_d and saturated μ_{sat} shear moduli are equal. (b) Corresponding compressional and shear waves speeds for the dry and saturated cases. (c) Corresponding V_P/V_S and Poisson's ratios for the dry and saturated cases.

amount upon substitution because of the increase in the bulk density as already noted. For this case, however, V_P increases relative to that for the dry frame; the increase in the bulk modulus has managed to overwhelm the increase in the density. At the greater porosities (or equivalently smaller K_d), the saturating water has a greater influence on V_{Psat}. These differences would be further amplified for the acoustic impedances. It is these types of differences that hold the key to the time-lapse seismic surveying.

Figure 24(c) shows the two parameters that are often derived from the wave speeds, the direct V_P/V_S ratio and Poisson's ratio equation [9]. These can serve as proxy indicators of the saturation state of the rock in part because of the relative impacts of saturation on V_{Psat} and V_{Ssat}. For example, the V_P/V_S ratio for water saturation is substantially greater than that for the dry (or nearly equivalently gas-filled) conditions. This difference is even greater for Poisson's ratio ν with a larger Poisson's ratio, indicating liquid saturation.

11.03.6.2 Frequency-Dependent Models

Gassmann's equations remain popular, but as noted, they strictly apply only under static conditions. However, in reality, researchers must work over a large range of frequencies. In the broadest sense, 'seismic' investigations center on frequencies of 1 MHz, 10 kHz, and 100 Hz for ultrasonic laboratory measurements, borehole sonic log readings, and applied seismic investigations, respectively.

In the laboratory, Gassmann's equations rarely reproduce the observed wave speeds particularly at low confining pressures. An example of this, again taken from measurements on the Cadotte sandstone (He, 2006), is given in Figure 25 that shows the observed dry and water-saturated measurements as a function of the effective confining pressure. The observed V_{Psat} are greater than V_{Pdry} as expected but they exceed those values predicted using Gassmann's equations significantly. Similar anomalies are seen for V_{Ssat} that again is much greater than V_{Sdry}; this is in opposition to Gassmann's predicted values that are slightly smaller than V_{Sdry} because of the increased density of the bulk saturated material. It is important to note that as the crack-like porosity closes, the observed and predicted values begin to approach one another. Indeed, even at the pressure of only 60 MPa, V_{Ssat} has nearly intersected with V_{Sdry}. Clearly, there is a large discrepancy between the observed and predicted saturated wave speeds particularly at the low confining pressures where the cracks remain most open (see also Mavko and Jizba (1991) for similar evidence).

An extreme case of wave speed dispersion is seen from recent V_P and V_S measurements through a highly porous, CO_2-saturated medium of sintered alumina (Yam, 2011; Yam and Schmitt, 2011). Figure 26 shows the variations of the observed ultrasonic (1 MHz) V_{Psat} and V_{Ssat} with pore pressure P_p for a suite of measurements carried out at constant differential effective stress $P_{eff} = P - P_p$ of 15 MPa. As noted in the

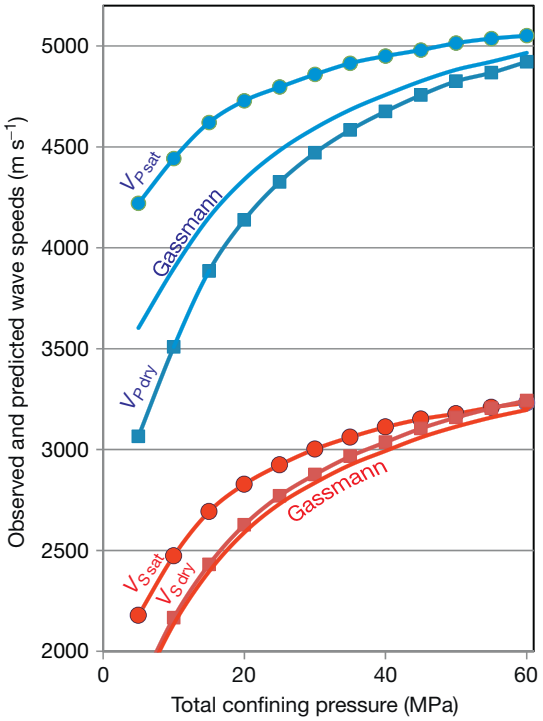

Figure 25 Observed V_P (blue) and V_S (red) wave speeds in Cadotte sandstone SB007 for dry (filled squares) and water-saturated (filled circles) situations. Theoretical Gassmann's wave speeds calculated using the dry moduli are also shown as lines.

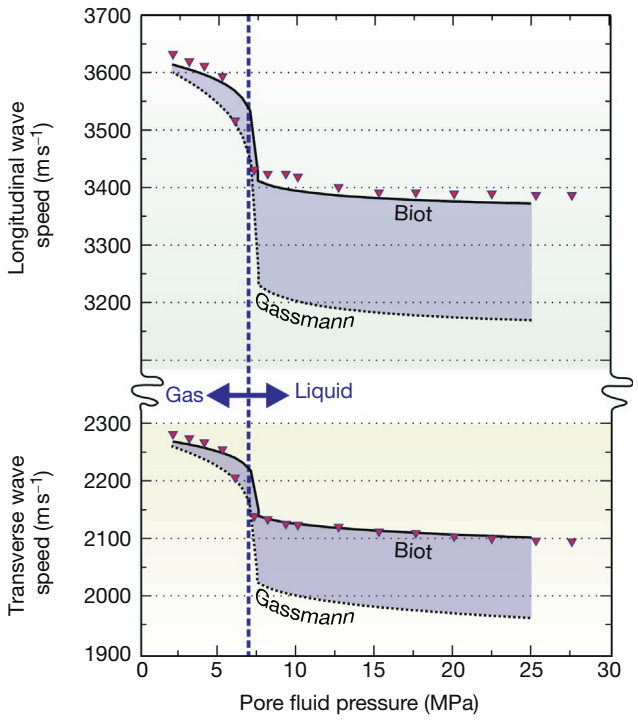

Figure 26 Comparison of observed ultrasonic wave speeds in a CO_2-saturated porous sintered alumina held at a constant differential pressure of $P_{eff} = 15$ MPa and temperature $T = 28$ °C. The pore pressure is varied in order to effect the gas–liquid phase transition that occurs at 6.144 MPa. Observed values of V_{Psat} and V_{Ssat} are indicated by red upside down triangles. Calculated values of the wave speeds according to the Biot formulations at 100 and 1 MHz are shown as dashed and solid black lines, respectively. For this case, the fluid substitution calculations using Gassmann's zero frequency equations cannot be distinguished from the 100 Hz Biot calculations. The violet-filled zones indicate the range of wave speed dispersion that exists between 100 Hz (Gassmann) and 1 MHz (Biot). Data and calculations from Yam (2011).

preceding text, carrying out the measurements at constant differential pressure should minimize any pressure-dependent effects of the rock frame of wave speeds and most of the variation will be due to changes in the fluid properties. Figure 26 also shows the corresponding wave speeds predicted by Gassmann's equations from fluid substitution calculations that employ knowledge of the fluid, solid, and dry frame properties. Gassmann's predictions are always less than the observations. This difference is relatively small when CO_2 gas saturates the pores but it grows to over 6% when the CO_2 is in the liquid state.

In the case shown, the differences between the observed and the predicted wave speeds at low frequencies arise primarily because the latter does not account for differential motions between the solid and fluid as the wave passes. We briefly survey the two main models in the succeeding text that do admit fluid motions. These are usually referred to as the global and local flow models.

11.03.6.2.1 Global flow (biot) model

Building on his work in the consolidation of porous media, Biot (1956a,b) constructed a seminal model to account for frequency-dependent wave propagation through a fluid-saturated porous and permeable medium. A full description of the model is beyond the needs here but readers can find more information in numerous contributions (Bourbié et al., 1987; Johnson, 1984; Smeulders, 2005). A most interesting outcome of this theory is that a third 'slow' longitudinal wave mode P_2 exists in such porous media because the fluid and solid are allowed to move independently of one another. This out-of-phase motion between the two admits a new degree of freedom to the equations of which the slow wave speed is the consequence.

This wave mode is difficult to observe in nature because the differential fluid–solid motions result in large viscous losses. Plona (1980) first observed this wave in acoustic refraction experiments through highly porous sintered glass beads. Figure 27 shows the results from similar recently conducted tests (Bouzidi and Schmitt, 2009) that highlight well the existence of all three modes. It is interesting to note the loss of the fast P_1 wave past its critical angle. The P_2 mode, which travels substantially more slowly than the surrounding water, has no critical angle and exists at all angles.

At this point, it is important to return to the CO_2-saturated measurements of Figure 26 where the Biot model has been used to predict the observed V_{Psat} and V_{Ssat}. The theory and observations match well as the observed and calculated values of V_{Ssat} agree to within experimental uncertainty. Those for V_{Psat} are only 20 m s^{-1} different. This agreement strongly suggests that the Biot model and its low-frequency limit given by Gassmann's equations adequately predict the behavior with frequency in highly porous and permeable materials. Although not shown here, the Biot formulas also allowed attenuation to be modeled satisfactorily (Yam, 2011).

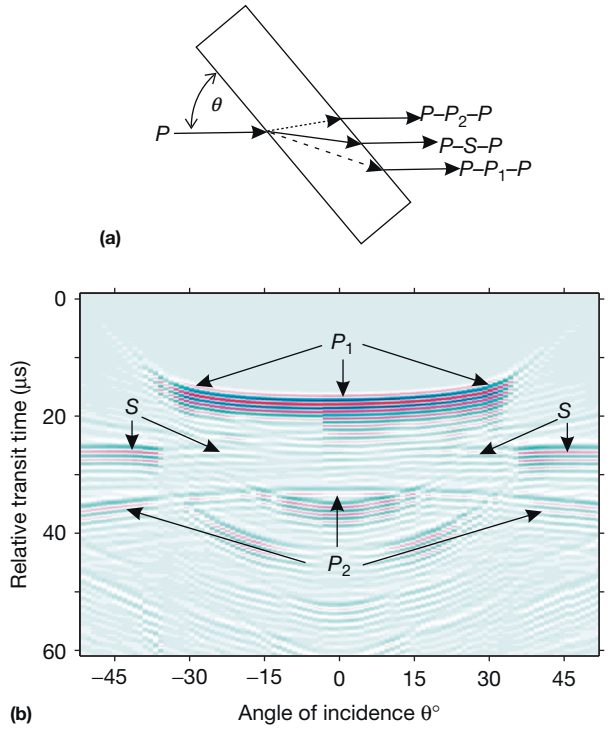

Figure 27 Experimental arrangement to show the existence of the slow wave. (a) Schematic of the experiment. An ultrasonic pulse insonifies a saturated porous plate immersed in a water tank with incoming longitudinal wave *P*. At the first boundary of the sample, the *P* wave converts to the 'fast' P_1, the *S*, and the 'slow' P_2 modes that propagate through the sample. These modes then are again converted back to separate *P* waves at the second surface and these waterborne arrivals are detected by an ultrasonic transducer. (b) Observed ultrasonic waveforms as a function of the incidence angle θ of the incoming waterborne *P* wave.

However, there are two problems with the use of the Biot formulas. First, properly carrying out the analysis requires knowledge of at least 14 different physical properties and characteristics of the porous medium. This is regrettably impractical in many situations. Second, the model does not account for all differential fluid motions within the porous rock and fails in predicting the wave speeds and attenuation through rocks containing compressible crack-like pores. This situation is discussed next.

11.03.6.2.2 Local flow (squirt) models

Although the concept was initially suggested by Mavko and Nur (1975), O'Connell and Budiansky (1977) carried out a theoretical analysis of a cracked solid containing cracks filled with a viscoelastic fluid. They noted that as long as the cracks are connected, then application of a stress to the porous medium allows the fluids to flow locally from those cracks preferentially oriented such that they compress (see **Figure 22**) into those cracks oriented more parallel to the stress. That is, the pressurized fluid in the compressed cracks 'squirts' into the uncompressed cracks. These fluid motions will preferentially occur at frequencies controlled by the crack density, effective permeability, and crack dimensions. At sufficiently high frequencies, the fluids cannot move fast enough and essentially become locked within the pores causing the medium to become stiffer. Similar phenomena can exist if the material contains both compressible cracks and stiffer equant pores.

O'Connell and Budiansky (1977) described a number of frequency domains that depend on the relationships between crack dimensions, frequency, and viscosity. Jackson (Lu and Jackson, 2006) had provided a particularly useful summary of their limiting cases that from high to low frequency are the *glued* (i.e., shear stresses do not have time to relax), the *saturated isolated* (i.e., shear stresses in the fluids relax but there is insufficient time for fluid exchange between pores), the *saturated isobaric* (i.e., adjacent pores can exchange fluids but there is no global fluid movement; this is similar to the undrained case of Gassmann's equations), and, finally, the *drained* case (i.e., bulk fluids can move in or out of the material to equilibrate the pore pressure and the moduli act as if the sample were dry).

These shifts between fluid-flow regimes impact the moduli and attenuation in different ways as illustrated in **Figure 28**. A large shift in the bulk modulus K occurs for the transition from the drained to undrained conditions. At low frequencies, there is no dispersion in the shear moduli μ across this same transition. Once viscous forces come into play, however, the shear moduli stiffen in the transitions from the saturated isobaric to the saturated isolated and from the saturated isolated to the glued regimes. A peak in the attenuation is expected at each of these jumps in the moduli with higher frequency.

These developments have been useful conceptually but finding appropriate expressions to account for these local flow effects has remained challenging. One issue is that the actual dimensions of the cracks play a significant role but appropriately assessing crack sizes is not easily accomplished. Mavko and Jizba (1991) attempted to indirectly account for the local flow effects by measuring the 'crack-free' modulus at high confining pressures in order to provide an estimate of the 'wet frame modulus.' These moduli are then used in Gassmann's equations to provide for a prediction of the high-frequency moduli. Work continues on this issue with numerous recent contributions (Adelinet et al., 2011; Dvorkin et al., 1995; LeRavalec and Gueguen, 1996; Schubnel and Gueguen, 2003).

11.03.7 Empirical Relations and Data Compilations

The sections in the preceding text have attempted to give some sense of the problems associated with predicting the seismic properties of rocks. Often, however, there is far from sufficient information in order to justifiably carry out such predictions, and workers rely instead on the observations of others. There are numerous drawbacks to this. For example, from the perspective of geology, the name of a rock type may reveal a great deal about how a rock was formed, what minerals might be in it, and what its texture is. However, the geologic name by itself may have little meaning from the perspective of the rock's physical properties except in the broadest of senses. Despite this, sometimes this is the only information that we have available.

Mavko et al. (2003) had already extensively reviewed a number of existing empirical relationships for a wide variety of rock types; as such we do not need to reproduce all of these

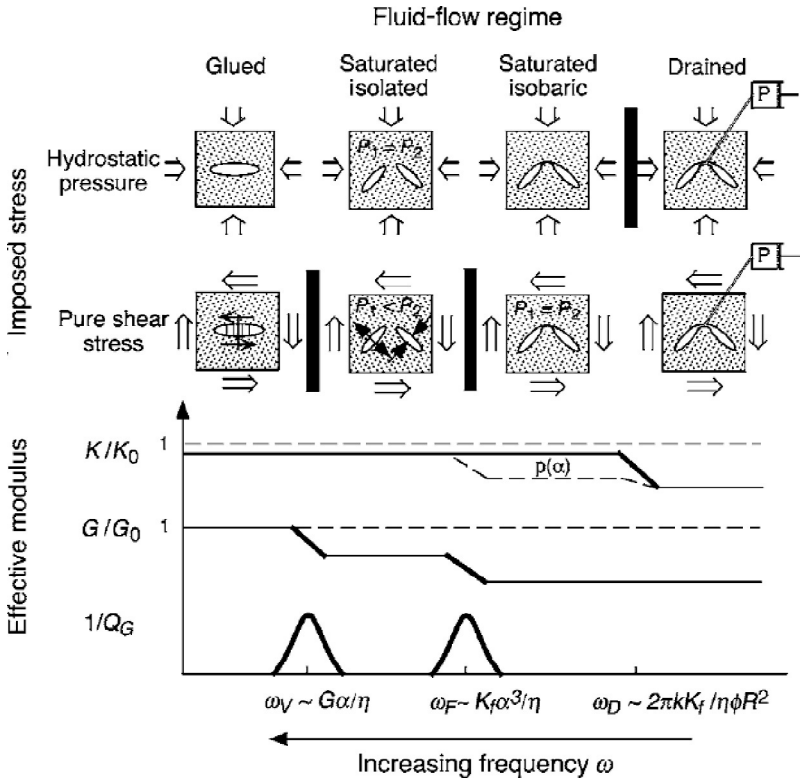

Figure 28 Description of the fluid-flow regimes expected in a cracked and fluid-saturated solid during passage of a harmonic wave according to O'Connell and Budiansky (1977) as explained by Lu and Jackson (2006). Figure 10 from Lu and Jackson (2006) with permission granted according the Society of Exploration Geophysicists fair use policy.

here, but we provide a few that have been popular in the literature. Dvorkin (2008) also provided a listing of many of the simpler linear fits for V_P and V_S.

Eberhart-Phillips et al. (1989) fitted various functions to the large ultrasonic data set of saturated shaley sandstones obtained by Han (1986) and arrived at the forms

$$V_P = 5.77 - 6.94\phi - 1.73\sqrt{C} + 0.446(P_{\text{eff}} - \exp(-16.7P_{\text{eff}}))$$
$$V_S = 3.70 - 4.94\phi - 1.57\sqrt{C} + 0.361(P_{\text{eff}} - \exp(-16.7P_{\text{eff}})) \quad [84]$$

where V_P and V_S are in km s^{-1}, C is the clay volume fraction, and P_{eff} is the differential pressure in kilobars (1 kbar = 100 MPa).

Castagna et al. (1985) derived what they called a 'mudrock' line from sonic logs allowing V_S to be predicted from V_P for siliclastics using

$$V_S = 0.862V_P - 1.1172 \quad [85]$$

where both velocities are in km s^{-1}. This simple linear fit has surprising predictive power. Jorstad et al. (1999) later carried out their own regression for their area of study and produced a remarkably similar relation:

$$V_S = 0.8966V_P - 1.1665 \quad [86]$$

Following the earlier work of Pickett (1963), Castagna et al. (1993) also developed a set of quadratic regression polynomials relating V_S to V_P for the pure lithologies of sandstone, limestone, dolomite, and shale saturated fully with brine of the form

$$V_{Si} = a_{i2}V_P^2 + a_{i1}V_P + a_{i0} \quad [87]$$

with the resulting empirical coefficients a_{i0}, a_{i1}, and a_{i2} provided in Table 4. Note that except for limestone, a linear fit suffices to describe the V_S–V_P relationships.

Table 4 Quadratic regression coefficients for pure rock types of Castagna et al. (1993)

Rock type	a_{i2}	a_{i1}	a_{i0}	R^2
Sandstone	0	0.80416	−0.8558	0.98352
Limestone	−0.05508	1.01677	−1.3049	0.99096
Dolomite	0	0.58324	−0.07775	0.87444
Shale	0	0.76969	−0.86735	0.97939

Greenberg and Castagna (1992, 1993) developed an iterative method that allows mixing of pure monomineralic 'lithologies' of sandstone (quartz), limestone (calcite), dolomite (dolomite), and shale (illite) lithologies together to predict V_S for variable fluid saturations. Their method is somewhat analogous to Hill's mean value of the Voigt–Reuss bounds as described in Section 11.03.5.2. Essentially, the strategy is to find the 'best' predicted value of the compressional wave velocity V_{P1C} of the rock under study when it is brine-saturated. Once this is found, the equivalent brine-saturated shear wave

velocity is calculated using the empirical regressions of Equation [87] just described. With knowledge of the brine-saturated density, one can easily calculate the rock's shear modulus μ_d that in turn can be used to calculate the proper shear wave velocity for the saturation at the proper saturation state using the rock's density ρ_{sat}.

Hence, the basis of the method is to make a proper estimate of V_{P1C}. To carry this out, one must have appropriate knowledge of the rock's porosity ϕ, its *in situ* saturations S_w, S_o, and S_g (see eqns [56] and [57]), and its observed *in situ* compressional velocity V_{Psat}. Further, the solid volume fractions X_i of the L different 'lithologies'

$$\sum_{i=0}^{L} X_i = 1 \qquad [88]$$

forming the rock's frame must also be found.

In the Greenberg and Castagna method, they first guess a value of the compressional wave speed V_{P1C} for the rock fully saturated with brine (i.e., $S_w = 1$). With the guess V_{P1C}, one can directly calculate the expected values V_{Si} for each of the lithologies using eqn [87] and **Table 4**. Using these V_{Si}, the shear wave velocity for the brine-saturated rock V_{S1C} is calculated in a manner analogous to the Voigt–Reuss–Hill calculations:

$$V_{S1C} = \frac{1}{2}\left\{\left[\sum_{i=0}^{L} X_i V_{Si}\right] + \left[\sum_{i=0}^{L} \frac{X_i}{V_{Si}}\right]^{-1}\right\} \qquad [89]$$

The density of the brine-saturated rock ρ_{1C} is calculated using an adaptation of eqn [55]:

$$\rho_{1C} = \phi\rho_w + (1-\phi)\sum_{i=1}^{L} X_i \rho_{mi} \qquad [90]$$

where the brine density must be determined for the appropriate conditions as discussed in **Section 11.03.4.3.2.1**. Note that the Greenberg and Castagna (1992) lithologies are sandstone, limestone, dolomite, and shale. The mineral densities ρ_{mi} that they employed for these lithologies are, respectively, those for quartz, calcite, dolomite, and illite as could be obtained from **Table 2**. The *in situ* saturated density ρ_{sat} can be either directly observed or calculated with an additional adaptation of eqn [56]:

$$\rho_{sat} = \phi\left(\sum_{j=1}^{n} S_j \rho_j^f\right) + (1-\phi)\sum_{i=1}^{L} X_i \rho_{mi} \qquad [91]$$

With the values of V_{S1C} and ρ_{1C}, the drained shear modulus μ_d using eqn [2]

$$\mu_d = V_{S1C}^2 \rho_{1C} \qquad [92]$$

may be calculated. The saturated bulk modulus K_{sat} of the rock in situ with its proper saturation is then from eqn [1]:

$$K_{sat} = V_{Psat}^2 \rho_{sat} - \frac{4}{3}\mu_d \qquad [93]$$

The drained frame modulus K_d may then be determined using the inverse Gassmann's equation [83] with knowledge of the appropriate K_f for the pore fluids and K_m for the mineral solids discussed in earlier sections. Now, the calculations are run somewhat backward in order to provide an updated value for the fully brine-saturated ($S_w = 1$) compressional wave speed V'_{P1C} using eqn [1]:

$$V'_{P1C} = \left\{\left[\left(K_d + \frac{\xi^2}{\frac{\phi}{K_w} + \frac{\xi-\phi}{K_m}}\right) + \frac{4}{3}\mu_d\right]\rho_{1C}^{-1}\right\}^{1/2} \qquad [94]$$

with the bulk modulus of the brine K_w taking the place of K_f in Gassmann's equation [82]. V'_{P1C} can then be used as the new V_{P1C} and the calculation repeated. This process can iterate until V'_{P1C} and V_{P1C} converge within acceptable limits. Once the convergence is complete, the current value of μ_d is accepted and the final estimate of the shear wave velocity V_{Ssat} is simply calculated using eqn [2]:

$$V_{Ssat} = \sqrt{\frac{\mu_d}{\rho_{sat}}} \qquad [95]$$

Raymer et al. (1980) also using well log information developed a piecewise relationship to predict velocity from knowledge of porosity and the intrinsic compressional wave speeds V_{Pm} and V_f for the constituent mineral and solid, respectively. This formula is

$$\begin{aligned} V_P &= (1-\phi)^2 V_{Pm} + \phi V_f, \ \phi < 0.37 \\ \frac{1}{\rho V_P^2} &= \frac{\phi}{\rho_f V_f^2} + \frac{1-\phi}{\rho_m V_{Pm}^2}, \ \phi > 0.47 \\ \frac{1}{V_P} &= \frac{0.47-\phi}{0.10}\frac{1}{V_{37}} + \frac{\phi-0.37}{0.10}\frac{1}{V_{47}}, \ 0.37 < \phi < 0.47 \end{aligned} \qquad [96]$$

where V_{37} and V_{47} are the velocities of the saturated rock for $\phi = 37\%$ and $\phi = 47\%$, respectively. Dvorkin (2008) more recently came up with a similar relation to predict shear wave velocities:

$$V_S = (1-\phi)^2 V_{Sm}\left[\frac{(1-\phi)\rho_m}{(1-\phi)\rho_m + \phi\rho_f}\right] \qquad [97]$$

given knowledge of the intrinsic mineral shear wave velocity V_{Sm} and the fluid and intrinsic mineral densities, ρ_f and ρ_m, respectively.

Hamilton (1979) derived a number of expressions for velocities in marine sediments (primarily silt–clays, turbidites, and mudstone shales); one of these relates V_P (in km s^{-1}) to depth D (in km) by

$$V_P = 1.511 + 1.304D - 0.741D^2 + 0.257D^3 \qquad [98]$$

which is accurate to about 800 m depth.

The general empirical relationship between density and seismic velocity fit by Gardner et al. (Gardner et al., 1974; Sayers and den Boer, 2011) is still widely applied in seismic studies particularly if only one of the other logs is available from a borehole

$$\rho \approx 1.741 V_P^{0.25} \qquad [99]$$

with V_P in km s^{-1} and ρ in g cm^{-3}.

More recently, Christensen and Stanley (2003) carried out a fit of V_P and V_S versus ρ from a compilation of laboratory measurements on a variety of igneous, metamorphic, and sedimentary rocks yielding

$$V_P = 2.8\rho - 1.5752 \qquad [100]$$

and

$$V_S = 1.4\rho - 0.4019 \qquad [101]$$

where again the velocities are in km s^{-1} and ρ in g cm^{-3}.

Examination of these regressions shows that, for the most part, they do not contain any physical principles. Hence, the reader must take care when applying these formulas and know their limitations.

Compilations of observed values of velocities and densities are also important sources of information. The densities of rocks and minerals are covered extensively by Wohlenberg (1982), while in the same series, Gebrande (1982) and Kern (1982) provided exhaustive listings of wave speeds as functions of pressure for various rock types. Christensen (1982, 1989) had provided the results of thousands of ultrasonic velocity laboratory measurements that have been used to create sophisticated models of the continental crust (Christensen and Mooney, 1995). Ji et al.'s (2002) compilation is perhaps the most complete in that it contains the results of both modeling and measurements for a wide variety of different rock types. Most recently, Gercek (2007) had compiled values of Poisson's ratio for a number of different Earth materials.

11.03.8 The Road Ahead

Studies related to 'seismic properties' continue to rapidly expand, and in reality, each of the topics touched on in the preceding text could be easily be turned into textbooks on their own. In writing such a review, some important issues were overlooked. The listing in the succeeding text contains important directions of investigation that I believe will be of increasing importance in the coming decade. These include the following:

i. Seismic anisotropy was touched on only in the context of mineral properties, but in general, rock is an anisotropic medium. Since the 1980s, geophysicists have dominated the literature on elastic anisotropy. As noted earlier, we do not really have a good understanding of the anisotropy of 'shales.' This is in part because the physical properties of clay mineralogical constituents are still not well known. Characterizing the clay mineralogy within a given sample remains problematic. The clay minerals themselves are difficult to study as the 'crystals' are often no more than a few nanometers in dimension. The effects of cracks and fractures on seismic responses still remain elusive. Being able to deconvolve seismic observations to detect and characterize fractures remains a goal for the future.
ii. Although it has been hinted at in the discussions earlier in the text, we currently do not have a good handle on seismic velocity dispersion in the Earth. Progress in this field should come more rapidly with the development of a variety of forcing-function stress–strain techniques that can allow the complex elastic moduli to be found at seismic frequencies.
iii. We have seen earlier that most rocks display nonlinear stress–strain or stress–velocity behavior. Despite this, we still cling to attempting to analyze much of our observed seismic data under the linearly elastic assumption. Currently, only a handful of workers are studying the often unexpected effects of wave propagation in nonlinear materials. It is likely that this field can gain from the much larger community of workers in nonlinear optics.
iv. In the laboratory, we often work on decimeter-scale samples that appear uniform and homogeneous. We then attempt to extend this assumption of homogeneity to much larger scales over many tens of meters (about the seismic wavelengths). However, there are subtle dispersion effects introduced by the scale of the heterogeneity of a rock mass relative to the interrogating seismic waves. For example, we most usually work under the ray theory paradigm that assumes the wavelengths are small relative to the dimensions of the heterogeneity. This is likely only rarely true, and in many cases, the waves we observe may more actually be revealing an effective medium. Much work remains to be done on assessing to what degree effective medium concepts may need to be incorporated to our field observations.
v. Finally, the remarkable growth in computing power and in easily employed parallel multiphysics numerical modeling together with parallel technical developments in benchtop x-ray tomography systems with micrometer-scale resolving power is leading to the rapid growth of 'digital rock physics.' These techniques allow one to calculate a variety of physical properties from the 3-D microtomograms. Estimation of electrical conductivity and permeability has been most successful so far, but accurate predictions of the elastic moduli and wave speeds have not yet been adequately solved. This is in part because for the most part, workers have focused on continuum approaches to solving such problems. Now, however, one can build actual models mimicking the true architecture of the minerals and pore space and more thought needs to go on with regard to actual physical phenomena in porous media at that scale before the seismic properties can be adequately modeled.

Taken together, there still remains a great deal to learn with regard to seismic properties of rocks. The new computational, imaging, and experimental tools now at our disposal will allow for rapid progress over the next decade.

Acknowledgments

The help of the many graduate students, postdoctoral researchers, and technical staff in making many of the measurements described in the preceding text is greatly appreciated. DRS is supported by the Canada Research Chairs Program. The author thanks T. Smith and the Editor L. Slater for providing ideas on improving the manuscript.

References

Adams LH and Williamson ED (1923) On the compressibility of minerals and rocks at high pressures. *Journal of the Franklin Institute* 195: 475–529.

Adelinet M, Fortin J, and Gueguen Y (2011) Dispersion of elastic moduli in a porous-cracked rock: Theoretical predictions for squirt-flow. *Tectonophysics* 503: 173–181.

Alam MM, Fabricius IL, and Christensen HF (2012) Static and dynamic effective stress coefficient of chalk. *Geophysics* 77: L1–L11.

Alexandrov KS and Ryzhova TV (1961a) The elastic properties of rock forming minerals I: Pyroxenes and amphiboles. *Bulletin (izvestiya), Academy of Sciences, USSR. Geophysics Series*, vol. 9, pp. 871–875.

Alexandrov KS and Ryzhova TV (1961b) The elastic properties of rock forming minerals II: Layered silicates. *Bulletin (izvestiya), Academy of Sciences, USSR. Geophysics Series*, vol. 12, pp. 1799–1804.

Alexandrov KS and Ryzhova TV (1962) The elastic properties of rock forming minerals III: Feldspars. *Bulletin (izvestiya), Academy of Sciences, USSR. Geophysics Series*, vol. 2, pp. 186–189.

Alexandrov KS and Ryzhova TV (1964) The elastic properties of pyroxenes. *Soviet Physics – Crystallography* 8: 589–591.

Almqvist BSG, Burlini L, Mainprice D, and Hirt AM (2010) Elastic properties of anisotropic synthetic calcite-muscovite aggregates. *Journal of Geophysical Research, Solid Earth* 115: B08203.

Andersen CF and Johansen TA (2010) Test of rock physics models for prediction of seismic velocities in shallow unconsolidated sands: A well log data case. *Geophysical Prospecting* 58: 1083–1098.

Anderson OL (1963) A simplified method for calculating debye temperature from elastic constants. *Journal of Physics and Chemistry of Solids* 24: 909–917.

Angel RJ, Jackson JM, Reichmann HJ, and Speziale S (2009) Elasticity measurements on minerals: A review. *European Journal of Mineralogy* 21: 525–550.

Angus DA, Verdon JP, Fisher QJ, and Kendall JM (2009) Exploring trends in microcrack properties of sedimentary rocks: An audit of dry-core velocity-stress measurements. *Geophysics* 74: E193–E203.

Auld BA (1990) Acoustic Fields and Waves in Solids, 2nd edn., p. 432. New York: John Wiley and Sons.

Auzende AL, Pellenq RJM, Devouard B, Baronnet A, and Grauby O (2006) Atomistic calculations of structural and elastic properties of serpentine minerals: The case of lizardite. *Physics and Chemistry of Minerals* 33: 266–275.

Azeemuddin M, Scott TE, Zaman M, and Roegiers JC (2001) *Stress-Dependent Biot's Constant Through Dynamic Measurements on Ekofisk Chalk*. Paper presented at 38th Symposium on Rock Mechanics: DC Rocks 2001. New York: Balkema.

Babuska V (1972) Elasticity and anisotropy of dunite and bronzitite. *Journal of Geophysical Research* 77: 6955–6965.

Babuška V and Cara M (1991) *Seismic Anisotropy in the Earth*. Netherlands: Springer.

Babuska V and Pros Z (1984) Velocity anisotropy in granodiorite and quartzite due to the distribution of microcracks. *Geophysical Journal of the Royal Astronomical Society* 76: 113–119.

Bachrach R and Avseth P (2008) Rock physics modeling of unconsolidated sands: Accounting for nonuniform contacts and heterogeneous stress fields in the effective media approximation with applications to hydrocarbon exploration. *Geophysics* 73: E197–E209.

Bachrach R, Dvorkin J, and Nur AM (2000) Seismic velocities and poisson's ratio of shallow unconsolidated sands. *Geophysics* 65: 559–564.

Bailey E and Holloway JR (2000) Experimental determination of elastic properties of talc to 800 degrees C, 0.5 GPa; Calculations of the effect on hydrated peridotite, and implications for cold subduction zones. *Earth and Planetary Science Letters* 183: 487–498.

Bakhorji A (2009) *Laboratory Measurements of Static and Dynamic Elastic Properties in Carbonate*. PhD, University of Alberta.

Bass JD (1995) Elasticity of minerals, glasses, and melts. In: Ahrens TJ (ed.) *Mineral Physics and Crystallography: A Handbook of Physical Constants*, pp. 45–63. Washington, DC: American Geophysical Union.

Batzle M and Wang ZJ (1992) Seismic properties of pore fluids. *Geophysics* 57: 1396–1408.

Becker K, Shapiro SA, Stanchits S, Dresen G, and Vinciguerra S (2007) Stress induced elastic anisotropy of the Etnean basalt: Theoretical and laboratory examination. *Geophysical Research Letters* 34: L11307.

Behura J, Batzle M, Hofmann R, and Dorgan J (2007) Heavy oils: Their shear story. *Geophysics* 72: E175–E183.

Belogol'skii VA, Sekoyan SS, Samorukova LM, Stefanov SR, and Levtsov VI (1999) Pressure dependence of the sound velocity in distilled water. *Measurement Techniques* 42: 406–413.

Benedict M, Webb GB, and Rubin LC (1942) An empirical equation for thermodynamic properties of light hydrocarbons and their mixtures II. Mixtures of methane, ethane, propane, and *n*-butane. *Journal of Chemical Physics* 10: 747–758.

Benedict M, Webb GB, and Rubin LC (1951) An empirical equation for thermodynamic properties of light hydrocarbons and their mixtures – Constants for 12 hydrocarbons. *Chemical Engineering Progress* 47: 419–422.

Berg CA (1965) Deformation of fine cracks under high pressure and shear. *Journal of Geophysical Research* 70: 3447–3452.

Berge PA, Bonner BP, and Berryman JG (1995) Ultrasonic velocity porosity relationships for sandstone analogs made from fused glass-beads. *Geophysics* 60: 108–119.

Bernabe Y (1987) The effective pressure law for permeability during pore pressure and confining pressure cycling of several crystalline rocks. *Journal of Geophysical Research-Solid Earth and Planets* 92: 649–657.

Berryman JG (1992) Effective stress for transport-properties of inhomogeneous porous rock. *Journal of Geophysical Research, Solid Earth* 97: 17409–17424.

Berryman JG (1993) Effective-stress rules for pore-fluid transport in rocks containing 2 minerals. *International Journal of Rock Mechanics and Mining Sciences & Geomechanics Abstracts* 30: 1165–1168.

Berryman JG (1995) Mixture theories for rock properties. In: *Rock Physics & Phase Relations*, pp. 205–228. Washington, DC: American Geophysical Union.

Berryman JG (1999) Origin of gassmann's equations. *Geophysics* 64: 1627–1629.

Berryman JG (2005) Bounds and self-consistent estimates for elastic constants of random polycrystals with hexagonal, trigonal, and tetragonal symmetries. *Journal of the Mechanics and Physics of Solids* 53: 2141–2173.

Berryman JG (2012) Evaluating bounds and estimators for constants of random polycrystals composed of orthotropic elastic materials. *International Journal of Engineering Science* 58: 11–20.

Berryman JG and Berge PA (1996) Critique of two explicit schemes for estimating elastic properties of multiphase composites. *Mechanics of Materials* 22: 149–164.

Berryman JG, Pride SR, and Wang HF (2002) A differential scheme for elastic properties of rocks with dry or saturated cracks. *Geophysical Journal International* 151: 597–611.

Bett KE, Rowlinson JS, and Saville G (2003) *Thermodynamics for Chemical Engineers*. Cambridge: MIT Press.

Bianco E, Kaplan S, and Schmitt DR (2010) Seismic rock physics of steam injection in bituminous-oil reservoirs – Chapter 6. In: Batzle ML, Chopra S, Lines LR, and Schmitt DR (eds.) *Heavy Oils: Reservoir Characterization and Production Monitoring*, pp. 105–110. Tulsa: Society of Exploration Geophysicists.

Biot MA (1956a) Theory of propagation of elastic waves in a fluid-saturated porous solid.1. Low-frequency range. *Journal of the Acoustical Society of America* 28: 168–178.

Biot MA (1956b) Theory of propagation of elastic waves in a fluid-saturated porous solid.2. Higher frequency range. *Journal of the Acoustical Society of America* 28: 179–191.

Biot MA and Willis D (1957) The elastic coefficients of the theory of consolidation. *Journal of Applied Mechanics-Transactions of the ASME* 24: 594–601.

Birch F (1947) Finite elastic strain of cubic crystals. *Physical Review* 71: 809–824.

Birch F (1960) The velocity of compressional waves in rocks to 10-kilobars.1. *Journal of Geophysical Research* 65: 1083–1102.

Birch F (1961) The velocity of compressional waves in rocks to 10 kilobars, part 2. *Journal of Geophysical Research* 66: 2199–2224.

Blake OO, Faulkner DR, and Rietbrock A (2013) The effect of varying damage history in crystalline rocks on the *P*- and *S*-wave velocity under hydrostatic confining pressure. *Pure and Applied Geophysics* 170: 493–505.

Bonner BP (1974) Shear wave birefringence in dilating granite. *Geophysical Research Letters* 1: 217–220.

Bourbié T, Coussy O, and Zinszner B (1987) *Acoustics of Porous Media*. Houston, TX: Gulf.

Bouzidi YS and Schmitt DR (2009) Measurement of the speed and attenuation of the biot slow wave using a large ultrasonic transmitter. *Journal of Geophysical Research* 114: B08201.

Bower AF (2010) *Applied Mechanics of Solids*. Boca Raton: Taylor and Francis.

Brace WF (1965) Some new measurements of linear compressibility of rocks. *Journal of Geophysical Research* 70: 391–398.

Brace WF and Martin RJ (1968) A test of law of effective stress for crystalline rocks of low porosity. *International Journal of Rock Mechanics and Mining Sciences* 5: 415–426.

Brown JM, Abramson EH, and Angel RJ (2006) Triclinic elastic constants for low albite. *Physics and Chemistry of Minerals* 33: 256–265.

Budiansky B and O'Connell RJ (1976) Elastic-moduli of a cracked solid. *International Journal of Solids and Structures* 12: 81–97.

Bunge H (1974) The effective elastic constants of textured polycrystals in second order approximation. *Kristall und Technik* 9: 413–424.

Calderon E, Gauthier M, Decremps F, Hamel G, Syfosse G, and Polian A (2007) Complete determination of the elastic moduli of alpha-quartz under hydrostatic pressure up to 1 GPa: An ultrasonic study. *Journal of Physics: Condensed Matter* 19: 436228.

Carcione JM (2007) *Wave Fields in Real Media: Wave Propagation in Anisotropic, Anelastic, Porous and Electromagnetic Media*. Amsterdam: Elsevier Science.

Carcione JM, Picotti S, Gei D, and Rossi G (2006) Physics and seismic modeling for monitoring CO_2 storage. *Pure and Applied Geophysics* 163: 175–207.

Carcione JM and Tinivella U (2001) The seismic response to overpressure: A modelling study based on laboratory, well and seismic data. *Geophysical Prospecting* 49: 523–539.

Carey WM and Evans RB (2011) *A Review of the Sonic Properties of Bubbly Liquids*. New York: Springer.

Carvalho FCS and Labuz JF (1996) Experiments on effective elastic modulus of two-dimensional solids with cracks and holes. *International Journal of Solids and Structures* 33: 4119–4130.

Castagna JP, Batzle ML, and Eastwood RL (1985) Relationships between compressional-wave and shear-wave velocities in clastic silicate rocks. *Geophysics* 50: 571–581.

Castagna JP, Batzle ML, and Kan TK (1993) Rock physics – The link between rock properties and AVO response. In: Castagna JP and Backus M (eds.) *Offset-Dependent Reflectivity – Theory and Practice of AVO Analysis*, pp. 135–171. Tulsa: Society of Exploration Geophysicists.

Castellan GW (1971) *Physical Chemistry*, 2nd edn. New York: Addison-Wesley.

Castier M (2011) Thermodynamic speed of sound in multiphase systems. *Fluid Phase Equilibria* 306: 204–211.

Chen C-T and Millero F (1976) Reevaluation of Wilson's sound-speed measurements for pure water. *The Journal of the Acoustical Society of America* 60: 1270–1273.

Cheng C and Toksöz M (1979) Inversion of seismic velocities for the pore aspect ratio spectrum of a rock. *Journal of Geophysical Research, Solid Earth* 84: 7533–7543.

Cheyne SA, Stebbings CT, and Roy RA (1995) Phase-velocity measurements in bubbly liquids using a fiber optic laser interferometer. *Journal of the Acoustical Society of America* 97: 1621–1624.

Chitale DV and Sigal R (2000) NMR characterization of the water adsorbed by montmorillonite: Impact on the analysis of porosity logs: Spe 62531. In: *SPE/AAPG Western Regional Meeting*, Long Beach: Society of Petroleum Engineers.

Cholach PY, Molyneux JB, and Schmitt DR (2005) Flin flon belt seismic anisotropy: Elastic symmetry, heterogeneity, and shear-wave splitting. *Canadian Journal of Earth Sciences* 42: 533–554.

Cholach PY and Schmitt DR (2006) Intrinsic elasticity of a textured transversely isotropic muscovite aggregate: Comparisons to the seismic anisotropy of schists and shales. *Journal of Geophysical Research, Solid Earth* 30: 111–116.

Christensen NI (1982) Seismic velocities. In: Carmichael RS (ed.) *Handbook of Physical Properties of Rocks*, vol. II, pp. 1–228. Boca Raton: CRC Press.

Christensen NI (1989) Seismic velocities. In: Carmichael R (ed.) *Practical Handbook of Physical Properties of Rocks and Minerals*, pp. 429–546. Boca Raton: CRC.

Christensen NI (2004) Serpentinites, peridotites, and seismology. *International Geology Review* 46: 795–816.

Christensen NI and Mooney WD (1995) Seismic velocity structure and composition of the continental-crust – A global view. *Journal of Geophysical Research, Solid Earth* 100: 9761–9788.

Christensen NI and Stanley D (2003) Seismic velocities and densities of rocks. In: Lee W, Kanamori H, Jennings P, and Kissinger C (eds.) *International Handbook of Earthquake and Engineering Seismology*, pp. 1587–1594. New York: Academic Press.

Christensen NI and Wang HF (1985) The influence of pore pressure and confining pressure on dynamic elastic properties of berea sandstone. *Geophysics* 50: 207–213.

Ciz R and Shapiro SA (2009) Stress-dependent anisotropy in transversely isotropic rocks: Comparison between theory and laboratory experiment on shale. *Geophysics* 74: D7–D12.

Clark VA (1992) The effect of oil under in situ conditions on the seismic properties of rocks. *Geophysics* 57: 894–901.

Commander KW and Prosperetti A (1989) Linear pressure waves in bubbly liquids – Comparison between theory and experiments. *Journal of the Acoustical Society of America* 85: 732–746.

Condon E (1933) Note on the velocity of sound. *American Journal of Physics* 1: 18.

Coppens A (1981) Simple equations for the speed of sound in neptunian waters. *The Journal of the Acoustical Society of America* 69: 862–863.

Crampin S (1994) The fracture criticality of crustal rocks. *Geophysical Journal International* 118: 428–438.

Crampin S and Peacock S (2008) A review of the current understanding of seismic shear-wave splitting in the earth's crust and common fallacies in interpretation. *Wave Motion* 45: 675–722.

Crosson R and Lin J (1971) Voigt and reuss prediction of anisotropic elasticity of dunite. *Journal of Geophysical Research* 76: 570–578.

Cundall PA and Strack ODL (1979) Discrete numerical-model for granular assemblies. *Geotechnique* 29: 47–65.

Daridon JL, Lagourette B, Xans P, and Montel F (1998) Petroleum characterization from ultrasonic measurement. *Journal of Petroleum Science and Engineering* 19: 281–293.

David EC and Zimmerman RW (2011) Elastic moduli of solids containing spheroidal pores. *International Journal of Engineering Science* 49: 544–560.

David EC and Zimmerman RW (2012) Pore structure model for elastic wave velocities in fluid-saturated sandstones. *Journal of Geophysical Research, Solid Earth* 117: B07210.

Del Grosso VA (1974) New equation for speed of sound in natural-waters (with comparisons to other equations). *Journal of the Acoustical Society of America* 56: 1084–1091.

Del Grosso VA and Mader CW (1972) Speed of sound in pure water. *Journal of the Acoustical Society of America* 52: 1442–1446.

Diamond LW and Akinfiev NN (2003) Solubility of CO_2 in water from −1.5 to 100 degrees c and from 0.1 to 100 MPa: Evaluation of literature data and thermodynamic modelling. *Fluid Phase Equilibria* 208: 265–290.

Digby PJ (1981) The effective elastic-moduli of porous granular rocks. *Journal of Applied Mechanics-Transactions of the ASME* 48: 803–808.

Dillen MWP, Cruts HMA, Groenenboom J, Fokkema JT, and Duijndam AJW (1999) Ultrasonic velocity and shear-wave splitting behavior of a colton sandstone under a changing triaxial stress. *Geophysics* 64: 1603–1607.

Domenico S (1977) Elastic properties of unconsolidated porous sand reservoirs. *Geophysics* 42: 1339–1368.

Duan Z, Hu J, Li D, and Mao S (2008) Densities of the CO_2–H_2O and CO_2–H_2O–NaCl systems up to 647 K and 100 MPa. *Energy & Fuels* 22: 1666–1674.

Duan ZH and Sun R (2003) An improved model calculating CO_2 solubility in pure water and aqueous NaCl solutions from 273 to 533 k and from 0 to 2000 bar. *Chemical Geology* 193: 257–271.

Dvorkin JP (2008) Yet another Vs equation. *Geophysics* 73: E35–E39.

Dvorkin J, Mavko G, and Nur A (1995) Squirt flow in fully saturated rocks. *Geophysics* 60: 97–107.

Eberhart-Phillips D, Han DH, and Zoback MD (1989) Empirical relationships among seismic velocity, effective pressure, porosity, and clay content in sandstone. *Geophysics* 54: 82–89.

Ebrahimi D, Pellenq RJM, and Whittle AJ (2012) Nanoscale elastic properties of montmorillonite upon water adsorption. *Langmuir* 28: 16855–16863.

Elbra T, Karlqvist R, Lassila I, Haeggstrom E, and Pesonen LJ (2011) Laboratory measurements of the seismic velocities and other petrophysical properties of the Outokumpu deep drill core samples, eastern Finland. *Geophysical Journal International* 184: 405–415.

Evelein K, Moore R, and Heidemann R (1976) Correlation of phase behavior in systems hydrogen-sulfide – Water and carbon-dioxide–water. *Industrial & Engineering Chemistry Process Design and Development* 15: 423–428.

Ezekwe N (2010) *Petroleum Reservoir Engineering Practice*. New York: Prentice Hall.

Fabricius IL, Gommesen L, Krogsboll A, and Olsen D (2008) Chalk porosity and sonic velocity versus burial depth: Influence of fluid pressure, hydrocarbons, and mineralogy. *AAPG Bulletin* 92: 201–223.

Fam M and Santamarina JC (1997) A study of consolidation using mechanical and electromagnetic waves. *Geotechnique* 47: 203–219.

Fereidoon V, Embleton J, and Lines LR (2010) The effects of cold production on seismic response. In: Chopra S, Lines LR, Schmitt DR, and Batzle M (eds.) *Heavy Oils: Reservoir Characterization and Production Monitoring*, pp. 237–241. Tulsa: Society of Exploration Geophysicists, ch. 18.

Fletcher NH (1974) Adiabatic assumption for wave-propagation. *American Journal of Physics* 42: 487–489.

Fletcher N (1976) Adiabatic assumption for wave propagation. *American Journal of Physics* 44: 486–487.

Freund D (1992) Ultrasonic compressional and shear velocities in dry clastic rocks as a function of porosity, clay content, and confining pressure. *Geophysical Journal International* 108: 125–135.

Fridleifsson GO and Elders WA (2005) The iceland deep drilling project: A search for deep unconventional geothermal resources. *Geothermics* 34: 269–285.

Fuck RF and Tsvankin I (2009) Analysis of the symmetry of a stressed medium using nonlinear elasticity. *Geophysics* 74: WB79–WB87.

Fung YC (1965) *Foundations of Solid Mechanics*. New York: Prentice Hall.

Gallagher JS, Crovetto R, and Sengers J (1993) The thermodynamic behavior of the CO_2–H_2O system from 400-K to 1000-K, up to 100 MPa and 30-percent mole fraction of CO_2. *Journal of Physical and Chemical Reference Data* 22: 431–513.

Gallop J (2013) Extended walton third-order elastic coefficients modified by an anisotropic and stress-dependent coordination number. *Geophysics* 78: D545–D556.

Gao K and Gibson RL Jr. (2012) Pressure-dependent seismic velocities based on effective compliance theory and an asperity deformation model. *Geophysics* 77: D229–D243.

Gardner GHF, Gardner LW, and Gregory AR (1974) Formation velocity and density – Diagnostic basics for stratigraphic traps. *Geophysics* 39: 770–780.

Gassmann F (1951) Über die elastizität poröser medien. *Vierteljahrsschrift der Naturforschenden Gesellschaft in Zurich* 96: 1–23.

Gebrande H (1982) Elastic wave velocities and constants of elasticity at normal conditions. In: *The Landolt-Bornstein Database*, pp. 1–99. Berlin: Springer-Verlag.

Gercek H (2007) Poisson's ratio values for rocks. *International Journal of Rock Mechanics and Mining Sciences* 44: 1–13.

Goddard JD (1990) Nonlinear elasticity and pressure-dependent wave speeds in granular media. *Proceedings of The Royal Society A Mathematical Physical and Engineering Sciences* 430: 105–131.

Gomez CT, Dvorkin J, and Vanorio T (2010) Laboratory measurements of porosity, permeability, resistivity, and velocity on fontainebleau sandstones. *Geophysics* 75: E191–E204.

Gray C, Gubbins K, and Joslin C (2011) Thermodynamic properties of mixtures. In: Gray C, Gubbins K, and Joslin C (eds.) *Theory of Molecular Fluids. Applications*, vol. 2, pp. 761–886. New York: Oxford University Press.

Greenberg ML and Castagna JP (1992) Shear-wave velocity estimation in porous rocks – Theoretical formulation, preliminary verification and applications. *Geophysical Prospecting* 40: 195–209.

Greenberg ML and Castagna JP (1993) Shear-wave velocity estimation in porous rocks – Theoretical formulation, preliminary verification and applications (vol 40, pg 195, 1992). *Geophysical Prospecting* 41: 515.

Gucker FT, Stubley D, and Hill DJ (1975) Isentropic compressibilities of aqueous-solutions of some alkali-halides at 298.15 K. *Journal of Chemical Thermodynamics* 7: 865–873.

Gueguen Y and Bouteca M (2004) *Mechanics of Fluid-Saturated Rocks*. Amsterdam/Boston: Elsevier/Academic Press.

Gurevich B, Pervukhina M, and Makarynska D (2011) An analytic model for the stress-induced anisotropy of dry rocks. *Geophysics* 76: WA125–WA133.

Hamilton EL (1979) $V_p - V_s$ and Poisson ratios in marine-sediments and rocks. *Journal of the Acoustical Society of America* 66: 1093–1101.

Han DH (1986) *Effects of Porosity and Clay Content on Acoustic Properties of Sandstones and Unconsolidated Sediments*. PhD, Stanford University.

Han D-H and Batzle M (2000) Velocity, density and modulus of hydrocarbon fluids – Data measurement. In: *Society of Exploration Geophysicists 70th Annual Meeting and Exposition, Calgary: Society of Exploration Geophysicist*.

Han DH and Batzle ML (2004) Gassmann's equation and fluid-saturation effects on seismic velocities. *Geophysics* 69: 398–405.

Han D-H, Sun M, and Batzle M (2010) CO_2 velocity measurement and models for temperatures up to 200 degrees C and pressures up to 100 MPa. *Geophysics* 75: E123–E129.

Han D-H, Sun M, and Batzle M (2011) CO_2 velocity measurement and models for temperatures up to 200 degrees C and pressures up to 100 MPa. *Geophysics* 75: e123–e129.

Hardin BO and Blandford GE (1989) Elasticity of particulate materials. *Journal of Geotechnical Engineering, ASCE* 115: 788–805.

Hashin Z and Shtrikman S (1962) On some variational principles in anisotropic and nonhomogeneous elasticity. *Journal of the Mechanics and Physics of Solids* 10: 335–342.

Hashin Z and Shtrikman S (1963) A variational approach to the theory of the elastic behaviour of multiphase materials. *Journal of the Mechanics and Physics of Solids* 11: 127–140.

He T (2006) *P and S Wave Velocity Measurement and Pressure Sensitivity Analysis of AVA Response*. MSc, University of Alberta.

Hearmon RFS (1946) The elastic constants of anisotropic materials. *Reviews of Modern Physics* 18: 409–440.

Hearmon RFS (1956) The elastic constants of anisotropic materials – II. *Advances in Physics* 5: 323–382.

Helgeson HC and Kirkham DH (1974) Theoretical prediction of thermodynamic behavior of aqueous electrolytes at high pressures and temperatures. 1. Summary of thermodynamic-electrostatic properties of solvent. *American Journal of Science* 274: 1089–1198.

Hemley RJ, Mao HK, and Struzhkin VV (2005) Synchrotron radiation and high pressure: New light on materials under extreme conditions. *Journal of Synchrotron Radiation* 12: 135–154.

Herwanger J and Horne S (2005) Predicting time-lapse stress effects in seismic data. *The Leading Edge* 24: 1234–1242.

Hill R (1952) The elastic behaviour of a crystalline aggregate. *Proceedings of the Physical Society. Section A* 65: 349–355.

Hill R (1965) A self-consistent mechanics of composite materials. *Journal of the Mechanics and Physics of Solids* 13: 213–222.

Holland TJB and Powell R (1998) An internally consistent thermodynamic data set for phases of petrological interest. *Journal of Metamorphic Geology* 16: 309–343.

Holmes GM, Crampin S, and Young RP (2000a) Controlled sources for shear-wave surveys in mines. *Geophysical Prospecting* 48: 399–414.

Holmes GM, Crampin S, and Young RP (2000b) Seismic anisotropy in granite at the underground research laboratory, Manitoba. *Geophysical Prospecting* 48: 415–435.

Holzapfel GA (2000) *Nonlinear Solid Mechanics: A Continuum Approach for Engineering*. Chichester, NY: Wiley.

Horii H and Nemat-Nasser S (1983) Overall moduli of solids with microcracks: Load-induced anisotropy. *Journal of the Mechanics and Physics of Solids* 31: 155–171.

Hou SX, Maitland GC, and Trusler JPM (2013) Measurement and modeling of the phase behavior of the (carbon dioxide plus water) mixture at temperatures from 298.15 K to 448.15 K. *Journal of Supercritical Fluids* 73: 87–96.

Hu J, Duan Z, Zhu C, and Chou IM (2007) Pvtx properties of the CO_2–H_2O and CO_2–H_2O–NaCl systems below 647 K: Assessment of experimental data and thermodynamic models. *Chemical Geology* 238: 249–267.

Hu M, O'sullivan C, Jardine R, and Jiang M (2010) Stress-induced anisotropy in sand under cyclic loading. *Granular Matter* 12: 469–476.

Hudson JA (1981) Wave speeds and attenuation of elastic-waves in material containing cracks. *Geophysical Journal of the Royal Astronomical Society* 64: 133–150.

Huntington HB (1958) The elastic constants of crystals. *Solid State Physics: Advances in Research and Applications* 7: 213–351.

IAPWS (2008) *Release on the IAPWS Formulation 2008 for the Thermodynamic Properties of Seawater*. Berlin: International Association for the Properties of Water and Steam.

IAPWS (2011) *Revised Release on the Pressure along the Melting and Sublimation Curves of Ordinary Water Substance*, Available: http://www.iapws.org/relguide/MeltSub2011.pdf (accessed 25 June 2013).

Ji SC, Wang Q, and Xia B (2002) *Handbook of Seismic Properties of Minerals, Rocks and Ores*. Montreal: Polytechnic International Press.

Johnson DL (1984) Recent developments in the acoustic properties of porous media. In: Sette D (ed.) *Frontiers in Physical Acoustics*, *Proceedings of the International School of Physics "Enrico Fermi" Course XCIII*, pp. 255–290.

Johnson K (1987) *Contact Mechanics*. New York: Cambridge University Press.

Johnson PA and Rasolofosaon PNJ (1996) Nonlinear elasticity and stress-induced anisotropy in rock. *Journal of Geophysical Research, Solid Earth* 101: 3113–3124.

Jones T and Nur A (1983) Velocity and attenuation in sandstone at elevated-temperatures and pressures. *Geophysical Research Letters* 10: 140–143.

Jorstad A, Mukerji T, and Mavko G (1999) Model-based shear-wave velocity estimation versus empirical regressions. *Geophysical Prospecting* 47: 785–797.

Kachanov M (1980) Continuum model of medium with cracks. *Journal of the Engineering Mechanics Division, ASCE* 106: 1039–1051.

Kachanov M, Tsukrov I, and Shafiro B (1994) Effective moduli of solids with cavities of various shapes. *Applied Mechanics Reviews* 1: S151–S174.

Kanitpanyacharoen W, Wenk HR, Kets F, Lehr C, and Wirth R (2011) Texture and anisotropy analysis of qusaiba shales. *Geophysical Prospecting* 59: 536–556.

Karmous MS (2011) Theoretical study of kaolinite structure; energy minimization and crystal properties. *The World Journal of Nano Science and Engineering* 1: 62–66.

Kay WB (1936) Density of hydrocarbon gases and vapors at high temperature and pressure. *Industrial and Engineering Chemistry* 28: 1014–1019.

Kell GS (1975) Density, thermal expansivity, and compressibility of liquid water from 0 degrees to 150 degrees. Correlations and tables for atmospheric-pressure and saturation reviewed and expressed on 1968 temperature scale. *Journal of Chemical and Engineering Data* 20: 97–105.

Kern H (1982) Elastic wave velocities and constants of elasticity of rocks at elevated pressures and temperatures. In: *The Landolt-Bornstein Database*, pp. 99–140. Berlin: Springer-Verlag.

Kern H, Mengel K, Strauss KW, Ivankina TI, Nikitin AN, and Kukkonen IT (2009) Elastic wave velocities, chemistry and modal mineralogy of crustal rocks sampled by the outokumpu scientific drill hole: Evidence from lab measurements and modeling. *Physics of the Earth and Planetary Interiors* 175: 151–166.

Khaksar A, Griffiths CM, and Mccann C (1999) Compressional- and shear-wave velocities as a function of confining stress in dry sandstones. *Geophysical Prospecting* 47: 487–508.

Khazanehdari J and Mccann C (2005) Acoustic and petrophysical relationships in low-shale sandstone reservoir rocks. *Geophysical Prospecting* 53: 447–461.

Khazanehdari J and Sothcott J (2003) Variation in dynamic elastic shear modulus of sandstone upon fluid saturation and substitution. *Geophysics* 68: 472–481.

Khidas Y and Jia XP (2010) Anisotropic nonlinear elasticity in a spherical-bead pack: Influence of the fabric anisotropy. *Physical Review E* 81: 021303.

Kieffer SW (1977) Sound speed in liquid-gas mixtures – Water-air and water-steam. *Journal of Geophysical Research* 82: 2895–2904.

Kirstetter O, Corbett P, Somerville J, and Macbeth C (2006) Elasticity/saturation relationships using flow simulation from an outcrop analogue for 4D seismic modelling. *Petroleum Geoscience* 12: 205–219.

Kumar A (2003) Speed of sound in concentrated aqueous KCl solutions from 278.15 to 338.15 K. *Journal of Chemical and Engineering Data* 48: 388–391.

Kumazawa M (1969) The elastic constant of polycrystalline rocks and nonelastic behavior inherent to them. *Journal of Geophysical Research* 74: 5311–5320.

Kunz O and Wagner W (2012) The gerg-2008 wide-range equation of state for natural gases and other mixtures: An expansion of gerg-2004. *Journal of Chemical and Engineering Data* 57: 3032–3091.

Kuster GT and Toksöz MN (1974a) Velocity and attenuation of seismic-waves in 2-phase media. 1. Theoretical formulations. *Geophysics* 39: 587–606.

Kuster GT and Toksöz MN (1974b) Velocity and attenuation of seismic-waves in 2-phase media. 2. Experimental results. *Geophysics* 39: 607–618.

Kwon O, Kronenberg AK, Gangi AF, and Johnson B (2001) Permeability of wilcox shale and its effective pressure law. *Journal of Geophysical Research, Solid Earth* 106: 19339–19353.

Lakes RS (2009) *Viscoelastic Materials*. New York: Cambridge University Press.

Laliberte M and Cooper WE (2004) Model for calculating the density of aqueous electrolyte solutions. *Journal of Chemical and Engineering Data* 49: 1141–1151.

Landau LD and Lifshitz EM (1959) *Fluid Mechanics*. New York: Pergamon Press.

Landau LD and Lifshitz EM (1970) *Theory of Elasticity*. Oxford: Pergamon Press.

Lassila I, Karlqvist R, Elbra T, Gates FK, Pesonen LJ, and Haeggstrom E (2010) Ultrasonic velocity of the upper gneiss series rocks from the outokumpu deep drill hole, fennoscandian shield – Comparing uniaxial to triaxial loading. *Journal of Applied Geophysics* 72: 178–183.

Lemmon EW, Jacobsen RT, Penoncello SG, and Friend DG (2000) Thermodynamic properties of air and mixtures of nitrogen, argon, and oxygen from 60 to 2000 k at pressures to 2000 MPa. *Journal of Physical and Chemical Reference Data* 29: 331–385.

Lemmon EW, Mclinden MO, and Friend DG (2012a) Thermophysical properties of fluid systems. In: Lindstrom PJ and Mallard WG (eds.) *NIST Chemistry WebBook, NIST Standard Reference Database Number 69*. Gaithersburg, MD: National Institute of Standards and Technology.

Lemmon EW, Mclinden MO, and Friend DG (eds.) (2012b) *Thermophysical Properties of Fluid Systems*. Gaithersburg, MD: National Institute of Standards and Technology.

Leravalec M and Gueguen Y (1996) High- and low-frequency elastic moduli for a saturated porous/cracked rock – Differential self-consistent and poroelastic theories. *Geophysics* 61: 1080–1094.

Li HB and Zhang JJ (2011) Elastic moduli of dry rocks containing spheroidal pores based on differential effective medium theory. *Journal of Applied Geophysics* 75: 671–678.

Lin C-W and Trusler JPM (2012) The speed of sound and derived thermodynamic properties of pure water at temperatures between (253 and 473) k and at pressures up to 400 MPa. *Journal of Chemical Physics* 136: 094511.

Lo TW, Coyner KB, and Toksöz MN (1986) Experimental-determination of elastic-anisotropy of berea sandstone, chicopee shale, and chelmsford granite. *Geophysics* 51: 164–171.

Lowell S, Shields JE, Thomas MA, and Thommes M (2004) *Characterization of Porous Solids and Powders: Surface Area, Pore Size and Density*. Amsterdam: Springer.

Lu C and Jackson I (2006) Low-frequency seismic properties of thermally cracked and argon-saturated granite. *Geophysics* 71: F147–F159.

Lumley DE (2001) Time-lapse seismic reservoir monitoring. *Geophysics* 66: 50–53.

Lyakhovsky V, Reches Z, Weinberger R, and Scott TE (1997) Non-linear elastic behaviour of damaged rocks. *Geophysical Journal International* 130: 157–166.

Mackenzie JK (1950) The elastic constants of a solid containing spherical holes. *Proceedings of the Physical Society. Section B* 63: 2–11.

Mackenzie KV (1981) 9-term equation for sound speed in the oceans. *Journal of the Acoustical Society of America* 70: 807–812.

Mainprice D (1990) A fortran program to calculate seismic anisotropy from the lattice preferred orientation of minerals. *Computers & Geosciences* 16: 385–393.

Mainprice D and Humbert M (1994) Methods of calculating petrophysical properties from lattice preferred orientation data. *Surveys in Geophysics* 15: 575–592.

Makse HA, Gland N, Johnson DL, and Schwartz LM (1999) Why effective medium theory fails in granular materials. *Physical Review Letters* 83: 5070–5073.

Man CS and Huang MJ (2011) A simple explicit formula for the Voigt–Reuss–Hill average of elastic polycrystals with arbitrary crystal and texture symmetries. *Journal of Elasticity* 105: 29–48.

Mao S, Duan Z, and Hu W (2009) A vapor-liquid phase equilibrium model for binary CO_2–H_2O and CH_4–H_2O systems above 523 K for application to fluid inclusions. *The Journal of Supercritical Fluids* 50: 13–21.

Matthies S and Humbert M (1993) The realization of the concept of a geometric mean for calculating physical constants of polycrystalline materials. *Physica Status Solidi B: Basic Research* 177: K47–K50.

Mavko G and Jizba D (1991) Estimating grain-scale fluid effects on velocity dispersion in rocks. *Geophysics* 56: 1940–1949.

Mavko G, Mukerji T, and Dvorkin J (2003) *The Rock Physics Handbook: Tools for Seismic Analysis in Porous Media*. New York: Cambridge University Press.

Mavko G and Nur A (1975) Melt squirt in asthenosphere. *Journal of Geophysical Research* 80: 1444–1448.

Mavko GM and Nur A (1978) The effect of nonelliptical cracks on the compressibility of rocks. *Journal of Geophysical Research, Solid Earth* 83: 4459–4468.

Mavko G and Vanorio T (2010) The influence of pore fluids and frequency on apparent effective stress behavior of seismic velocities. *Geophysics* 75: N1–N7.

Meister R and Peselnick L (1966) Variational method of determining effective moduli of polycrystals with tetragonal symmetry. *Journal of Applied Physics* 37: 4121–4125.

Melendez Martinez J and Schmitt DR (2013) Anisotropic elastic moduli of carbonates and evaporites from the Weyburn-Midale reservoir and seal rocks. *Geophysical Prospecting* 61: 363–379.

Militzer B, Wenk H-R, Stackhouse S, and Stixrude L (2011) First-principles calculation of the elastic moduli of sheet silicates and their application to shale anisotropy. *American Mineralogist* 96: 125–137.

Mookherjee M and Stixrude L (2009) Structure and elasticity of serpentine at high-pressure. *Earth and Planetary Science Letters* 279: 11–19.

Mori T and Tanaka K (1973) Average stress in matrix and average elastic energy of materials with misfitting inclusions. *Acta Metallurgica* 21: 571–574.

Morris PR (2006) Polycrystal elastic constants for triclinic crystal and physical symmetry. *Journal of Applied Crystallography* 39: 502–508.

Nichita DV, Khalid P, and Broseta D (2010) Calculation of isentropic compressibility and sound velocity in two-phase fluids. *Fluid Phase Equilibria* 291: 95–102.

Nist (2010a) *NIST Reference Fluid Thermodynamic and Transport Properties Database (RefProp): Version 9.1 [Online]*. Gaithersburg, MD: National Institute of Standards and Technology, Available: http://www.nist.gov/srd/nist23.cfm.

Nist (2010b) *NIST/ASME Steam Properties Database: Version 3.0, the Latest IAPWS Standard Formulation [Online]*. Gaithersburg, MD: National Institute of Standards and Technology, Available: http://www.nist.gov/srd/nist10.cfm.

Njiekak G, Schmitt DR, Yam H, and Kofman RS (2013) CO_2 rock physics as part of the Weyburn-Midale geological storage project. *International Journal of Greenhouse Gas Control* 16S: S118–S133.

Norris AN (1985) A differential scheme for the effective moduli of composites. *Mechanics of Materials* 4: 1–16.

Nur A (1971) Effects of stress on velocity anisotropy in rocks with cracks. *Journal of Geophysical Research* 76: 2022–2034.

Nur A and Byerlee JD (1971) An exact effective stress law for elastic deformation of rock with fluids. *Journal of Geophysical Research* 76: 6414–6419.

Nur A and Simmons G (1969) Stress-induced velocity anisotropy in rock – An experimental study. *Journal of Geophysical Research* 74: 6667–6674.

O'Connell RJ and Budiansky B (1977) Viscoelastic properties of fluid-saturated cracked solids. *Journal of Geophysical Research* 82: 5719–5735.

Oakley BA, Barber G, Worden T, and Hanna D (2003a) Ultrasonic parameters as a function of absolute hydrostatic pressure. I. A review of the data for organic liquids. *Journal of Physical and Chemical Reference Data* 32: 1501–1533.

Oakley BA, Hanna D, Shillor M, and Barber G (2003b) Ultrasonic parameters as a function of absolute hydrostatic pressure. II. Mathematical models of the speed of sound in organic liquids. *Journal of Physical and Chemical Reference Data* 32: 1535–1544.

O'Connell RJ and Budiansky B (1974) Seismic velocities in dry and saturated cracked solids. *Journal of Geophysical Research* 79: 5412–5426.

Ohno I, Abe M, Kimura M, Hanayama Y, Oda H, and Suzuki I (2000) Elasticity measurement of silica glass under gas pressure. *American Mineralogist* 85: 288–291.

Ohno I, Harada K, and Yoshitomi C (2006) Temperature variation of elastic constants of quartz across the alpha-beta transition. *Physics and Chemistry of Minerals* 33: 1–9.

Payan C, Garnier V, Moysan J, and Johnson PA (2009) Determination of third order elastic constants in a complex solid applying coda wave interferometry. *Applied Physics Letters* 94: 011904.

Peng DY and Robinson DB (1976) A new two-constant equation of state. *Industrial and Engineering Chemistry Fundamentals* 15: 59–64.

Peselnick L and Meister R (1965) Variational method of determining effective moduli of polycrystals – (a) Hexagonal symmetry (b) trigonal symmetry. *Journal of Applied Physics* 36: 2879–2884.

Pham DC (2011) On the scatter ranges for the elastic moduli of random aggregates of general anisotropic crystals. *Philosophical Magazine* 91: 609–627.

Picard DJ and Bishnoi PR (1987) Calculation of the thermodynamic sound-velocity in 2-phase multicomponent fluids. *International Journal of Multiphase Flow* 13: 295–308.

Pickett GR (1963) Acoustic character logs and their applications in formation evaluation. *Transactions of the Society of Petroleum Engineers of AIME* 228: 659–667.

Plantier F, Bessieres D, Daridon JL, and Montel F (2008) Structure and thermodynamic consistency of heavy oils: A study on the basis of acoustic measurements. *Fuel* 87: 196–201.

Plona TJ (1980) Observation of a 2nd bulk compressional wave in a porous-medium at ultrasonic frequencies. *Applied Physics Letters* 36: 259–261.

Prasad M and Manghnani MH (1997) Effects of pore and differential pressure on compressional wave velocity and quality factor in berea and michigan sandstones. *Geophysics* 62: 1163–1176.

Prikryl R, Klima K, Lokajicek T, and Pros Z (2005) Non-linearity in multidirectional *P*-wave velocity; confining pressure behaviour based on real 3D laboratory measurements, and its mathematical approximation. In: Brewer TS, Pezard PA, Petrov VA, and Harvey PK (eds.) *Petrophysical Properties of Crystalline Rocks*, pp. 323–334. London: Geological Society of London.

Prioul R, Bakulin A, and Bakulin V (2004) Nonlinear rock physics model for estimation of 3d subsurface stress in anisotropic formations: Theory and laboratory verification. *Geophysics* 69: 415–425.

Rai CS and Hanson KE (1988) Shear-wave velocity anisotropy in sedimentary-rocks – A laboratory study. *Geophysics* 53: 800–806.

Raymer L, Hunt ER, and Gardner J (1980) An improved sonic transit time-to-porosity transform. In: Paper P (ed.) *21st Annual Logging Symposium*, Layfayette: Soc. of Well Log Analysts.

Reuss A (1929a) Berechnung der fließgrenze von mischkristallen auf grund der plastizitätsbedingung für einkristalle. *Journal of Applied Mathematics and Mechanics (Z. Angew. Math. Mech)* 9: 49–58.

Reuss A (1929b) Berechnungd er fliessgrenzey on mischkristallen auf grund der plastiziffitsbedingunfagr einkristall. *Zeitschrift für Angewandte Mathematik und Mechanik* 9: 49–58.

Rice JR and Cleary MP (1976) Some basic stress diffusion solutions for fluid-saturated elastic porous-media with compressible constituents. *Reviews of Geophysics* 14: 227–241.

Rivers ML and Carmichael ISE (1987) Ultrasonic studies of silicate melts. *Journal of Geophysical Research-Solid Earth and Planets* 92: 9247–9270.

Roesler SK (1979) Anisotropic shear modulus due to stress anisotropy. *Journal of the Geotechnical Engineering Division, ASCE* 105: 871–880.

Rogers PSZ and Pitzer KS (1982) Volumetric properties of aqueous sodium-chloride solutions. *Journal of Physical and Chemical Reference Data* 11: 15–81.

Rowe AM and Chou JCS (1970) Pressure–volume–temperature–concentration relation of aqueous NaCl solutions. *Journal of Chemical and Engineering Data* 15: 61–66.

Ryzhova TV, Alexandrov KS, and Korobkova VM (1966) The elastic properties of rock forming minerals v. Additional data on silicates. *Izvestiya, Earth Physics* 2: 63–65.

Safarov J, Berndt S, Millero F, Feistel R, Heintz A, and Hassel E (2012) (p, ρ, t) properties of seawater: Extensions to high salinities. *Deep Sea Research Part I: Oceanographic Research Papers* 65: 146–156.

Safarov J, Berndt S, Millero FJ, Feistel R, Heintz A, and Hassel E (2013) (p, r, t) properties of seawater at brackish salinities: Extension to high temperatures and pressures. *Deep-Sea Research Part 1* 78: 95–101.

Safarov J, Millero F, Feistel R, Heintz A, and Hassel E (2009) Thermodynamic properties of standard seawater: Extensions to high temperatures and pressures. *Ocean Science* 5: 235–246.

Sato H, Ono K, Johnston CT, and Yamagishi A (2005) First-principles studies on the elastic constants of a 1:1 layered kaolinite mineral. *American Mineralogist* 90: 1824–1826.

Sayers CM (1999) Stress-dependent seismic anisotropy of shales. *Geophysics* 64: 93–98.

Sayers CM (2002) Stress-dependent elastic anisotropy of sandstones. *Geophysical Prospecting* 50: 85–95.

Sayers C (2004) Monitoring production – Induced stress changes using seismic waves. *SEG Technical Program Expanded Abstracts* 2004: 2287–2290.

Sayers CM (2007) Effects of borehole stress concentration on elastic wave velocities in sandstones. *International Journal of Rock Mechanics and Mining Sciences* 44: 1045–1052.

Sayers CM and Den Boer LD (2011) Rock physics-based relations for density and *S*-velocity versus *P*-velocity in deepwater subsalt Gulf of Mexico shales. *The Leading Edge* 30: 1376–1381.

Sayers CM and Kachanov M (1995) Microcrack-induced elastic wave anisotropy of brittle rocks. *Journal of Geophysical Research, Solid Earth* 100: 4149–4156.

Sayers CM, Vanmunster JG, and King MS (1990) Stress-induced ultrasonic anisotropy in Berea sandstone. *International Journal of Rock Mechanics and Mining Sciences & Geomechanics Abstracts* 27: 429–436.

Schijns H, Schmitt DR, Heikkinen PJ, and Kukkonen IT (2012) Seismic anisotropy in the crystalline upper crust: Observations and modelling from the outokumpu scientific borehole, finland. *Geophysical Journal International* 189: 541–553.

Schmitt DR (1999) Seismic attributes for monitoring of a shallow heated heavy oil reservoir: A case study. *Geophysics* 64: 368–377.

Schmitt DR, Han Z, Kravchinsky VA, and Escartin J (2007) Seismic and magnetic anisotropy of serpentinized ophiolite: Implications for oceanic spreading rate dependent anisotropy. *Earth and Planetary Science Letters* 261: 590–601.

Schmitt DR and Li Y (1995) A high-pressure technique for determining the microcrack porosities of damaged brittle materials. *Canadian Journal of Physics* 73: 330–337.

Schmitt DR, Mwenifumbo J, Pflug KA, and Meglis IL (2003) Geophysical logging for elastic properties in hard rock: A tutorial. In: Eaton DW, Milkereit B, and Salisbury MH (eds.) *Hardrock Seismic Exploration*, pp. 20–41. Tulsa: Society of Exploration Geophysicists.

Schmitt DR, Smither C, and Ahrens TJ (1989) In situ holographic elastic-moduli measurements from boreholes. *Geophysics* 54: 468–477.

Schmitt DR and Zoback MD (1992) Diminished pore pressure in low-porosity crystalline rock under tensional failure – Apparent strengthening by dilatancy. *Journal of Geophysical Research, Solid Earth* 97: 273–288.

Schubnel A, Benson PM, Thompson BD, Hazzard JF, and Young RP (2006) Quantifying damage, saturation and anisotropy in cracked rocks by inverting elastic wave velocities. *Pure and Applied Geophysics* 163: 947–973.

Schubnel A and Gueguen Y (2003) Dispersion and anisotropy of elastic waves in cracked rocks. *Journal of Geophysical Research, Solid Earth* 108: 2101–2116.

Setzmann U and Wagner W (1989) A new method for optimizing the structure of thermodynamic correlation equations. *International Journal of Thermophysics* 10: 1103–1126.

Setzmann U and Wagner W (1991) A new equation of state and tables of thermodynamic properties for methane covering the range from the melting line to 625-K at pressures up to 1000-MPa. *Journal of Physical and Chemical Reference Data* 20: 1061–1155.

Sharqawy MH, Lienhard JH, and Zubair SM (2010) Thermophysical properties of seawater: A review of existing correlations and data. *Desalination and Water Treatment* 16: 354–380.

Simmons G and Wang HF (1971) *Single Crystal Elastic Constants and Calculated Aggregate Properties: A Handbook*. Cambridge, MA: MIT Press.

Sinha BK and Kostek S (1996) Stress-induced azimuthal anisotropy in borehole flexural waves. *Geophysics* 61: 1899–1907.

Smeulders DMJ (2005) Experimental evidence for slow compressional waves. *Journal of Engineering Mechanics, ASCE* 131: 908–917.

Smith TM, Sondergeld CH, and Rai CS (2003) Gassmann fluid substitutions: A tutorial. *Geophysics* 68: 430–440.

Smith T, Sondergeld C, and Tinni A (2010) Microstructural controls on electric and acoustic properties in tight gas sandstones; some empirical data and observations. *The Leading Edge* 29: 1470–1474.

Smyth JR and Mccormick TC (1995) Crystallographic data for minerals. In: Ahrens TJ (ed.) *Mineral Physics and Crystallography: A Handbook of Physical Constants*, pp. 1–17. Washington, DC: American Geophysical Union.

Smyth JR and Mccormick TC (2013) Crystallographic data for minerals. In: *Mineral Physics & Crystallography: A Handbook of Physical Constants*, pp. 1–17. Washington, DC: American Geophysical Union.

Span R and Wagner W (1996) A new equation of state for carbon dioxide covering the fluid region from the triple-point temperature to 1100 K at pressures up to 800 MPa. *Journal of Physical and Chemical Reference Data* 25: 1509–1596.

Spycher N, Pruess K, and Ennis-King J (2003) CO_2–H_2O mixtures in the geological sequestration of CO_2. I. Assessment and calculation of mutual solubilities from 12 to 100 degrees c and up to 600 bar. *Geochimica et Cosmochimica Acta* 67: 3015–3031.

Stanek M, Geraud Y, Lexa O, Spacek P, Ulrich S, and Diraison M (2013) Elastic anisotropy and pore space geometry of schlieren granite: Direct 3-D measurements at high confining pressure combined with microfabric analysis. *Geophysical Journal International* 194: 383–394.

Stein S and Wysession M (2002) *An Introduction to Seismology, Earthquakes, and Earth Structure*. New York: Wiley-Blackwell.

Stroisz AM and Fjaer E (2013) Tracing causes for the stress sensitivity of elastic wave velocities in dry castlegate sandstone. *Geophysical Journal International* 192: 137–147.

Sumino Y and Anderson OL (1984) Elastic constants of minerals. In: Carmichael RS (ed.) *Handbook of Physical Properties or Rocks, III* Boca Raton, FL: CRC Press.

Tadmor EB, Miller RE, and Elliot RS (2012) *Continuum Mechanics and Thermodynamics: From Fundamental Concepts to Governing Equations*. New York: Cambridge University Press.

Takenouchi S and Kennedy GC (1964) Binary system H_2O–CO_2 at high temperatures +pressures. *American Journal of Science* 262: 1055–1074.

Thomas LK, Hankinson RW, and Phillips KA (1970) Determination of acoustic velocities for natural gas. *Journal of Petroleum Technology* 22: 889–892.

Thomsen L (1972) Elasticity of polycrystals and rocks. *Journal of Geophysical Research* 77: 315–327.

Tinder RF (2007) Tensor properties of solids, part two: Transport properties of solids. *Synthesis Lectures on Engineering*, vol. 2, pp. 145–236.

Todt T and Simmons G (1972) Effect of pore pressure on velocity of compressional waves in low-porosity rocks. *Journal of Geophysical Research* 77: 3731–3743.

Umekawa S and Sherby O (1966) Young's modulus of eutectic alloy systems with special emphasis on silver-lead system. *Journal of the Mechanics and Physics of Solids* 14: 65.

van Der Waals JD (1873) *Over de continuiteit van den gas- en vloeistoftoestand (on the continuity of the gas and liquid state)*. PhD, Leiden.

Van Weert F and Van Der Gun J (2012) Saline and brackish groundwater at shallow and intermediate depths: Genesis and worldwide occurrence. In: *39th International Association of Hydrologists*, Niagara Falls: International Association of Hydrologists.

Vance S and Brown JM (2010) Sound velocities and thermodynamic properties of water to 700 MPa and −10 to 100 degrees C. *Journal of the Acoustical Society of America* 127: 174–180.

Vankonynenburg PH and Scott RL (1980) Critical lines and phase equilibria in binary van der waals mixtures. *Philosophical Transactions of the Royal Society Series A: Mathematical Physical and Engineering Sciences* 298: 495–540.

Voigt W (1887) Theoretische studien über die elasticitätsverhältnisse der krystalle. *Abhandlungen der Königlichen Gesellschaft der Wissenschaften zu Göttingen* 34: 3–51.

Voigt W (1928) *Lehrbuch der kristallphysik (mit ausschluss der kristalloptik)*. Leipzig: B.G. Teubner.

Wagner W (2013) *Software for the Reference Equation of State Gerg-2008 for Natural Gases and Other Mixtures [Online]*. Bochum: Ruhr-Universität Bochum, Available: http://www.thermo.rub.de/en/prof-w-wagner/software/gerg-2004-gerg-2008.html.

Wagner W and Pruss A (2002) The iapws formulation 1995 for the thermodynamic properties of ordinary water substance for general and scientific use. *Journal of Physical and Chemical Reference Data* 31: 387–535.

Walker AM and Wookey J (2012) Msat-a new toolkit for the analysis of elastic and seismic anisotropy. *Computers & Geosciences* 49: 81–90.

Walsh JB (1965) Effect of cracks on compressibility of rock. *Journal of Geophysical Research* 70: 381–389.

Walsh JB, Brace WF, and England AW (1965) Effect of porosity on compressibility of glass. *Journal of the American Ceramic Society* 48: 605–608.

Walton K (1987) The effective elastic-moduli of a random packing of spheres. *Journal of the Mechanics and Physics of Solids* 35: 213–226.

Wang HF (2000) *The Linear Theory of Poroelasticity with Applications to Geomechanics and Hydrology*. Princeton: Princeton University Press.

Wang ZJ and Nur A (1991) Ultrasonic velocities in pure hydrocarbons and mixtures. *Journal of the Acoustical Society of America* 89: 2725–2730.

Wang ZJ, Nur AM, and Batzle ML (1990) Acoustic velocities in petroleum oils. *Journal of Petroleum Technology* 42: 192–200.

Watt JP (1979) Hashin–shtrikman bounds on the effective elastic-moduli of polycrystals with orthorhombic symmetry. *Journal of Applied Physics* 50: 6290–6295.

Watt JP (1980) Hashin–shtrikman bounds on the effective elastic-moduli of polycrystals with monoclinic symmetry. *Journal of Applied Physics* 51: 1520–1524.

Watt JP (1986) Hashin–shtrikman bounds on the effective elastic-moduli of polycrystals with trigonal (3,3 bar) and tetragonal (4,4 bar,4m) symmetry. *Journal of Applied Physics* 60: 3120–3124.

Watt JP, Davies GF, and O'Connell RJ (1976) Elastic properties of composite-materials. *Reviews of Geophysics* 14: 541–563.

Watt JP and Peselnick L (1980) Clarification of the Hashin–Shtrikman bounds on the effective elastic-moduli of polycrystals with hexagonal, trigonal, and tetragonal symmetries. *Journal of Applied Physics* 51: 1525–1531.

Wendland M, Hasse H, and Maurer G (1999) Experimental pressure–temperature data on three- and four-phase equilibria of fluid, hydrate, and ice phases in the system carbon dioxide-water. *Journal of Chemical and Engineering Data* 44: 901–906.

Wenk HR, Lonardelli I, Franz H, Nihei K, and Nakagawa S (2007) Preferred orientation and elastic anisotropy of illite-rich shale. *Geophysics* 72: E69–E75.

Wenk HR, Vasin RN, Kern H, Matthies S, Vogel SC, and Ivankina TI (2012) Revisiting elastic anisotropy of biotite gneiss from the Outokumpu scientific drill hole based on new texture measurements and texture-based velocity calculations. *Tectonophysics* 570: 123–134.

White D (2013) Seismic characterization and time-lapse imaging during seven years of CO_2 flood in the Weyburn field, Saskatchewan, Canada. *International Journal of Greenhouse Gas Control* 16(supplement 1): S78–S94.

Wilson WD (1959) Speed of sound in distilled water as a function of temperature and pressure. *Journal of the Acoustical Society of America* 31: 1067–1072.

Wilson PS (2005) Low-frequency dispersion in bubbly liquids. *Acoustics Research Letters Online (ARLO)* 6: 188–194.

Winkler KW (1996) Azimuthal velocity variations caused by borehole stress concentrations. *Journal of Geophysical Research, Solid Earth* 101: 8615–8621.

Wohlenberg J (1982) Density of rocks. In: Hellwege K-H (ed.) *Landolt–Bornstein Numerical Data and Functional Relationships in Science and Technology*, pp. 11–199. Berlin: Springer-Verlag.

Wong GSK and Embleton TFW (1984) Variation of specific-heats and of specific-heat ratio in air with humidity. *Journal of the Acoustical Society of America* 76: 555–559.

Wong GSK and Zhu SM (1995) Speed of sound in seawater as a function of salinity, temperature, and pressure. *Journal of the Acoustical Society of America* 97: 1732–1736.

Wood AB (1955) *A Textbook of Sound*. London: George Bell & Sons.

Wu T (1966) The effect of inclusion shape on the elastic moduli of a two-phase material. *International Journal of Solids and Structures* 2: 1–8.

Wuestefeld A, Verdon JP, Kendall JM, Rutledge J, Clarke H, and Wookey J (2011) Inferring rock fracture evolution during reservoir stimulation from seismic anisotropy. *Geophysics* 76: WC157–WC166.

Wyllie M, Gregory A, and Gardner G (1958) An experimental investigation of factors affecting elastic wave velocities in porous media. *Geophysics* 23: 459–493.

Xu XX, Hofmann R, Batzle M, and Tshering T (2006) Influence of pore pressure on velocity in low-porosity sandstone: Implications for time-lapse feasibility and pore-pressure study. *Geophysical Prospecting* 54: 565–573.

Yam H (2011) *CO_2 Rock Physics: A Laboratory Study*. MSc, University of Alberta.

Yam H and Schmitt DR (2011) CO_2 rock physics: A laboratory study. *InSite Magazine* 30: 13–16.

Yan XF, Yao FC, Cao H, Ba J, Hu LL, and Yang ZF (2011) Analyzing the mid-low porosity sandstone dry frame in central Sichuan based on effective medium theory. *Applied Geophysics* 8: 163–170.

Yoshimura HN, Molisani AL, Narita NE, Cesar PF, and Goldstein H (2007) Porosity dependence of elastic constants in aluminum nitride ceramics. *Materials Research* 10: 127–133.

Ziabakhsh-Ganji Z and Kooi H (2012) An equation of state for thermodynamic equilibrium of gas mixtures and brines to allow simulation of the effects of impurities in subsurface CO_2 storage. *International Journal of Greenhouse Gas Control* 11: S21–S34.

Zimmer M (2003) *Seismic Velocities in Unconsolidated Sands: Measurements of Pressure, Sorting, and Compaction Effects*. PhD, Stanford University.

Zimmer M, Prasad M, Mavko G, and Nur A (2007) Seismic velocities of unconsolidated sands: Part 1 – Pressure trends from. *Geophysics* 72: E1–E13.

Zimmerman RW (1984) Elastic-moduli of a solid with spherical pores – New self-consistent method. *International Journal of Rock Mechanics and Mining Sciences* 21: 339–343.

Zimmerman RW (1985) The effect of microcracks on the elastic-moduli of brittle materials. *Journal of Materials Science Letters* 4: 1457–1460, *AAPG Bulletin-American Association of Petroleum Geologists* 59: 154–158.

Zoback MD and Byerlee JD (1975) Permeability and effective stress. *AAPG Bulletin-American Association of Petroleum Geologists* 59(1): 154–158.